

FLORIDA STATE UNIVERSITY
COLLEGE OF ARTS AND SCIENCES

SEARCH FOR LARGE EXTRA DIMENSIONS VIA SINGLE PHOTON
PLUS MISSING ENERGY FINAL STATES AT $\sqrt{S} = 1.96$ TEV

By
EDGAR F. CARRERA

A Dissertation submitted to the
Department of Physics
in partial fulfillment of the
requirements for the degree of
Doctor of Philosophy

Degree Awarded:
Spring Semester, 2009

The members of the Committee approve the Dissertation of Edgar F. Carrera defended on December 3, 2008.

Yuri Gershtein
Professor Co-Directing Dissertation

Harrison Prosper
Professor Co-Directing Dissertation

Chris Schatschneider
Outside Committee Member

Laura Reina
Committee Member

Grigory Rogachev
Committee Member

Horst Wahl
Committee Member

The Office of Graduate Studies has verified and approved the above named committee members.

To my mother, my sister, and my father...

ACKNOWLEDGEMENTS

I would like to thank my adviser Yuri Gershtein for his invaluable guidance, insights, great ideas, patience, and constant support and motivation. I will always be grateful to him, not only for his advise and teachings, but for injecting a sometimes much needed dose of optimism and positive attitude in my personality. Andrew Askew, for his constant help, fruitful discussions, and permanent disposition to help, not only me, but graduate students in general. Yurii Maravin and Alexey Ferapontov for their important contributions to the study presented in this dissertation.

I am also thankful to Florida State University faculty, postdoctoral researchers, fellow graduate students, and staff, for their support and help. In particular, I would like to thank all members of the High Energy Physics group; my doctoral training could have not been completed without their help. Special mention to members of my graduate committee for the time they spent serving in it and for their suggestions to improve this manuscript. I am thankful to Harrison Prosper for “adopting” me as his graduate student during the last few months of my training, and making sure I complete my degree without any inconvenient.

I thank members of the DØ Collaboration and staffs at Fermilab. The expertise of Stephen Mrenna was fundamental for carrying out an important part of this study.

Finally, I would like to thank my family and friends for their support and help, predominantly during difficult extracurricular hours.

— Edgar

TABLE OF CONTENTS

List of Tables	vii
List of Figures	viii
Abstract	xiii
1. INTRODUCTION	1
1.1 The Standard Model of Particle Physics	1
1.1.1 Electromagnetic Interactions	4
1.1.2 Strong Interactions	5
1.1.3 Weak Interactions and the Electroweak Unification	5
1.2 Gravity and the Hierarchy Problem	7
1.3 Theories of Large Extra Dimensions	8
1.4 Graviton Production at Colliders	10
2. EXPERIMENTAL APPARATUS	12
2.1 The Tevatron Accelerator Complex	12
2.2 Coordinate System and Units Convention	14
2.3 The DØ Detector	16
2.3.1 Tracking Detectors	17
2.3.1.1 Silicon Microstrip Tracker (SMT)	18
2.3.1.2 Central Fiber Tracker (CFT)	19
2.3.2 Preshower Detectors	21
2.3.3 Calorimeter	22
2.3.4 Luminosity Monitor	26
2.3.5 Muon Spectrometer	27
2.3.6 Trigger and Data Acquisition	28
2.3.6.1 The Level 1 trigger	30
2.3.6.2 The Level 2 trigger	32
2.3.6.3 The Level 3 trigger	33
2.3.6.4 Data acquisition systems	34
3. EVENT RECONSTRUCTION	36
3.1 Track Reconstruction	37
3.1.1 The Alternative Algorithm	37

3.1.2	The Histogramming Track Finder	39
3.2	Vertex Reconstruction	40
3.3	Electromagnetic Object Reconstruction	42
3.4	Muon Reconstruction	45
3.5	Jet Reconstruction	48
3.6	Missing Energy Reconstruction	50
4.	ANALYSIS	52
4.1	Event Selection	53
4.1.1	Datasets and Triggers	54
4.1.2	Signal, Background Sources, and MC Simulations	57
4.1.3	The EM Pointing Algorithm	62
4.1.4	Single Photon Sample Selection	67
4.1.4.1	Photon p_T , jet p_T , and \cancel{E}_T requirements.	68
4.1.4.2	Anti-track match requirement	69
4.1.4.3	CPS match requirement and EM pointing resolution	70
4.1.4.4	Muon and high- p_T track rejection	71
4.1.4.5	Cosmic muon rejection	73
4.1.4.6	Pointed vertex requirement	74
4.1.4.7	Photon shower shape requirements	76
4.2	Background Estimation	82
4.2.0.8	Non-collision and Misidentified jets background estimation	82
4.2.0.9	Additional SM background estimation	87
5.	RESULTS AND CONCLUSIONS	94
5.1	Systematic Uncertainties	94
5.2	Limit Setting Technique	94
5.3	Limits on LED	96
5.4	Summary and Final Remarks	98
	REFERENCES	100
	BIOGRAPHICAL SKETCH	106

LIST OF TABLES

1.1	Leptons (spin $\frac{1}{2}$) [1]	2
1.2	Quarks (spin $\frac{1}{2}$) [1]	3
3.1	Muon types [2]	47
4.1	Run IIa trigger list.	55
4.2	Run IIb trigger list.	56
4.3	Data summary for Run IIa.	57
4.4	Data summary for Run IIb.	57
4.5	Methodology used for calculating the number of remaining events in data when MC samples are used.	90
4.6	Data and estimated backgrounds for Run IIa and Run IIb.	91
5.1	Summary of limit calculations.	97

LIST OF FIGURES

2.1	Different accelerators at Fermilab Tevatron Accelerator Complex [3].	13
2.2	DØcoordinate system with respect to the Tevatron ring [4].	15
2.3	A cross-section view in the y - z plane of the DØdetector.	17
2.4	A cross-section view in the y - z plane of the central tracking system. Also shown are the solenoid, the preshower detectors, luminosity monitor, and the calorimeter.	18
2.5	Schematic of the silicon microstrip tracker detector.	19
2.6	Schematic endview of the central fiber tracker with its associated waveguides.	20
2.7	Cross section of the scintillating strips used in the CPS and FPS. The circles indicate the location of the embedded wavelength shifting fibers.	22
2.8	The DØcalorimeter..	23
2.9	DØcalorimeter cell.	24
2.10	Schematic view of a portion of the DØdetector.	25
2.11	Readout chain of the calorimeter.	25
2.12	Schematic showing the location of the luminosity counters.	26
2.13	Exploded view of the DØdrift tubes.	28
2.14	Exploded view of the DØmuon scintillators.	29
2.15	Overview of the DØtrigger and data acquisition systems.	30
2.16	Schematic illustration of the information and data flow through the L3DAQ system.	35
3.1	Schematic of the construction of track hypotheses in the AA method and its relevant parameters [5].	38

3.2	The histogramming technique shown for an example of a single 1.5 GeV muon track of 5 hits. (a) The family of trajectories containing a given hit. (b) The geometric place of all trajectories containing a given hit in parameter space. (c) Curves from different hits intersect at one point corresponding to the track parameters. (d) The point of intersection can be seen as a peak in the (ρ, ϕ) histogram. [6]	40
3.3	A circle of calorimeter towers in $\eta - \phi$ space. [7]	43
3.4	Schematic for the isolation in the simple cone algorithm. [7]	44
3.5	A local track segment in the muon system. Black vertical lines are the wire planes with the wires represented as “×”, running perpendicular to the plane of the picture. Drift circles are in red while the muon track is represented by a blue inclined line. [8].	46
4.1	Feynman diagram for the process $q\bar{q} \rightarrow \gamma + G_{KK}$. Direct graviton production in the $\gamma + \cancel{E}_T$ channel.	52
4.2	LED cross-sections for central single photons with $p_T^{gen} > 90$ GeV as function of M_D . Plots with linear (left) and semi-logarithmic (right) scales are shown.	58
4.3	Feynman diagrams for the process $q\bar{q} \rightarrow Z + \gamma$	59
4.4	Feynman diagram for the background process $W \rightarrow e\nu$. The electron (positron) is misidentified as a photon due to inefficiency in the tracker.	59
4.5	From left to right: Feynman diagrams representing the initial state radiation (IRS), trilinear gauge coupling (TGC), and final state radiation (FSR) contributions to the background process $W + \gamma$. The lepton from the leptonic decay of the W is not reconstructed.	60
4.6	Example of a Feynman diagram for the background process $W/Z + \text{jets}$. The jet is misidentified as a photon.	60
4.7	K-factor as a function of photon p_T with $p_T^{jet} > 15$ GeV veto (left) and with no veto on jets (right) [9].	62
4.8	Detector display of a single photon event. In (a), the presence of an EM object is depicted in red, while missing transverse energy (MET) is shown in yellow. In (b) and (d), tracks can be seen, together with the energy deposition in the calorimeter. (c) shows very little activity (red and blue segments) in the muon spectrometer.	64
4.9	Detector display of a cosmic ray event with identical signature as for a signal single photon event. A cosmic ray muon enters the detector from the upper part, deposits energy in the calorimeter, and leaves at the bottom.	65

4.10	Detector display of a beam halo event with identical signature as for a signal single photon event. Notice the presence of no tracks and, therefore, no reconstructed interaction vertex in the event.	66
4.11	Illustration of the inward extrapolation of the the EM pointing algorithm fit in the $r - z$ plane (left), which predicts the z -coordinate of the interaction vertex, and in the $r - \phi$ plane (right), which predicts the DCA to the z -axis of the detector.	67
4.12	<i>Significance-like</i> metric ϵ_S/\sqrt{B} for the signal versus photon p_T threshold in Run IIa.	69
4.13	\cancel{E}_T distribution for Run IIa signal events with photon $p_T > 90$ GeV	70
4.14	Three body mass distribution for $Z \rightarrow e^+e^-\gamma$ events in Run IIb data.	71
4.15	CPS match efficiency vs photon rapidity using $Z \rightarrow e^+e^-\gamma$ events in Run IIb data (left) and Run IIb MC (right).	72
4.16	Pointing resolution measured using $Z \rightarrow e^+e^-\gamma$ events in Run IIb data (left) and MC (right).	72
4.17	<i>Significance-like</i> metric ϵ_S/\sqrt{B} for the signal versus track p_T maximum threshold, for different isolation values. Run IIa data (left) and RunIIb (right) results are shown.	73
4.18	Cosine of θ distribution for Run IIa (left) and Run IIb (right) photon samples. Zero is a default value for those events that do not have muon A-segments or for events with muon A-layer positions exceeding the maximum allowed size, as stated in Ref. [2].	74
4.19	Distribution of the distance along the z -axis between the reconstructed vertex that best agrees with that from the pointing tool and the pointed vertex for different Run IIa data samples.	75
4.20	Distribution of the distance along the z -axis between the reconstructed vertex that best agrees with that from the pointing tool and the pointed vertex for different Run IIb data samples.	76
4.21	DCA distribution of the Run IIa photon sample before and after applying a requirement on ΔZ_{min}	77
4.22	DCA distribution of the Run IIb photon sample before and after applying a requirement on ΔZ_{min}	77
4.23	Distribution of the energy fraction at the third EM layer of the calorimeter for different Run IIa data samples.	78

4.24	Distribution of the energy fraction at the third EM layer of the calorimeter for different Run IIb data samples.	79
4.25	Distribution of the energy fraction at the first EM layer of the calorimeter for non-collision events.	80
4.26	<i>DCA</i> distribution of the Run IIa photon sample before and after applying a requirement on the fractional energy at the third EM layer of the calorimeter.	80
4.27	<i>DCA</i> distribution of the Run IIb photon sample before and after applying a requirement on the fractional energy at the third EM layer of the calorimeter.	81
4.28	Photon p_T distribution in semi-log scale for the photon sample. The peaks in one of the Run IIa distributions is due to calorimeter noise. The requirements imposed successfully reject those problematic events.	82
4.29	Photon <i>DCA</i> distributions in the photon sample.	83
4.30	Detector display for a beam halo event with a single photon. The number of reconstructed tracks is less than three.	84
4.31	Detector display of a cosmic ray muon event with a single photon. No tracks and, therefore, no vertices are reconstructed.	85
4.32	Comparison between misidentified jets <i>DCA</i> templates from two different samples in Run IIa (left). <i>DCA</i> template shapes in Run IIa (right).	86
4.33	(a) <i>DCA</i> templates in Run IIb. (b,c,d) Comparison between shapes in Run IIa and Run IIb.	87
4.34	<i>DCA</i> distribution for the selected events in data (points with statistical uncertainties). The different histograms represent the estimated background composition from the template fit to this distribution. The number of events within a window of 4 cm in <i>DCA</i> are shown.	88
4.35	<i>DCA</i> template fit using the EM plus jet sample for Run IIa and Run IIb.	88
4.36	e/γ <i>DCA</i> templates comparison.	89
4.37	Photon azimuthal distribution in a photon sample with lower kinematical requirements. The different background components are shown.	90
4.38	Missing transverse energy distribution in semi-log scale for Run IIa photon sample after releasing the \cancel{E}_T requirement.	92
4.39	(a) Exponential fit to the difference between data and the total accounted background at low \cancel{E}_T in Run IIa data. (b) Zoomed-in figure.	92

4.40	Photon p_T distribution for the final candidate events in Run IIa and Run IIb photon samples (data show statistical uncertainties). The LED signal is stacked on top of SM backgrounds.	93
4.41	Photon p_T distribution for the final candidate events in the combined Run IIa and Run IIb photon sample (data show statistical uncertainties). The LED signal is stacked on top of SM backgrounds.	93
5.1	Expected and observed lower limits on M_D for LED in the $\gamma + \cancel{E}_T$ final state. CDF limits with 2 fb^{-1} of data (single photon channel) [10], and the LEP combined limits [11] are also shown.	98

ABSTRACT

This dissertation presents a search for large extra dimensions in the single photon plus missing transverse energy final states. We use a data sample of approximately 2.7 fb^{-1} of $p\bar{p}$ collisions at $\sqrt{s} = 1.96 \text{ TeV}$ (recorded with the DØ detector) to investigate direct Kaluza Klein graviton production and set limits, at the 95% C.L., on the fundamental mass scale M_D from 970 GeV to 816 GeV for two to eight extra dimensions.

CHAPTER 1

INTRODUCTION

Today, more than 2300 years from Democritus' first ideas on atoms, and more than 100 years after Thomson's electron discovery, particle physicists around the world are still trying to unveil the secrets of our universe by seeking the most elementary pieces that form everything there is, and by refining our understanding of the interactions that govern these pieces. This dissertation is part of that quest for knowledge. It presents an analysis that tests for an interesting hypothesis, that our universe has more than three spatial dimensions, which, if true, would shed some light on one of the least understood forces of Nature: gravity.

This first chapter gives an overview of the current knowledge in the field of particle physics and explains the main empirical difficulties that have led to the emergence of theories that postulate the existence of large extra dimensions (LED). The analysis in this dissertation aims at testing the hypothetical scenarios presented by theories of LED, which are discussed at the end of the chapter. Later in this manuscript, the experimental apparatus and the technical machinery required to carry out this study are explained, as well as the details of the analysis itself.

1.1 The Standard Model of Particle Physics

The Standard Model¹(SM) of particles and fields is a theory that explains the interactions between the most basic constituents of matter in a framework that combines special relativity with quantum mechanics. Although incomplete, it has been extraordinarily successful in describing our universe to the smallest distance scales studied with impressive precision.

In our current understanding, quarks, leptons, and the particles responsible for the interactions between them, called mediators, make up everything that exists around us.

¹For a review of the SM see Ref. [12, 13], for example.

At current accelerator energies, they all seem to be point-like, indivisible, particles.

Quarks and leptons are *fermions*, i.e., they have angular momentum (*spin*²) of $\frac{1}{2}\hbar$. *Bosons*, on the other hand, are particles with integer spin. The six quarks and six leptons³ that exist in Nature are grouped into three generations, as can be seen in Tables 1.1 and 1.2. Leptons are either neutral or carry integral electric charge. The electron (e) is the best known and most familiar of the leptons. There are heavier versions of it called muons (μ) and taus (τ). Each of these charged leptons seem to be matched to their corresponding *flavor* of uncharged leptons, called neutrinos (ν). Quarks, on the other hand, have fractional charges and come in six different flavors: the *up* (u) and *down* (d); the *strange* (s) and *charm* (c); and the *top* (t) and *bottom* (b) quarks. They also carry *color*, a three-valued characteristic analogous to electric charge that permits interactions among them.

Table 1.1: Leptons (spin $\frac{1}{2}$) [1]

Generation	Lepton	Charge (e)	Mass (MeV)
First	e	-1	0.511
	ν_e	0	$< 2 \times 10^{-6}$
Second	μ	-1	105.66
	ν_μ	0	< 0.19
Third	τ	-1	1777
	ν_τ	0	< 18.2

Modern theories in particle physics describe particles as excitations of relativistic quantum-mechanical *fields* (ψ) occupying some region of space. A mathematical construction, called a *Lagrangian*, holds all the information about a physical system and it is the starting point if one wants to determine the evolution or properties of that system, for example, the energy and momentum of the fields. The so-called *gauge* theories are used to describe the interactions between the fields based on symmetry principles. In this context, *gauge* transformations are symmetry operations performed on the fields of the theory. These transformations can be *global* or *local*, depending on whether the mathematical entities

²Or just $\frac{1}{2}$ in the rest of this dissertation as, conventionally, $\hbar = 1$. We also adopt the convention for the speed of light $c = 1$ in this manuscript.

³Plus their corresponding antiparticles (particles with the same mass and life time, but with opposite charge and magnetic moment). It is striking to note that the hierarchy of fermion masses spans over eleven orders of magnitude.

Table 1.2: Quarks (spin $\frac{1}{2}$) [1]

Generation	Flavor	Charge (e)	Bare Mass
First	u	$\frac{2}{3}$	1.5 to 3.0 MeV
	d	$-\frac{1}{3}$	3.5 to 6 MeV
Second	c	$\frac{2}{3}$	$1.27^{+0.07}_{-0.11}$ GeV
	s	$-\frac{1}{3}$	104^{+26}_{-34} MeV
Third	t	$\frac{2}{3}$	171.2 ± 2.1 GeV
	b	$-\frac{1}{3}$	$4.20^{+0.17}_{-0.07}$ GeV

defining them are functions of the space-time coordinates (x^μ) or not.

Current quantum field theories⁴ require the Lagrangian, which is a function of the fields ψ and their space-time derivatives, to be invariant under global and local gauge transformations. This guarantees that the calculated observables are finite, a characteristic known as *renormalizability* of the theory. Modern field theories associate families of these transformations to mathematical structures called *groups*. When the elements of these symmetry groups commute the associated theory is called *Abelian*. Quantum electrodynamics (QED), the theory describing the electromagnetic interactions among charged particles, is an example of such a theory. QED is summarized in Section 1.1.1 and used as an example of how a gauge theory is constructed.

In 1954, Yang and Mills applied the strategy for constructing QED, but using mathematical groups with non-commuting elements to formulate theories known as *non-Abelian* gauge theories. Quantum chromodynamics (QCD) is a spectacular, successful, example of a non-Abelian gauge theory. QCD describes the strong interactions between quarks; it is briefly described in Section 1.1.2. Yang-Mills theories have inspired the application of these principles to even higher order symmetry groups. In the SM, all the fundamental interactions are formulated in this way.

Weak interactions, responsible for the slow process of nuclear β -decay, occurs between all leptons and quarks. In the 1960s, theories of the weak interactions were combined with electrodynamics into a single theory called the electroweak theory, following the same Yang-Mills recipe. This theory is described in Section 1.1.3.

⁴For a review of quantum field theories see, for example, [14, 15].

There is one additional force in Nature, felt by all its basic constituents: gravity. However, its strength is so weak (compared to that of other forces) that its contribution is neglected in the SM. The extreme weakness of gravity has puzzled many generations of physicists. Gravity and the relevant aspects of the puzzles that it presents in the context of the SM are left to Section 1.2.

1.1.1 Electromagnetic Interactions

Electromagnetic interactions occur between charged particles and are mediated by bosons called photons (γ), which are simply the excitations of the quantized Maxwell fields. Photon fields emerge naturally in QED after the introduction of the covariant derivative⁵ D_μ (Eq. 1.1) in the Lagrangian (\mathcal{L}_{free}) that describes a free fermion of mass m (free Dirac Lagrangian, Eq. 1.2). This addition is necessary to restore local gauge invariance after a local gauge (phase) transformation (Eq. 1.3) of the particle field,

$$D_\mu \equiv \partial_\mu + ieA_\mu, \tag{1.1}$$

$$\mathcal{L}_{free} = \bar{\psi}(i\cancel{D} - m)\psi, \tag{1.2}$$

$$\psi \rightarrow e(i\alpha(x))\psi. \tag{1.3}$$

The vector field A_μ , which transforms as in Eq. 1.4, is just the electromagnetic potential. The description of free electromagnetic fields requires A_μ to be massless, otherwise local gauge invariance would be lost. A_μ is associated with the photon field that interacts with the charged particle fields. The complete QED Lagrangian in Eq. 1.5, where $F_{\mu\nu}$ is the electromagnetic field strength, and the current density defined in Eq. 1.6 generate all of electrodynamics and specify the currents produced by Dirac particles.

$$A'_\mu = A_\mu(x) - \frac{1}{e}\partial_\mu\alpha(x) \tag{1.4}$$

⁵This procedure, a simple mechanism for converting a globally invariant Lagrangian into a locally invariant one, is called the *minimum coupling rule*.

$$\mathcal{L}_{QED} = -\frac{1}{4}F_{\mu\nu}F^{\mu\nu} + \bar{\psi}(i\cancel{D} - m)\psi - e\bar{\psi}A\psi \quad (1.5)$$

$$J_{\mu} \equiv \bar{\psi}\gamma_{\mu}\psi \quad (\gamma_{\mu} \text{ are the usual Dirac matrices}) \quad (1.6)$$

The family of phase transformations, $U(\alpha) = e^{i\alpha(x)}$, form the unitary Abelian group $U(1)$.

1.1.2 Strong Interactions

Strong interactions are responsible for binding the quarks together in the neutron and proton. They are described by QCD and mediated by bosonic particles called *gluons* (g). Leptons do not participate in strong interactions since they lack *color* charge, but quarks, which carry *color* (or *anticolor*), do feel this force. The strength of strong interactions grows with increasing distance, while it becomes weak at smaller distances. This behavior, known as *asymptotic freedom*, prevents isolated quarks (or isolated gluons) from appearing in Nature. Instead, they form *hadrons*, composite particles, baryons or mesons, made of quarks. Baryons are composed of three quarks or antiquarks, whereas mesons are quark-antiquark pairs. They have integer or no electric charge and are color neutral.

QCD is based on the transformations belonging to the symmetry group $SU(3)$. We can apply the same formalism as in Yang-Mills theories, but now with ψ being three component column vectors describing a particular quark flavor with three possible colors: red, blue, and green. The $SU(3)$ transformations are able to change the color of the quark fields. In order to achieve local gauge invariance, one can use the minimum coupling rule used in the Abelian case of QED. This requirement introduces eight massless gauge bosons which are the aforementioned gluons.

Gluons carry *color* themselves, therefore they can couple directly to other gluons. This feature makes quantum chromodynamics a lot more complicated than electrodynamics, but far richer in terms of phenomenology.

1.1.3 Weak Interactions and the Electroweak Unification

Weak interactions occur between leptons and quarks via the intermediate bosons W^{\pm} (*charged weak processes*) and Z^0 bosons (*neutral weak processes*). Charged processes were

studied early in nuclear β -decays⁶. However, the neutral weak currents, which explains processes like neutrino scattering by quarks or electrons, were studied rather recently.

Glashow, Salam, and Weinberg used the $SU(2)_L \times U(1)_Y$ symmetry group to describe weak and electromagnetic interactions in a unified electroweak theory. In this theory, leptons and quarks are arranged in doublets such as (ν_e, e) , (u, d) , etc, and are subject to $SU(2)$ gauge transformations. Local gauge invariance requires the introduction of three massless spin-1 gauge bosons W^\pm and W^0 , arranged in a triplets of *weak isospin* I . The subscript L on $SU(2)_L$ indicates that the gauge fields only couple to left-handed⁷ particles (or right-handed antiparticles). Right handed fermions are arranged in singlets and transform under $U(1)$ symmetry, while left handed fermions can be transformed by both gauge symmetries; no right-handed neutrinos exist in the SM. The addition of $U(1)$ incorporates QED, adding one more gauge field, B^0 . The conserved quantum number Y is called *weak hypercharge*.

Experiment rules out the possibility for all the gauge bosons to be massless. Therefore, it is necessary to include a mechanism in the theory that allows for mass while preserving renormalizability. The mechanism is spontaneous symmetry breaking via the Higgs mechanism [16]. This mechanism is responsible for endowing mass to the weak bosons, leptons, and quarks. The result is one massless gauge boson field γ , which is the linear combination $W^0 \sin(\theta_W) + B^0 \cos(\theta_W)$, that already appeared in QED, and three massive gauge bosons W^+ , W^- , and Z^0 ; the latter one being the orthogonal combination $W^0 \cos(\theta_W) - B^0 \sin(\theta_W)$. The angle θ_W is a parameter of electroweak theory. Additionally, a neutral scalar particle called the Higgs boson is predicted but has not yet been observed.

The gauge bosons W^+ and W^- exchange one unit of charge and are able to convert one member of a fermion doublet into another. While transmutations between generations among charged leptons does not seem to be possible, quark and neutrino generation mixing⁸ does occur via charge weak currents. The Z^0 boson transmits neutral weak current with no change of charge, preserving quark and lepton flavors. It transforms singlets and the upper and lower members of doublets into themselves.

If we combine the $SU(3)$ symmetry of strong interactions with the $SU(2)_L \times U(1)_Y$ electroweak symmetry, we arrive at the gauge invariant theory called the Standard Model.

⁶Fermi developed a theory in which weak interactions were point interactions. Although rather successful, it is nevertheless just an approximation. It present problems since it is a non-renormalizable theory.

⁷The handedness of a particle indicates the alignment of its spin relative to its momentum.

⁸The SM needs to be slightly modified to incorporate the rather new evidence of this behavior.

1.2 Gravity and the Hierarchy Problem

We have seen how the electromagnetic, weak, and strong interactions can be described by the Standard Model. However, there is one additional force, gravity, which we have not yet considered. Despite our everyday familiarity with gravity, it is the least understood of the forces of Nature. At the macroscopic level (or equivalently at low energies), the force between two equal point masses M is proportional to GM^2/r^2 , where G is the Newtonian coupling constant and r is their separation. Newton's non-relativistic approximation is contained as a limit of Einstein's theory of general relativity, which is known to work correctly on scales of the solar system. At larger scales, however, the situation is not as clear. For instance, phenomena like the observed invariant spiral structure of galaxies, known as the winding problem [17], could be a real blow to general relativity. The existence of dark matter is widely accepted among scientists to explain the disagreement between theory and the observed results, but the nature of dark matter is unknown.

On the other hand, efforts to build a quantum theory of gravity, where the *graviton* would be the force carrier for the gravitational field, present fundamental problems. For example, the role that space-time plays in quantum gauge theories is radically different from the one in general relativity. In the former, the space-time geometry is simply a kinematical canvas in which the fields propagate. In general relativity, by contrast, the space-time itself is a dynamical variable. Despite this, courageous efforts have been made to salvage the powerful machinery of perturbative quantum field theory in order to apply it to gravity. Unfortunately, it turns out that the resulting theories are non-renormalizable, that is, infinities that appear at higher orders cannot be removed with a finite number of counter-terms. Theories like supergravity [18] or string theory [19] (which introduces the concept of extra dimensions) are the current attempts of a quantum theory of gravity.

Measured accurately only at the ~ 1 cm range, gravity is at least 10^{38} orders of magnitude weaker than the other interactions in Nature. It is assumed that it only becomes as strong as the gauge interactions at the *Planck length* $\sim 10^{-33}$ cm, or equivalently, at the *Planck energy* scale $M_{Pl} = G^{-1/2} \sim 10^{19}$ GeV. The enormous jump between the current experimental energy regime near the *electroweak energy* scale ($m_{EW} \sim 10^3$ GeV), and the Planck energy scale, introduces a serious problem for the validity of the SM. It is traditionally believed that the SM alone cannot provide a good physical description over such a broad range of energies,

and that the breakdown of its simple gauge group has something to do with setting the scale for gravitational interactions. This is still a very interesting puzzle for many physicists, which is referred as the *hierarchy* problem of the SM.

The difficulty with the large hierarchy of energies between these two scales, however, is not the broad range they span. After all, the Newtonian theory of gravity covers more than fifteen orders of distance magnitude with extraordinary accuracy. The range spanned by electromagnetism is even more striking. The underlying problem stems from the fact that the SM, in its current form, violates the principle of *naturalness* [20], which requires the observable properties of a theory to be stable under very small variations of its fundamental parameters. The SM requires a tremendous amount of *fine-tuning* of its parameters (to a precision of $\sim (m_{EW}/M_{Pl})^2 \sim 10^{-32}$) in order for it to be able to work at energies close to the Planck scale; such adjustments are regarded unnatural, and are assumed to be absent in a more complete theory.

Supersymmetry [21] and technicolor [22] are, today, two of the most appealing theories for solving the fine-tuning problem. These theories rely on the idea of higher order symmetries being broken by different mechanisms, at energies lower than the Planck scale. In the next section, however, we introduce the paradigm of large extra dimensions, which establishes a new approach to overcome the hierarchy problem.

1.3 Theories of Large Extra Dimensions

In 1998, Nima Arkani-Hamed, Savas Dimopoulos, and Gia Dvali (ADD) [23, 24] proposed a new framework for solving the hierarchy problem of the SM. Their basic assumption is that m_{EW} is the only fundamental short distance scale in Nature, and that our interpretation of M_{Pl} , being a fundamental energy scale, is just an artifact created by the presence of extra dimensions at very short distances. This assumption is well motivated since m_{EW} is the only fundamental scale experimentally tested. M_{Pl} , on the other hand, relies on the assumption that gravity is unmodified over at least 33 orders of magnitude. It is interesting to note that many theoretical frameworks are based on this, rather blind, extrapolation. It is worthwhile, therefore, to try a different approach.

The ADD paradigm postulates the presence of n extra spatial dimensions, with sizes (R) much greater than the electroweak scale ($\sim \text{TeV}^{-1} \sim 10^{-19}$ m). While the SM particles

are bound to our 3-dimensional space (3-d brane), gravitons can penetrate the additional volume (created by the large extra dimensions), thereby decreasing the strength of the gravitational field in the 3-d brane. The hierarchy and fine-tuning problems are nullified since the fundamental Planck scale in the $(4 + n)$ -dimensional space-time (M_D) becomes, effectively, the electroweak scale. In order to realize this, consider two test masses of mass m_1 and m_2 placed at distances r , very small compared to the size of the extra volume. The gravitational potential they feel is derived using the Gauss's law in $(4 + n)$ dimensions [23]:

$$V(r) \sim \frac{m_1 m_2}{M_D^{n+2}} \frac{1}{r^{n+1}}, \quad (r \ll R). \quad (1.7)$$

As we separate these two masses, the leakage of the gravitational field to the extra volume starts to stabilize. The Newtonian potential $1/r$ is obtained at distances $r \gg R$, as the gravitational field cannot penetrate further into the extra volume:

$$V(r) \sim \frac{m_1 m_2}{M_D^{n+2} R^n} \frac{1}{r}, \quad (r \gg R). \quad (1.8)$$

From Eq. 1.7 and Eq. 1.8, we can infer the relation:

$$M_{Pl}^2 \sim M_D^{2+n} R^n. \quad (1.9)$$

Clearly, the smallness of the scale M_D is concealed by the size of the extra volume. The apparent febleness of the gravitational field is therefore explained, and the hierarchy problem is solved in a trivial way. Non-trivial is, however, the localization of the SM fields in our 4-dimensional world. Many possible mechanisms have been envisaged for such localizations. In this discussion, we will assume the framework to have a coherent localization mechanism for the SM model particles, most likely in terms of trapping zero modes on topological defects of the compactified extra space [23]. These requirements also lead to the assumption that the extra space is compactified in a torus.

If we require R to reproduce the extrapolated M_{Pl} scale with $M_D \sim m_{EW}$, we arrive at

$$R \sim 10^{\frac{30}{n}-19} \text{ cm}. \quad (1.10)$$

To date, only $n = 1$ ($R \sim 10^{11}$ cm), and $n = 2$ ($R \sim 1$ mm) scenarios seem to have been ruled out, or very tightly constrained. The former is excluded by the validity of the Newtonian gravity in our solar system. The $n = 2$ scenario is constrained primarily by direct gravity measurements. For example, the torsion-balance experiment described in Ref. [25]) imposes a limit of $R \leq 44 \mu\text{m}$ for the size of extra dimensions. Other observations and experiments involving astrophysics and cosmology put lower limits on M_D as large as 30 TeV for $n = 2$. A famous example is the non-observation of additional *cooling* for the supernovae SN1987A [26] that would be evident in the presence of LED. Other measurements are less robust. This dissertation tests for $n \geq 2$, observing that independent collider searches need to be performed, even for the case $n = 2$.

We have presented the basic ideas that serve as the main framework for the development of theories that can cure the hierarchy problem. In the next section, we summarize the key aspects of the effective theory presented in Ref. [27], which formulates the mechanism for graviton production at high-energy colliders used in this dissertation.

1.4 Graviton Production at Colliders

The compactification of the extra space forces the gravitational field to populate only certain energy modes. They are known as Kaluza-Klein (KK) modes and have mass splitting $\Delta m \sim 1/R$. Given this mass separation, the current experimental energy resolutions are only sensitive to the case of large number of extra dimensions. However, for large n , the total cross-section is negligible, since there is only a small number of KK modes that can be produced. Therefore, we limit ourselves to the cases where $n \leq 8$. For experimental applications, when n is not too large, the mass splittings are so small that the different KK states can be summed up, forming towers of modes that behave like massive, non-interacting, stable particles. We call these particles KK gravitons (G_{KK}).

At low energy and small curvature, the equations that describe the motion of the KK excitations reduce to the Einstein equation in $4 + n$ dimensions [27]. The associated Lagrangian is used to compute the rate of graviton-emission processes by employing field parametrizations and gauge choices that prevent the appearance of non-physical degrees of freedom. The interested reader can consult Ref. [27] for a detail derivation of the graviton

Feynman rules.

In principle, since the interactions are with the 3-d brane, processes with real graviton emission are expected to be suppressed by $\sim 1/M_{Pl}^2$. For instance, the cross-section for producing a graviton (a single KK mode, G) of mass m and a photon in a fermion-antifermion collision is [27]

$$\frac{d\sigma_m}{dt}(f\bar{f} \rightarrow \gamma G) = \frac{\alpha Q_f^2}{16N_f s \bar{M}_{Pl}^2} F_1(t/s, m^2/s), \quad (1.11)$$

where Q_f and N_f are the electric charge and number of colors of the fermion f , $\bar{M}_{Pl} = M_{Pl}/\sqrt{8\pi}$, t and s are the usual Mandelstam variables, and F_1 is given by

$$F_1(x, y) = \frac{1}{x(y-1-x)} [-4x(1+x)(1+2x+2x^2) + y(1+6x+18x^2+16x^3-6y^2x(1+2x)+y^3(1+4x))]. \quad (1.12)$$

However, the large size of the compactified volume provides a large phase space that ultimately cancels the dependence on M_{Pl} . The differential cross section for producing a Kaluza-Klein graviton is, therefore, suppressed only by powers of $1/M_D$,

$$\frac{d^2\sigma}{dt dm} = S_{n-1} \frac{\bar{M}_{Pl}^2}{M_D^{2+n}} m^{n-1} \frac{d\sigma_m}{dt}, \quad (1.13)$$

where $d\sigma_m/dt$ is given by Eq. 1.11 and S_{n-1} is the surface of a unit-radius sphere in n dimensions⁹.

Since the entire KK tower would leak into the extra volume of space, the collider detector signature for a KK graviton produced in association with a photon (Eq. 1.11, Eq. 1.13) would be the presence of apparent missing transverse energy and the detection of a photon. There is a similar formulation for processes that involve direct graviton production in association with a jet [27]. However, this dissertation is devoted to study the process $q\bar{q} \rightarrow \gamma + G_{KK}$ only.

⁹For $n=2k$ (where k is the number of single KK modes in the summation) and k integer, $S_{n-1} = 2\pi^k/(n-1)!$ For $n=2k+1$, $S_{n-1} = 2\pi^k/\prod_{i=0}^{k-1}(i+\frac{1}{2})$

CHAPTER 2

EXPERIMENTAL APPARATUS

The Fermi National Accelerator Laboratory (Fermilab) [28] hosts the Tevatron Accelerator Complex [29, 30], a proton-antiproton ($p\bar{p}$) collider designed to produce high energy collisions at a center of mass energy of approximately 1.96 TeV [30]. Section 2.1 gives an overview of the process needed to achieve such energetic collisions.

The $D\bar{O}$ experiment is one of the two multipurpose detectors designed to study the secondary particles coming from these proton-antiproton collisions. A description of the coordinate system and conventions used in this detector is given in Section 2.2, while Section 2.3 describes its basic components.

2.1 The Tevatron Accelerator Complex

The Tevatron Accelerator Complex is made of several different accelerator systems [3]. The Pre-accelerator, Linac, and Booster are collectively known as the Proton Source. The Debuncher and Accumulator are referred to as the Antiproton Source. The Main Injector and the Tevatron, which are the largest systems, complete this machine. Figure 2.1 shows a graphical view the integrated system.

Producing high energy collisions begins with the production of negatively ionized hydrogen gas (H^-) at the Cockcroft-Walton generator. This gas is allowed to accelerate to an energy of 750 keV in the Pre-accelerator system. After the injection of these ions into the Linac, they are accelerated to an energy of 400 MeV. The Linac uses radio frequency (RF) fields to accomplish this acceleration. The first five RF stations use drift tube technology and the last seven use Klystron amplifiers.

After the beam is accelerated in the Linac, the 400 MeV H^- ions are sent to the Booster which strips the electrons off the ions, leaving only the proton. It accelerates these particles

to an energy of 8 GeV. The Booster is the first synchrotron in the chain of accelerators, it consists of a series of magnets arranged around a 75 m radius circle, with 18 RF cavities interspersed. The Main Injector (MI) is the second largest accelerator at Fermilab. It is a circular synchrotron with a circumference seven times larger than the Booster. With its 18 accelerating cavities, the MI can accelerate 8 GeV protons from the Booster to 120 GeV or 150 GeV, depending on whether the protons are used to stack¹ antiprotons or to inject beam into the Tevatron synchrotron. When loading the Tevatron with protons, seven bunches² are injected from the Booster and accelerated to 150 GeV. A process called coalescing makes one bunch out of the seven originals, and this coalesced bunch is extracted and sent into the Tevatron. By repeating this process 36 times, the protons for a 36×36 store³ are injected.

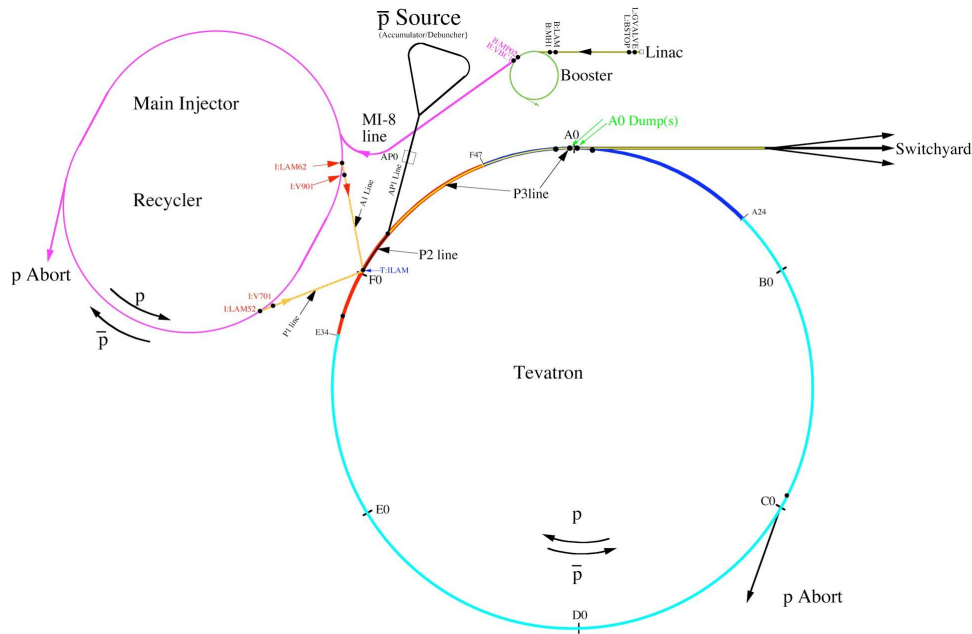


Figure 2.1: Different accelerators at Fermilab Tevatron Accelerator Complex [3].

The MI can also accept antiprotons from the Antiproton Source. Antiproton production [32] starts by striking 120 GeV protons from the MI to a nickel target, which produces a spray of all sorts of secondary particles. Magnets are then used to select antiprotons by their

¹The making of a stack of antiprotons.

²A bunch is a collection of particles revolving together within the Tevatron [31]

³The stable situation of 980 GeV proton and antiproton collisions.

momentum and charge. It is possible to collect 8 GeV antiprotons in this manner. They are then directed into the Debuncher.

The main purpose of the Debuncher is to capture pulses of antiprotons coming off the target and reduce their momentum spread by using an RF manipulation called bunch rotation and adiabatic debunching. The Debuncher maintains the beam at a constant energy of 8 GeV and uses beam-cooling systems (stochastic cooling technology) to make the beam more manageable. The antiproton beam is then transferred to the Accumulator which stores and cools 8 GeV antiprotons. The Accumulator is the second synchrotron of the antiproton source and it is housed in the same tunnel as the Debuncher. During shot setup⁴, four sets of seven bunches of antiprotons are extracted from the Accumulator and sent into the MI. Once there, the antiprotons are accelerated to 150 GeV, and coalesced, forming 4 coalesced bunches. These are then extracted and sent out into the Tevatron. This process is repeated nine times in a row to load the antiprotons for a 36×36 store.

The Recycler is an antiproton storage ring located along the ceiling of the Main Injector tunnel. This system was designed to recycle antiprotons from a Tevatron store. However, it is used only to stored antiprotons from the Antiproton Source. The Recycler does not accelerate particles, it only stores them at a constant kinetic energy of 8 GeV.

The Tevatron accelerator, the largest at Fermilab, is a circular synchrotron with eight accelerating cavities and a circumference of 6.3 km. It is the final destination for the beams of protons and antiprotons coming from the MI. The beams are accelerated from 150 GeV to 980 GeV. Once the final energy is reached, the two counter-rotating particle beams pass through each other for hours at a time, and can collide with each other at certain pre-determined points in order to produce interesting secondary particles.

2.2 Coordinate System and Units Convention

The DØ experiment uses a right handed coordinate system in which the z -axis is along the proton direction and the y -axis is upward with the origin being at the center of the detector. The azimuthal angle ϕ is defined with respect to the x -axis while the polar angle θ is defined with respect to the z -axis (Figure 2.2). Additionally, the r coordinate denotes the perpendicular distance from the z -axis.

⁴The act of extracting antiprotons from the Antiproton Source.

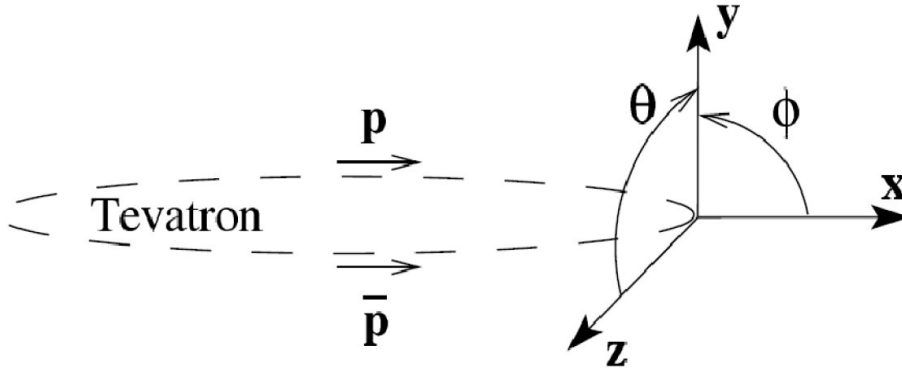


Figure 2.2: DØ coordinate system with respect to the Tevatron ring [4].

The distribution of the rapidity y is invariant under a Lorentz boost along the z -direction and it is defined by

$$y = \frac{1}{2} \ln \left(\frac{E + p_z}{E - p_z} \right). \quad (2.1)$$

In Eq. 2.1, p_z is the z -component of the momentum of the particle in question, and E is its energy. The pseudo-rapidity,

$$\eta \approx -\ln \tan(\theta/2), \quad (2.2)$$

is approximately equal to the rapidity y [1] in the limit where the particle can be considered massless. This is useful because $p\bar{p}$ collisions at the Tevatron are usually boosted along the z -axis and the final state particles are in the massless limit. Therefore, it is convenient to convert the angle θ to η using the transformation in Eq. 2.2. The term *forward* is used to describe the regions at large η .

The coordinates calculated using the detector origin $(0, 0, 0)$ are referred to as *detector* coordinates. It is frequently more useful, however, to define the coordinate system with respect to the location of the actual interaction point; these are called *physics* coordinates. A subscript may be used to differentiate between the two possibilities, although physics coordinates are assumed in the absence of any subscripts.

The solid angle ΔR defined by Eq. 2.3,

$$\Delta R = \sqrt{(\Delta\phi)^2 + (\Delta\eta)^2}, \quad (2.3)$$

where $\Delta\phi = \phi_1 - \phi_2$ and $\Delta\eta = \eta_1 - \eta_2$, is another important quantity used to describe the separation of two objects with coordinates (η, ϕ) , or to isolate objects in the detector.

In order to convert the measured rate of events into a cross section, the luminosity needs to be determined. The rate of a certain process can be calculated from the Lorentz invariant cross section σ and the luminosity \mathcal{L} as shown in Eq. 2.4,

$$\frac{dN}{dt} = \sigma \cdot \mathcal{L}. \quad (2.4)$$

The typical unit used at the Tevatron for cross sections is the pico-barn (10^{-36} cm²). Thus, the units of luminosity are pb⁻¹s⁻¹. When discussing a set of accumulated data, the time integrated luminosity $\int \mathcal{L}$ is used, whose units are pb⁻¹ or fb⁻¹ (10^3 pb⁻¹).

2.3 The DØ Detector

The DØ detector [33], a multipurpose particle detection system, operates at the Tevatron at a rate of one beam crossing every 396 ns. Figure 2.3 shows an overview of the main subsystems of the DØ detector. The central tracking system (Section 2.3.1) includes a silicon microstrip tracker and a scintillating-fiber tracker located within a 2 T solenoidal magnet. It provides the capability for precise measurements of particles position along their path from the interaction point. The next layer of detectors are the preshower system (Section 2.3.2) and the liquid-argon–uranium calorimeter (Section 2.3.3), which accurately measure the energy of most particles. The luminosity monitor, briefly outlined in Section 2.3.4, measures the inelastic $p\bar{p}$ cross section in order to determine the total integrated luminosity to which the DØ detector has been exposed. The muon spectrometer, a system that uses mini drift tubes and trigger scintillation counters, as well as a 1.8 T toroidal magnet to identify muons, is described in Section 2.3.5. Finally, a complex readout trigger-based system that records only those events with interesting physics signatures is described in Section 2.3.6.

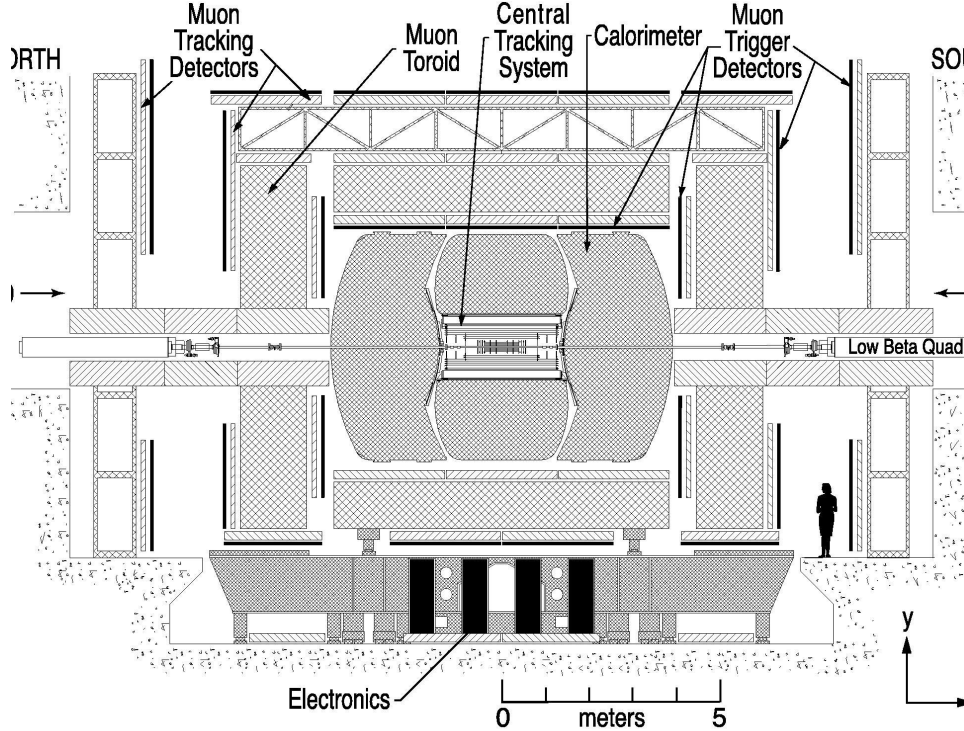


Figure 2.3: A cross-section view in the y - z plane of the DØ detector.

2.3.1 Tracking Detectors

The tracking system constitutes the first layer of detectors that surround the DØ beryllium beam pipe. Figure 2.4 shows its two main components, the silicon microstrip tracker (SMT), which is described in Section 2.3.1.1, and the central fiber tracker (CFT), described in Section 2.3.1.2. The 2 T solenoid magnet is also shown in the figure, along with the location of the preshower detectors, luminosity monitor and calorimeter. Both tracking detectors are part of the Run II DØ upgraded detector [33], and were designed to provide excellent determination of the flight path of charged particles, necessary for studies of top quark, electroweak, and b physics, and to search for new phenomena.

The two tracking detectors locate the primary interaction vertex with a resolution of about $35 \mu\text{m}$ in r - z , and measure track impact parameters for b -quark jets identification with a precision better than $15 \mu\text{m}$ in r - ϕ for particles with transverse momentum $p_T > 10 \text{ GeV}$ at $|\eta| = 0$. The magnetic field provides a calorimeter-independent way of determining the p_T

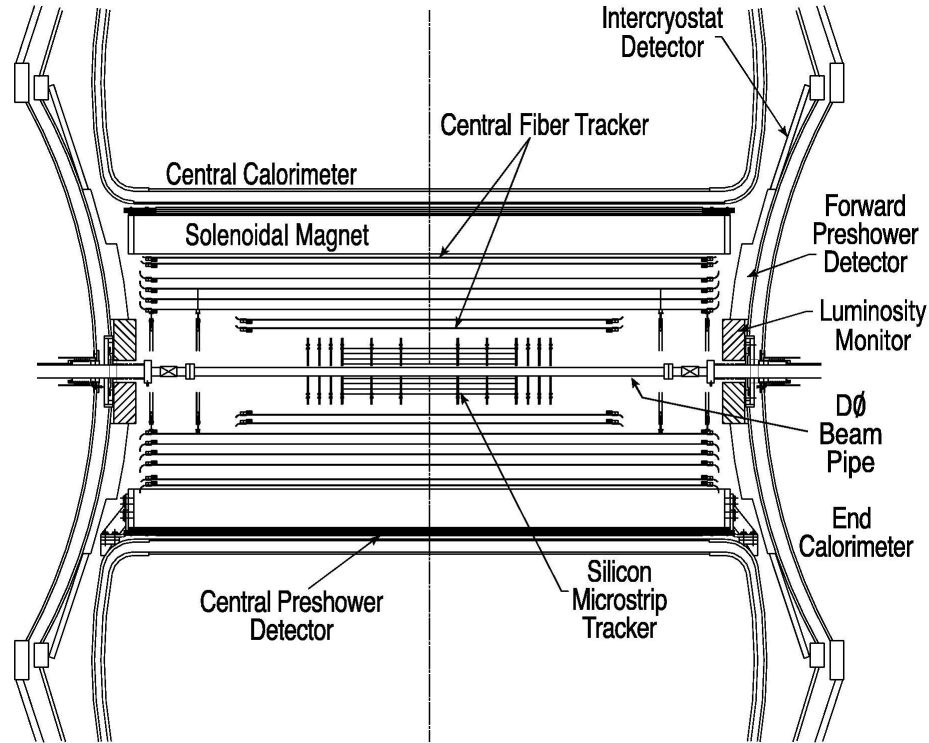


Figure 2.4: A cross-section view in the y - z plane of the central tracking system. Also shown are the solenoid, the preshower detectors, luminosity monitor, and the calorimeter.

of charged particles. The transverse momentum thus measured can then be compared to the transverse energy E_T in the calorimeter in order to tune the energy scale of electromagnetic particles.

2.3.1.1 Silicon Microstrip Tracker (SMT)

The silicon microstrip tracker (SMT) [34, 35] is the closest subsystem to the beam pipe and provides track and vertex reconstruction capabilities over the pseudo-rapidity coverage η of the DØ detector. It is a collection of doped silicon detectors and consists of six central barrel segments interspaced with disks as shown in Figure 2.5. There are 12 central F-disks and 4 forward H-disk detectors⁵.

The barrels are 12 cm long and consist of 72 silicon modules called *ladders* arranged

⁵The outer H-disks were removed in the latest upgrade of the detector in 2006.

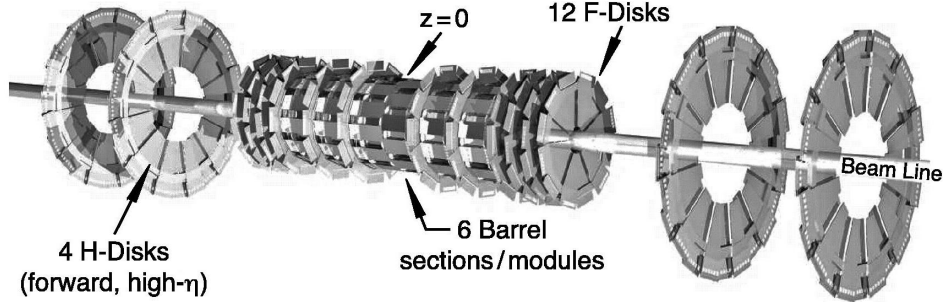


Figure 2.5: Schematic of the silicon microstrip tracker detector.

in eight layers with pairs of layers forming super-layers. Each barrel has four super-layers. Super-layers 1 and 3 have single layer sensors (SS) in the two outer barrels (in the beam direction), and use double sided double metal (DSDM) technology with 90° stereo angle in the four central barrels. Double sided (DS) ladders with $\sim 2^\circ$ stereo are used in super-layers 2 and 4 in all barrels. There are 432 ladders in total.

The 12 F-disks are composed of 12 DS wedge 30° stereo detectors while the H-disks, covering the most forward tracking region, consist of 24 pairs of SS detectors glued back to back. There are 144 F-wedges and 96 H-wedges in the tracker. The total number of readout modules is 912, with nearly 793 thousand channels. These detectors are read out by custom-made 128-channel SVXIIe readout chips. Additionally, there is a radiation-hard layer (Layer 0), which was recently installed [36] in the space between the beam pipe and the innermost barrel layers. Layer 0 has a single layer geometry arranged in a barrel design. The sensors are mounted in a fiber carbon support structure, which is supported from the beam tube. The SVX4 readout chips used by this system are not placed on the sensor because of lack of space and insufficient cooling. Instead, analog cables are used to transmit the unamplified signal to a hybrid for digitization. Layer 0 significantly improves the impact parameter resolution.

2.3.1.2 Central Fiber Tracker (CFT)

The central fiber tracker (CFT) [37] combines with the SMT detector to provide charged particle tracking. The CFT is constructed of scintillating fibers of $835 \mu\text{m}$ diameter and 1.66 or 2.52 m axial length that are connected to clear fiber waveguides of identical diameter

and typically 7.8 to 11.90 m long. The 32 concentric layers of scintillating fibers are arranged in eight barrels, each consisting of two doublet layers, one with zu and one with zv configuration (z is an axial layer; u and v have a stereo angle of $\pm 3^\circ$). The light generated by charged particles traversing the fibers is converted into electrical signals by visible light photon counters (VLPCs) housed in VLPC cassettes. VLPCs are solid state avalanche photodetectors based on silicon diodes with an operating temperature of 9 K and quantum efficiency of 75%. The CFT requires 76,800 channels of VLPC readout. Figure 2.6 shows a schematic view of the CFT layers and their associated waveguides.

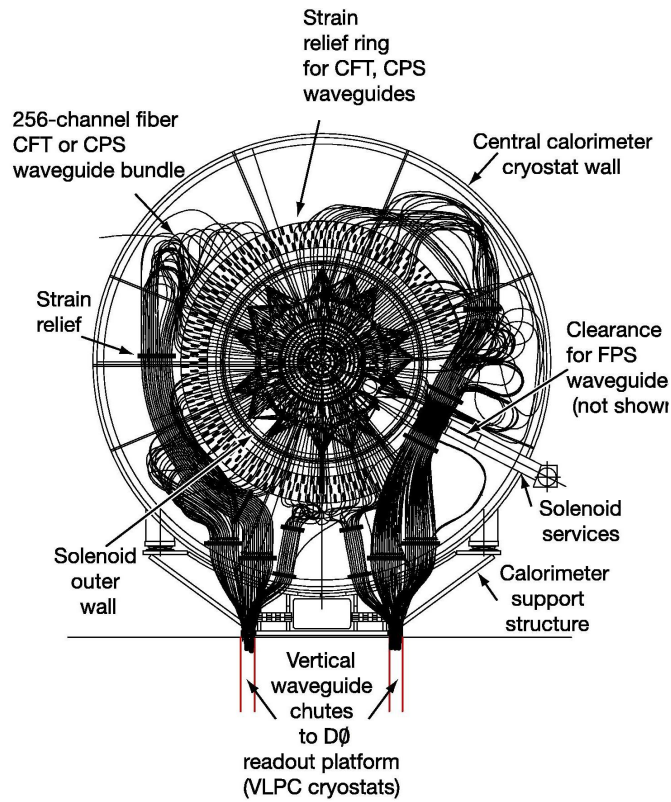


Figure 2.6: Schematic endview of the central fiber tracker with its associated waveguides.

2.3.2 Preshower Detectors

The preshower detectors can be thought of as a hybrid between tracking and calorimeter detectors. They enhance electron identification capabilities by improving, with its position measurement, the quality of the match between tracks in the tracking detectors and clusters in the calorimeter. Photon identification also benefits from the improved cluster position determination. The energy deposited in the calorimeter, degraded mainly by the presence of the solenoid, can also be corrected using information from the preshower detectors. Their fast measurement of position and energy, and the distinctive shape of their clusters, allow the preshower information to be included in the Level 1 trigger (Section 2.3.6.1), as well as to be used in offline background rejection.

The central preshower detector (CPS) [38] is located between the solenoid magnet and the calorimeter, covering $|\eta| < 1.31$. A lead radiator, of approximately one radiation length⁶ (X_0) thick, sits in front of the CPS system.

The CPS is built with three concentric cylindrical layers of triangular extruded strips made of scintillating plastic embedded with wavelength shifting (WLS) fibers. When a charged particle crosses a layer, the ionization energy is collected in form of light by the WLS and transported to the end of the detector. Light is then transmitted for readout to the same VLPC system used by the CFT through clear fibers. The triangular shape of the strips and the nested geometry (Figure 2.7) typically allows a particle to pass through multiple strips, making strip-to-strip interpolations possible, which directly improves the precision of the position measurement.

The strips in the innermost (axial) layer are parallel to the beam pipe while the additional layers, u -stereo and v -stereo, are arranged at angles of 23.774° and 24.016° , respectively, with respect to the axial layer. This configuration makes it possible to reconstruct three-dimensional clusters in the system. Each layer is formed from eight octant modules with the WLS fibers split at $z = 0$ and read out from each end. There are, in total, 2560 readout channels per layer.

A forward preshower detector (FPS) [39] is mounted on each of the calorimeter endcaps. They are made of the same scintillating triangular strips used in the CPS, but with a trapezoidal modular arrangement. Each module consists of two layers separated by a $2X_0$ -

⁶One radiation length (X_0) is roughly the distance an electron or photon will travel before undergoing bremsstrahlung or decaying into a e^+e^- pair, respectively.

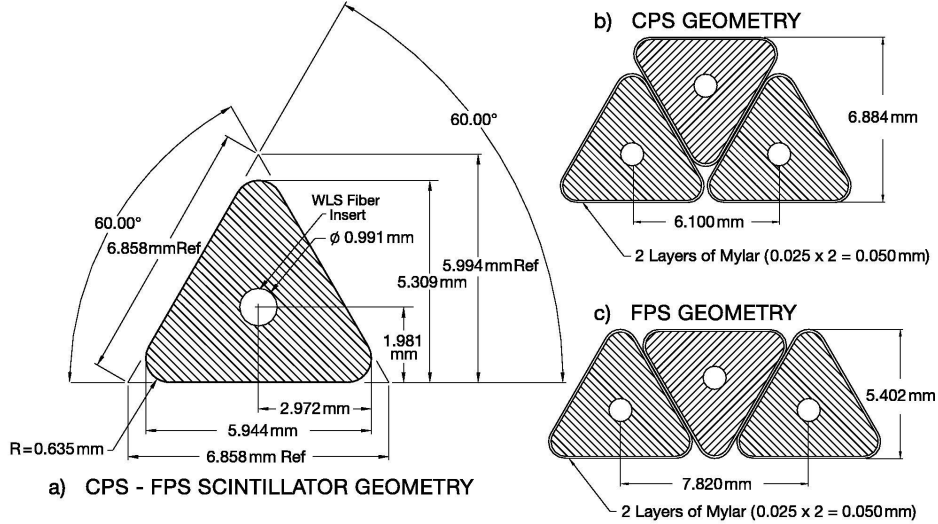


Figure 2.7: Cross section of the scintillating strips used in the CPS and FPS. The circles indicate the location of the embedded wavelength shifting fibers.

thick-lead-stainless-steel absorber; the inner layer is called the minimum ionizing particle (or MIP) layer where minimum ionizing signals from charged particles are registered; the outer layer is called the shower layer where particles, like electrons and photons, deposit their energy after showering in the absorber. Each layer is made of two planes of scintillator strips aligned at different pitches in order to allow for three-dimensional position reconstruction. The shower layer covers the region $1.5 < |\eta| < 2.5$ and the MIP layer and the absorber cover the region $1.65 < |\eta| < 2.5$

2.3.3 Calorimeter

The main purpose of the $D\phi$ calorimeter [40] is to provide position and energy measurement of most long-lived particles, as well as to help in particle identification through the determination of the shower shape topology of different electromagnetic (EM) and strongly interacting particles.

The calorimeter consists of one central sub-detector, or central calorimeter (CC), covering the region $|\eta| < 1.1$, and two end-cap (EC) detectors covering $1.3 < |\eta| < 4$, each of them encased in their own cryostat (Figure 2.8). Each region is subdivided in an electromagnetic

section, closest to the interaction region, followed by a fine and coarse hadronic (HD) sections.

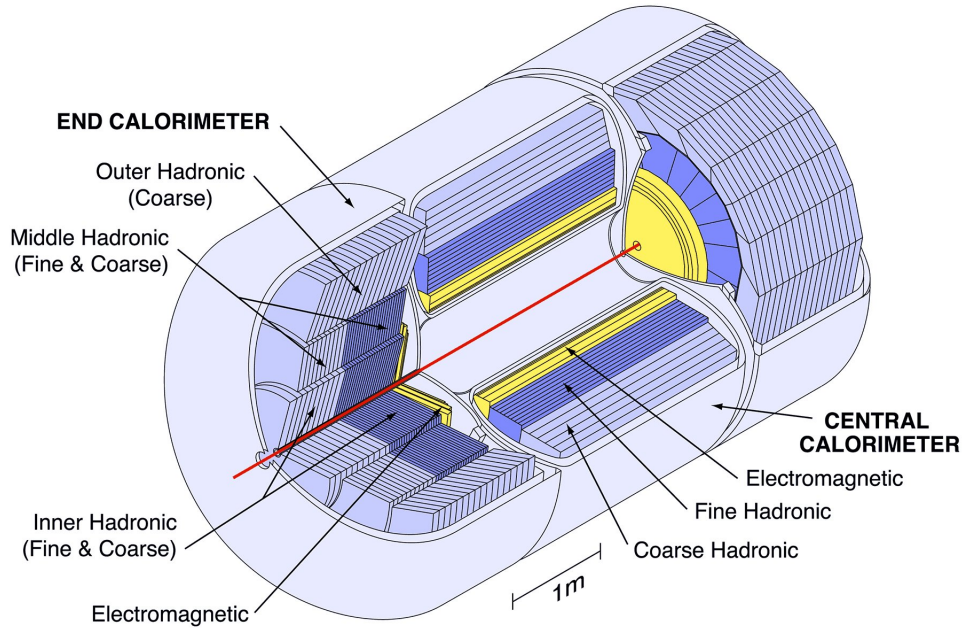


Figure 2.8: The DØ calorimeter..

All calorimeter regions consist of cells (Figure 2.9) with liquid argon as the active medium, and grounded absorber plates whose material changes depending on the section type. In the case of electromagnetic sections, it is made from nearly pure depleted uranium, whereas an uranium-niobium alloy is used in the fine hadronic sections. The coarse hadronic absorbers are made of copper (in the CC) or stainless steel (in the EC). High voltage pads complete the calorimeter cell design. These pads measure the energy deposited in the cell by collecting the charge resulting from the ionization of the liquid argon. The ionization is triggered by a shower of secondary particles that are produced when a particle interacts with the absorber plates.

The calorimeter cells are arranged in four electromagnetic layers, three fine hadronic layers (four in the EC), and one coarse hadronic layer. All these layers form pseudo-projective towers as seen in Fig 2.10. In addition, EC hadronic layers are further divided into inner, middle and outer hadronic sections. At $\eta = 0$, the CC has a total of 7.2 nuclear absorption lengths (λ_A).

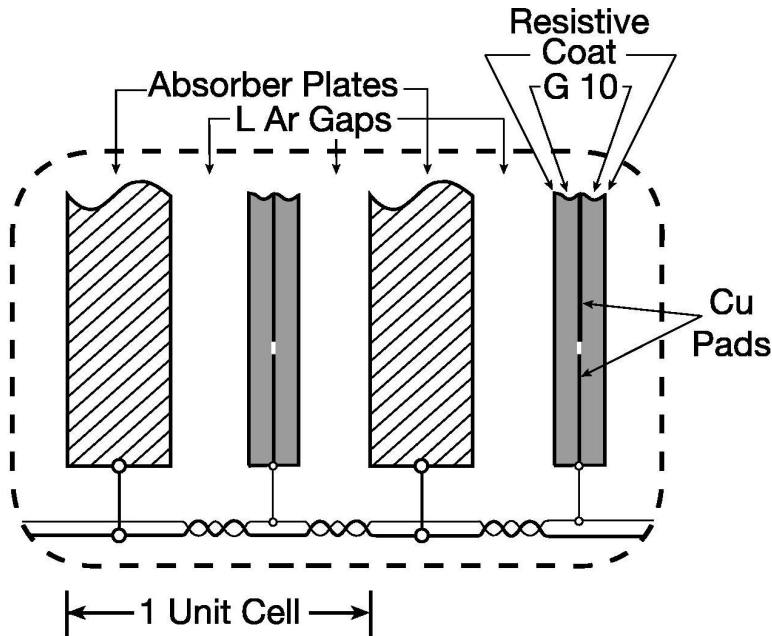


Figure 2.9: DØ calorimeter cell.

The DØ calorimeter is finely segmented in the transverse and longitudinal directions, which allows for precise measurement of shower position and shape. The typical cell subtends an area of 0.1×0.1 in $\eta - \phi$ space, with the exception of the third electromagnetic layer where the segmentation is 0.05×0.05 in $\eta - \phi$. The finer segmentation is due to the expectation for electrons and photons electromagnetic showers to reach their maximum in the third layer. Cell sizes increase at larger η in order to avoid small cells.

In order to accommodate beam crossings occurring every 396 ns, and taking into account the electron drift time across the liquid-argon gap of approximately 450 ns, a base line subtraction (BLS) system is implemented to handle the effects of pile-up⁷. There are close to 50,000 electronic channels to be read out in the calorimeter. The readout chain (Figure 2.11) starts with the charge being collected at the cell pads; it is then transported to the readout electronics via coaxial cables and integrated in a preamplifier system. The output signal is later shaped and filtered in the BLS circuitry. The BLS uses switched capacitor arrays

⁷More than one event in the detector due to multiple interactions in a single beam or to interactions in multiple beam crossings [33].

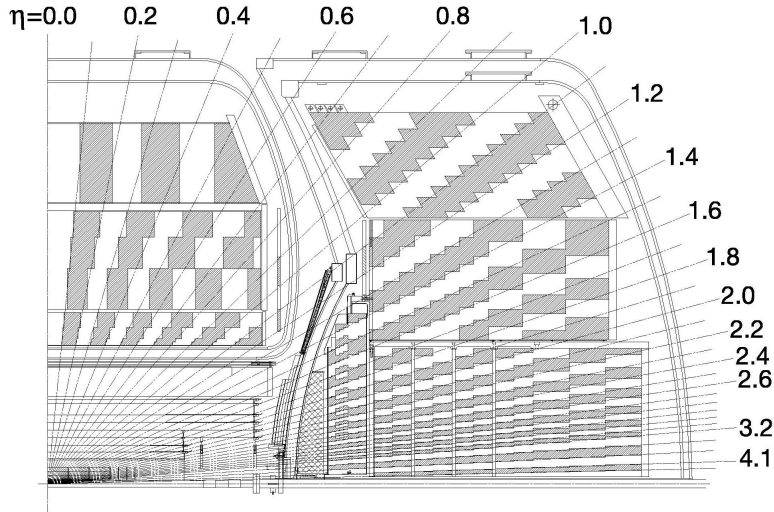


Figure 2.10: Schematic view of a portion of the DØ detector.

(SCA) to store the signal until Level 1 (Section 2.3.6.1) and Level 2 (Section 2.3.6.2) trigger decisions are made. The SCAs store two gain paths separately (gain x1 and gain x8) in order to extend the ADC readout dynamic range. Upon positive trigger decision, the precision signals from the BLS are transmitted to the analog to digital converters (ADCs). These signals are then subject to Level 3 (Section 2.3.6.3) decision and, if accepted, are recorded to tape alongside the rest of the event information.

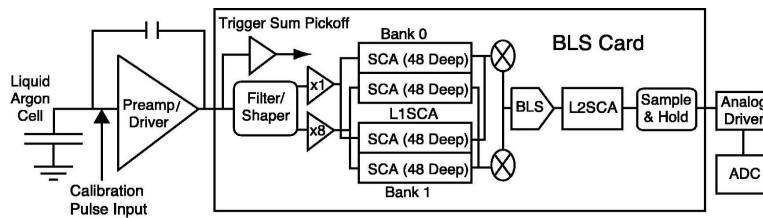


Figure 2.11: Readout chain of the calorimeter.

In order to address the problem of substantial unsampled material in the region $0.8 < |\eta| < 1.4$, which degrades the energy resolution, additional layers of sampling are added. Single-cell structures, called massless gaps, sit in front of the first layer of uranium within

the central and end cryostats. Due to the cryogenic and electrical services for the solenoid, as well as the inner tracking system cabling that is routed between the CC and the ECs, two intercryostat detectors, consisting of scintillating tiles, are present in these gaps to give additional coverage for calorimetry.

2.3.4 Luminosity Monitor

To properly normalize all the data collected by the DØ detector, it is of vital importance to gather information about the $p\bar{p}$ inelastic collisions. This is achieved by the luminosity monitor (LM), which consists of luminosity counters made of two sets of 24 plastic scintillators. They are located in front of the end-cap calorimeters and cover a range of $2.7 < |\eta| < 4.4$. The averaged number of inelastic collisions per beam crossing N_{LM} is used to determine the luminosity: $\mathcal{L} = f \cdot N_{LM}/\sigma_{LM}$ where f is the beam crossing frequency and σ_{LM} is the effective cross-section for the LM that takes into account the acceptance and efficiency of the LM detector.

When a charged fragment from the break-up of the protons in the $p\bar{p}$ collision transverse the detector, the scintillators produce light which is collected by photo-multiplier tubes (PMT). A schematic of the luminosity monitor can be seen in Figure 2.12.

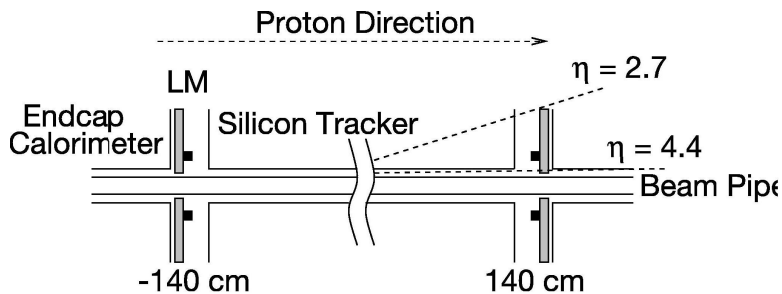


Figure 2.12: Schematic showing the location of the luminosity counters.

The LM detectors can also be used to measure the beam halo and estimate the z -position of the interaction vertex. The time-of-flight, measured for particles striking the LM detectors placed at ± 140 cm, plays an important role in determining these two quantities. A fast calculation of the z -coordinate of the interaction vertex, z_v , can be estimated using the expression $z_v = \frac{c}{2}(t_- - t_+)$, where t_+ and t_- are the times-of-flight measured by the North (+)

and South (–) detectors, respectively. Beam halo particles are eliminated by a requirement $|z_v| < 100$.

2.3.5 Muon Spectrometer

Muons behave as minimum ionizing particles, i.e., they do not deposit significant amounts of energy in the tracker or in the calorimeter. Therefore, a standalone system was built to detect these leptons. The muon spectrometer consists of an arrangement of drift tubes (wire chambers) and scintillating tiles, plus a toroidal magnet with an iron yoke in order to bend the muons from their original paths. This allows for local, tracker-independent momentum measurement. The iron yoke suppresses the leakage of very high energetic jets into the muon system (punch through particles), and stops muons with $p_T \leq 3$ GeV.

The central muon system covers the region $|\eta| < 1$ and the forward system does the same with the region $1 < |\eta| < 2$. The scintillation counters are used for muon identification and fast triggering, while the wire chambers help in precise coordinate measurement, as well as triggering. These detectors form a three layer system (an A-layer located inside the toroidal magnet, and B- and C- layers outside the toroidal magnet) in both the central and forward regions. Figure 2.13 and 2.14 show the exploded views of both types of detectors.

The scintillator counters produce light when the muon passes through the detector; this light is then collected by a PMT. The drift chambers are filled with gas that is ionized by the passage of a charged particle. High voltage sense-wires are responsible for collecting the charge. Proportional drift tube (PDT) technology is used in the central region, while the forward region uses smaller drift chambers called mini drift tubes (MDT).

A hole, ranging in ϕ from 225° to 310° , in the bottom A-layer in the central region is necessary for the structural support of the calorimeter. The A-layer contains four sub-layers of PDTs, except at the bottom of the detector where there are three sub-layers. The B- and C- layers contain three sub-layers of PDTs. Two layers of scintillators are added inside the A-layer (A- ϕ counters) and outside the B- and C- layers (cosmic cap and bottom counters) to provide fast timing signal for triggering and cosmic ray background discrimination.

In the forward region, each layer of MDTs are divided into octants consisting of three (for the B- and C- layers) or four (for the A-layer) planes of tubes oriented along the field lines. All three layers of muon chambers are covered with a layer of scintillator pixels. A shielding system, as seen in Figure 2.3, was built in order to reduce the background due to

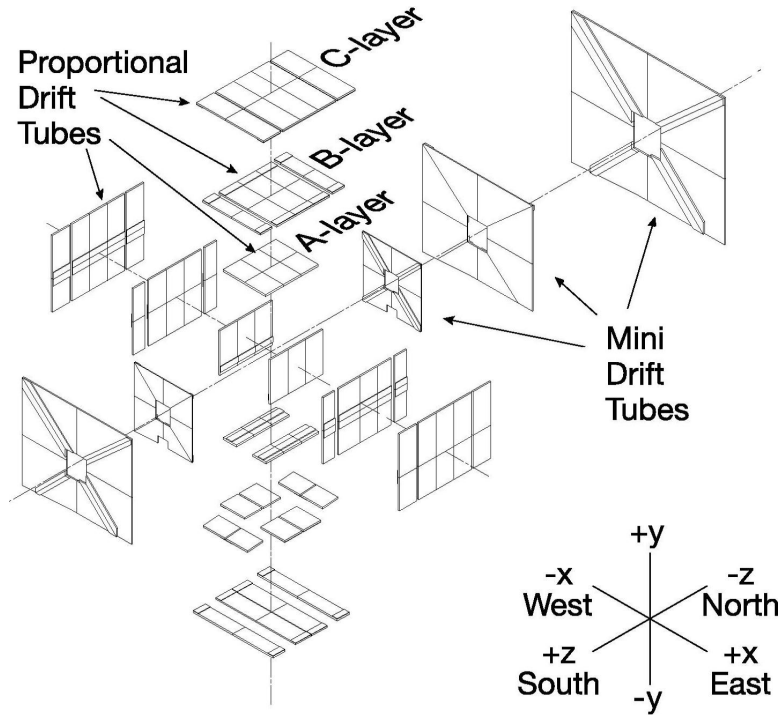


Figure 2.13: Exploded view of the DØ drift tubes.

beam halo particles and proton and antiproton remnants. The shielding is made of layers of iron, polyethylene, and lead in a steel structure that surrounds the beam pipe and low-beta quadrupole magnets.

2.3.6 Trigger and Data Acquisition

Collisions are seen in the DØ detector at a frequency of about 1.7 MHz. Because of technical and financial constraints, this rate is too high for all events to be recorded. Therefore, a three-level trigger system has been implemented in order to reduce the rate to about 100 Hz of interesting physics events. The DØ trigger system starts at Level 1 (L1, Section 2.3.6.1). The L1 trigger is based on custom-made hardware and firmware and it reduces the rate to about 2 kHz. The second stage, called Level 2 (L2, Section 2.3.6.2), uses hardware engines and single board computers (SBC) running simple software algorithms to reduce the rate to 1 kHz. The Level 3 (L3, Section 2.3.6.3) receives candidates that pass L1 and L2 and uses more sophisticated algorithms that run in a farm of computers. It reduces the rate

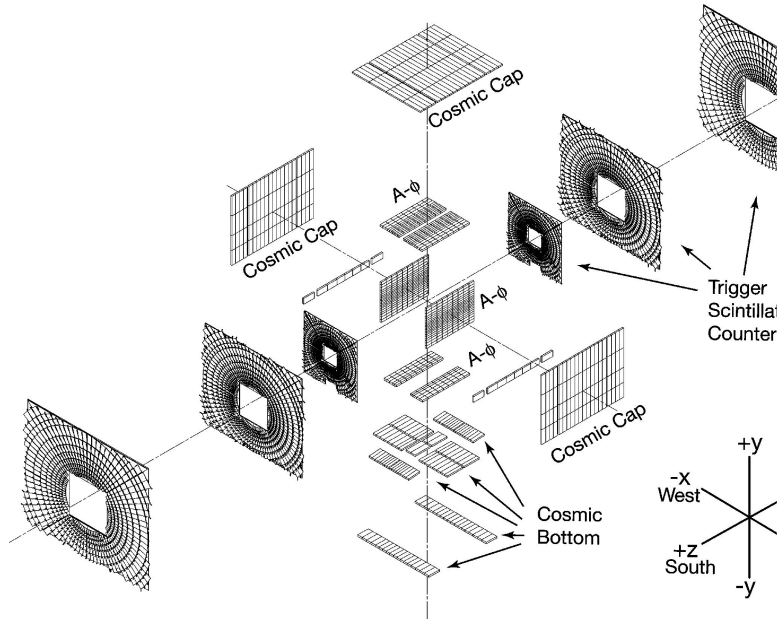


Figure 2.14: Exploded view of the DØ muon scintillators.

to about 100 Hz, making it possible to record the event candidates to tape for later offline reconstruction. Different trigger definitions are formed by applying certain requirements at the three distinct levels of the trigger architecture. Every event written to tape has to satisfy at least one of these trigger definitions, which are basically a specific *AND* condition on L1, L2, and L3 requirements. The nomenclature of the triggers gives some information about the requirements that are applied. For instance, the trigger E1_SHT27 indicates that at least one EM object is selected at L1, and that it is found satisfying tight shower shape requirements (with $p_T > 27$ GeV) at L3. Some of these triggers are *prescaled* at the L1 stage if their firing rate is too high. If a trigger has a prescale of 5, then only one out of 5 events that satisfy the L1 requirement is randomly selected to continue the trigger chain. A collection of trigger definitions forms a trigger list. These lists are defined for different ranges of instantaneous luminosities in order to optimize the accept rates at the different trigger levels. Over time, it is necessary to update the trigger lists to cope with detector upgrades, increasing instantaneous luminosities, or to improve efficiency. As a consequence, there are various versions of trigger lists. The trigger system is tightly integrated with the DØ data acquisition system (Section 2.3.6.4), as illustrated in Figure 2.15.

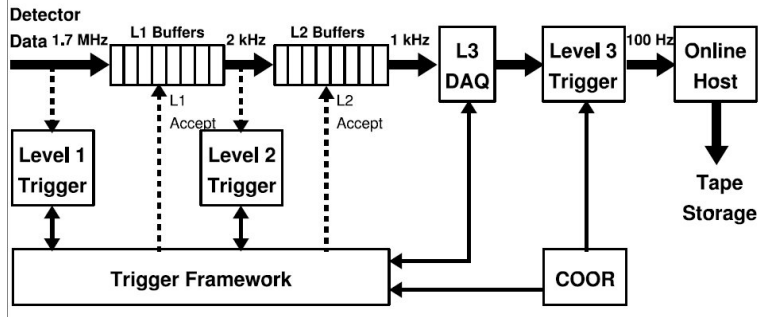


Figure 2.15: Overview of the DØ trigger and data acquisition systems.

2.3.6.1 The Level 1 trigger

Level 1 trigger collects information that was read out from all subsystems of the detector with the exception of the SMT. It uses specialized hardware to examine every event for interesting signatures, calculates trigger terms (trigger decisions), and sends the results to the trigger framework (TFW). The TFW is the specialized manager for the trigger system; it gathers information from all the L1 trigger devices and makes a decision on whether a particular event is accepted to continue through the trigger chain. The TFW is built out of 9U 400 mm cards housed in customized VME crates, and performs a series of different tasks like coordinating trigger vetoes, providing and implementing trigger prescaling, correlating the trigger and readout functions, as well as managing the communication tasks between the front-end electronics and the trigger control computer (TCC). After the L1 stage, the events rate is reduced to 2 kHz.

The Level 1 calorimeter trigger (L1Cal) form trigger towers, in the EM and HD sections, that are made up from a combination of four calorimeter towers, i.e., towers of size 0.2×0.2 in $\eta \times \phi$. The energies, which are sums of fast analog pickoffs from the BLS circuit, are converted to E_T . In an earlier stage of the DØ detector, thresholds on the trigger tower E_T were used to calculate trigger terms. However, after a later upgrade [41], the transverse energy of clusters of trigger towers are used instead. Clustering of trigger towers are accomplished in three steps [42]. First, the E_T of various trigger towers are summed to form trigger tower clusters. This operation is executed for each trigger tower, observing shower shape differences between different objects like jets, electrons or photons, and taus. In the second step, local

maxima are determined in the trigger tower cluster space by comparing adjacent trigger tower clusters and setting a particular spatial separation between them to avoid multiple counting. Finally, in the third phase, simple versions of higher-level requirements, like isolation or (EM/HD) energy fraction for EM objects, or the addition of energy of surrounding trigger towers to improve the total jet object energy are performed. Additionally, the L1CTT trigger (described below) is used to find tracks by matching the ϕ position of EM and jet objects from the L1Cal trigger. This element, called L1CalTrack trigger employs the L1Muon architecture (described below) with small modifications.

The Level 1 central track trigger (L1CTT) provides a fast way of searching for tracks exceeding predefined p_T thresholds with data provided by three scintillator-based detectors: the CFT and the central and forward preshower detectors (described earlier in this chapter). The trigger is divided into 4.4° wedges in ϕ . The data from the CFT fiber hits is compared against approximately 20,000 predefined hit patterns and grouped in p_T bins. The track candidates are sorted, matched to CPS clusters (axial), and counted. The list of tracks are then sent to the L1Muon (see below) or L1Cal to search for matches in the muon detector or in the calorimeter, respectively. After checking for isolation, the resulting trigger terms are sent to the TFW for an L1 global decision. The CPS stereo subsystem, even though does not generate trigger terms, contributes with additional hits information, after an L1 decision has been made. This can later be used by the Level 2 stage of the trigger. The FPS subsystem of the trigger produces its own set of L1 trigger terms. It searches for clusters of hits in the FPS fiber layers. Counts of these clusters are summed and used to make L1 trigger terms which are later sent to the TFW for a global decision. The FPS subsystem also feeds the higher levels of the trigger chain with more discriminating information.

The Level 1 muon trigger (L1Muon) system is responsible for searching muon patterns using the hits in the wire chambers, muon scintillation counters, and tracks from the L1CTT. Up to 480 tracks from the L1CTT can be compared with the information from about 60,000 muon channels for every bunch crossing. Loose (track matched to A-layer scintillator) and tight (track matched to a scintillator road using the A- and B- layers) triggers for different p_T thresholds can be formed by matching central tracks from the L1CTT to hits in the muon scintillator system. Triggers can also be made based on track stubs formed in the wire chambers that are confirmed by the presence of scintillator hits in two or three layers of the muon system. The L1Muon is divided into central and forward regions, and eight octants in

ϕ .

2.3.6.2 The Level 2 trigger

The Level 2 trigger (L2) system was designed to provide a more sophisticated pre-processing of the data collected at the front-ends and accepted by the L1 trigger system. L2 applies fast reconstruction algorithms on data across the detectors to form crude physics objects. The information of the subsystems, handled by preprocessors running in parallel, is combined into a global L2 processor (L2Global) to test for correlations in physics signatures. The L2 trigger can reduce the event rate by a factor of 10, if necessary. Typically, it delivers output rates on the order of 1 KHz.

The L2 system uses 9U VME crates built to the VME64/VIPA standard. The crates are instrumented for fast intra-crate data flow and communication, and house commercially produced SBCs mounted on adapter cards.

The L2 calorimeter preprocessor system consists of three algorithms designed to identify jets, identify electrons and photons, and to calculate the event missing transverse energy (\cancel{E}_T) for the global processor. The information of all 2560 calorimeter trigger towers are used. Jets are built from 5×5 towers centered on the seed tower. All towers passing the 2 GeV threshold are used as seed towers. Electrons and photons are built from seeds with $E_T > 1$ GeV in the EM layers of the calorimeter and consist of 3×3 clusters. An event \cancel{E}_T is also calculated. The final list of objects is passed to L2Global which applies the different trigger list requirements.

The quality of muon candidates is improved by the L2Muon system which uses calibration and more precise timing information. Track segments from the A-layer are combined with those from the B- and C- layers to provide momentum measurements. A quality value handle is assigned based on the number of hits, and (η, ϕ) coordinates are provided.

The L2 preshower system (L2PS) provide evidence for early shower development and give a good spatial point for comparison with calorimeter clusters or tracks. Stereo hits from the CPS and FPS are combined with the axial hits used in L1 trigger to form three-dimensional clusters. The results from both subsystems are transmitted to the global L2 processor for correlation with the information from other detector components.

After a L1 accept, the L2CTT preprocessor receives a list of tracks from the L1CTT. This list, as well as SMT data, are also sent to the silicon track trigger system (L2STT). The

L2STT uses the tracks from the L1CTT as seeds to find tracks in the SMT. These refined tracks have an impact parameter (which can be used for triggering on the displaced vertices found in b -jets) and improved p_T measurement. The output is transmitted to the L2CTT which refines the track ϕ and projects the track location into the calorimeter. An isolation is also calculated taking into account the occupancy of the CFT near the track in question.

Finally, the L2Global makes the trigger decisions based on the objects identified by the L2 preprocessors.

2.3.6.3 The Level 3 trigger

The Level 3 trigger system (L3) is a set of algorithms executed in a collection of farm nodes. The goal of this system is to reduce the nominal 1 kHz input rate to 100 Hz for data recorded⁸ for offline analysis. This trigger uses the full detector readout to select events, which requires data from all sub-detector to be transmitted to the farm nodes. L3 makes use of more sophisticated conditions to select events; for example, the angle between objects or the invariant mass can be used as additional handles. Object-specific algorithms, called filter tools, are employed to generate such physics objects.

The L3 jet tool bases its jet reconstruction on the high-precision calorimeter readout and depends heavily on the primary vertex determination, because jet selection is made on transverse energy. A simple cone algorithm is implemented and hot calorimeter cells are suppressed in order to sharpen the trigger turn-on.

The L3 electron tool uses a fast version of the offline code for electron identification. The trigger decision is based on a combination of a simple $\Delta R = 0.25$ jet cone requirement, a cut on the energy fraction in the electromagnetic calorimeter (> 0.9), requirements on \cancel{E}_T , and a requirement on the transverse shower shape of the EM cluster. A match to a preshower detector signal can also be required.

The L3 \cancel{E}_T tool calculates \cancel{E}_T by using the calorimeter cell information (assuming a nominal $(x, y, z) = (0, 0, 0)$) grouped in pseudo-rapidity ring sums. This tool performs a fast geometrical recalculation to correct the \cancel{E}_T value after the primary vertex has been determined. The \cancel{E}_T filter can be added to any other filter in order to provide additional rejection power.

⁸In practice, the L3 output rate oscillates between 100 to a maximum of 150 Hz.

Like the electron tool, the L3 muon tool consists of a simpler and faster version of the offline muon reconstruction code and runs on the L3 farms. The L2 trigger dictates the region and the type of data that needs to be unpacked by L3 muon for fast reconstruction. This tool improves the overall ability of L2 to identify muon candidates by, for instance, applying more sophisticated timing discrimination, track matching, isolation, etc.

The L3 tracking tool finds tracks by unpacking the CFT and SMT information and forming clusters with specific L2 algorithms. Since the outer CFT layers have the lowest occupancy, the track finding starts from outside in. The track seeds, which satisfy an equation describing a straight track of certain p_T threshold, predict the region in which the next possible hits should lie in. This forms a series of layer links. Candidate tracks are built by adding more links with a curvature consistent with the preceding link. To build three dimensional tracks, a histogramming method is used. The found tracks are propagated into the SMT where hits are added if they fulfill the extrapolation prediction. The track with SMT hits is kept if its χ^2 is better than that of the CFT-only track. L3 tracks are used as standalone trigger objects by the rest of the L3 tools.

2.3.6.4 Data acquisition systems

The Level 3 data acquisition (L3DAQ) is responsible for transmitting the data from the VME readout crates over Ethernet cables to the farm nodes, as well as distributing the information out from the L3 farm nodes for logging and monitoring tasks. The overall coordination and control of triggering and data acquisition are managed by a program called COOR running on the on-line host system.

An SBC, located in each VME crate, collects the crate data and sends it to one or more farm nodes previously defined by the *routing master* process which itself consists of a dedicated SBC. A process called the *event builder*, running on each farm node, builds a complete event from event fragments and organizes them into a readable format for the L3 trigger software. The event is dropped if one of the fragments is missing. The supervisor process provides the interface between the main $D\emptyset$ run control program (COOR) and the L3DAQ system. Figure 2.16 shows a schematic diagram of communication and data flow in the system. Events that pass the L3 trigger are sent to a machine called the Collector for temporary storage. When enough events are accumulated, the data are stored on a machine called the Datalogger and finally sent to be stored on tape.

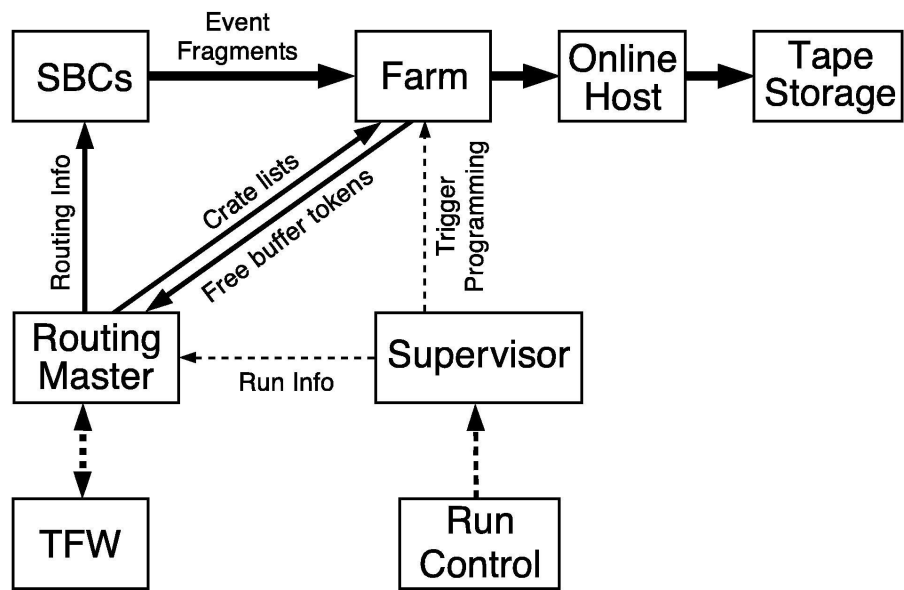


Figure 2.16: Schematic illustration of the information and data flow through the L3DAQ system.

CHAPTER 3

EVENT RECONSTRUCTION

The raw data recorded by DØ detector consists primarily of digitized electronic signals that result from the integration of collected charge, the light yields in scintillators, the time differences from drift chambers, etc. Data in this format is not convenient for doing physics analyses; it needs to be decoded and translated into a more useful format. This is accomplished by the DØ Offline Reconstruction Program (RECO) [43], which is responsible for reconstructing objects that are later used to perform all the DØ physics analyses.

The reconstruction program is run on the offline production farms and it is based on the DØ Event Data Model [44]. It takes as input the information created either by the L3 trigger system or by Monte Carlo (MC) simulation, and delivers data with recognizable reconstructed object information, organized in a convenient format.

In the first step of the reconstruction chain, the reconstruction program unpacks the digitized signals from the detector, associates the electronic channels with physical detector elements, and applies detector specific calibration constants. The second step is the most computer-intensive and consists of reconstructing global tracks using the hits in the SMT and CFT detectors. These tracks are stored and later become the input to the third level in the reconstruction: vertexing. In this third step, primary (location of $p\bar{p}$ interactions) and secondary (associated with decay of long-lived particles) vertices are identified and stored. In the final step, higher level objects such as electromagnetic particle candidates (electrons and photons), muons, neutrinos (\cancel{E}_T), and jet candidates are reconstructed based on specific sub-detector information, track, and vertex objects.

Each of the steps mentioned above involve complex algorithms. A general overview is presented in the following subsections. The interested reader should check the appropriate references for a more thorough description.

3.1 Track Reconstruction

Particles traversing the tracker ionize its sensitive elements and deposit energy in the SMT silicon strips or the CFT fibers. Activated channels in these sub-detectors are then spatially clustered. The energy weighted centroids of these clusters are fed to two tracking algorithms that run in parallel and form a pool of candidate tracks (track hypotheses).

The Alternative Algorithm (AA) [5], described in Section 3.1.1, constructs a large pool of track hypotheses by extending seed clusters of tracking hits from the SMT to the rest of the tracking system. It filters down the number of track candidates based on well defined criteria and eliminates all overlapping hypotheses until no more tracks remain in the pool.

The Histogramming Track Finder (HTF) [6], detailed in Section 3.1.2, finds tracks by filling a histogram in the track parameter space (track curvature and azimuthal angle) with values consistent with each hit in the CFT and the SMT. Hits from the same particle will produce a peak in the histogram whereas random hits will uniformly populate the space.

3.1.1 The Alternative Algorithm

In this method, an initial track hypothesis is constructed from three two-dimensional hits in the SMT barrels or disks. The selection of hits starts at the inner-most layer and extrapolates to the outer-most layer of the tracking system. There are certain conditions to form a track hypothesis from the measurement of hits. The first measurement can be any hit in the barrel layers or in the F-disks. The second measurement is selected in any successive layer, provided that the axial angle between the first and second point, as seen from the beam spot (Figure 3.1), is smaller than $\Delta\phi = 0.08$. The third measurement may be in any further SMT layer given that the radius of curvature of a circle through the selected hits is greater than 30 cm (this corresponds to a $p_T > 180$ MeV). Additionally, the axial impact parameter, with respect to the beam spot, needs to be smaller than 2.5 cm and the χ^2 of the fit less than 16.

Each track hypothesis is extrapolated to the remaining silicon and fiber tracker layers. Hits are searched in an expectation window consistent with the track candidate and are associated with the hypothesis if the resulting χ^2 increases by less than 16 for each new hit. If more than one hit is accepted, the hypothesis is split and each result is considered separately.

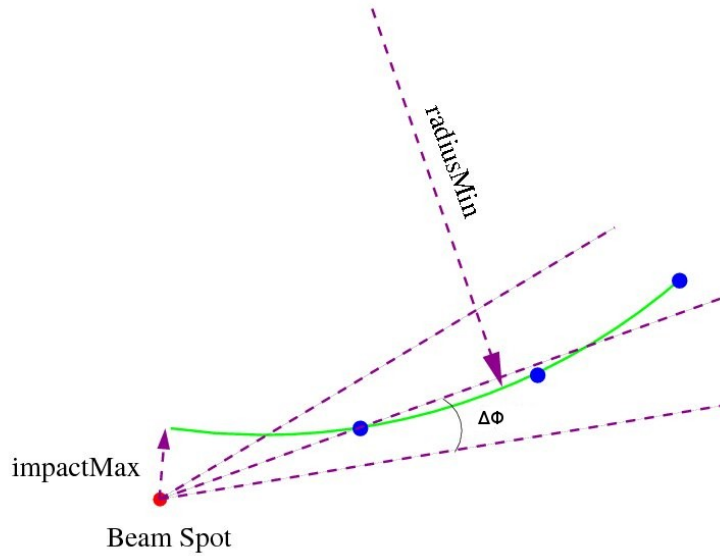


Figure 3.1: Schematic of the construction of track hypotheses in the AA method and its relevant parameters [5].

Missing hits (*misses*) are monitored taking into account adjustments for the presence of dead or disabled channels. Preliminary track selection depends heavily on the type of misses. They can be inside misses, which are those in between any two hits of a track hypothesis, and forward and backward misses, which are basically missed hits in the corresponding track extrapolation path.

There must be at least four hits in the detectors (SMT or CFT), in both axial and stereo layers. There may not be more than three inside misses, no more than six forward plus backward misses, and a maximum of two inside misses in the SMT are allowed. The number of hits should be at least five times as numerous as the misses. For track candidates with at least one inside miss, there may not be more than four (inside plus forward) misses and no more than three (inside plus backward) misses.

The hypotheses that pass these requirements are ordered observing first the number of hits (in decreasing order), then the number of misses (in increasing order), and finally the fit χ^2 of the track (in increasing order). A hypothesis is declared an AA-track if the following conditions are satisfied:

$$- N_{shared} \leq \frac{2}{3}N_{tot}$$

$$- N_{shared} \leq \frac{1}{5}N_{tot} \text{ or } N_{tot} - N_{shared} \geq 3$$

where N_{shared} is the number of shared¹ axial hits, and N_{tot} is the total number of axial hits.

In order to locate tracks with few or no hits in the SMT, AA is run a second time to search for hits in the CFT. The larger combinatorial background that arises in this case is reduced by considering only tracks that are consistent with a preliminary vertex identified in the first run of the AA.

3.1.2 The Histogramming Track Finder

This algorithm is based on the fact that the trajectory of a particle in a magnetic field can be characterized in the plane perpendicular to the direction of the field by three parameters: the radius of curvature, $\rho = qB/p_T$ (where q and p_T are the charge and transverse momentum of the particle, and B is the magnetic field); the impact parameter, d_0 ; and the azimuthal angle, ϕ . Cases we are interested in are those with small impact parameters $d_0 \approx 0$. The method relies on the so-called Hough transformation, which simply realizes that a family of possible trajectories (circles) crossing the (x, y) coordinates of a hit (in the SMT or CFT) of an unknown trajectory can be mapped into a single line in the parameter space (ρ, ϕ) . The parameters of the unknown trajectory will be associated to the intersection of such lines after all possible hits are taken into consideration. By quantizing the parameter space one gets a histogram with a clearly pronounced peak. Figure 3.2 illustrates the principles of the procedure.

After the histogram is created, it is processed through a two-dimensional Kalman filter [45] that attempts to remove tracks with large track errors as well as incorporate detector geometry and material density. In order to include the z -coordinate information and to further reduce the number of potential *fake* tracks, a new histogram is made, this time mapping the (r, z) coordinates to the parameter space (z_0, C) , where z_0 is the position of the track along the direction parallel to the beam line, and $C = dz/dr$ is the track inclination. Finally, depending on whether the algorithm initiated in the SMT or the CFT, the formed tracks are extrapolated outwards to the CFT or inwards to the SMT, respectively.

¹A track hypothesis *shares* a hit if it was used in an already selected AA-track.

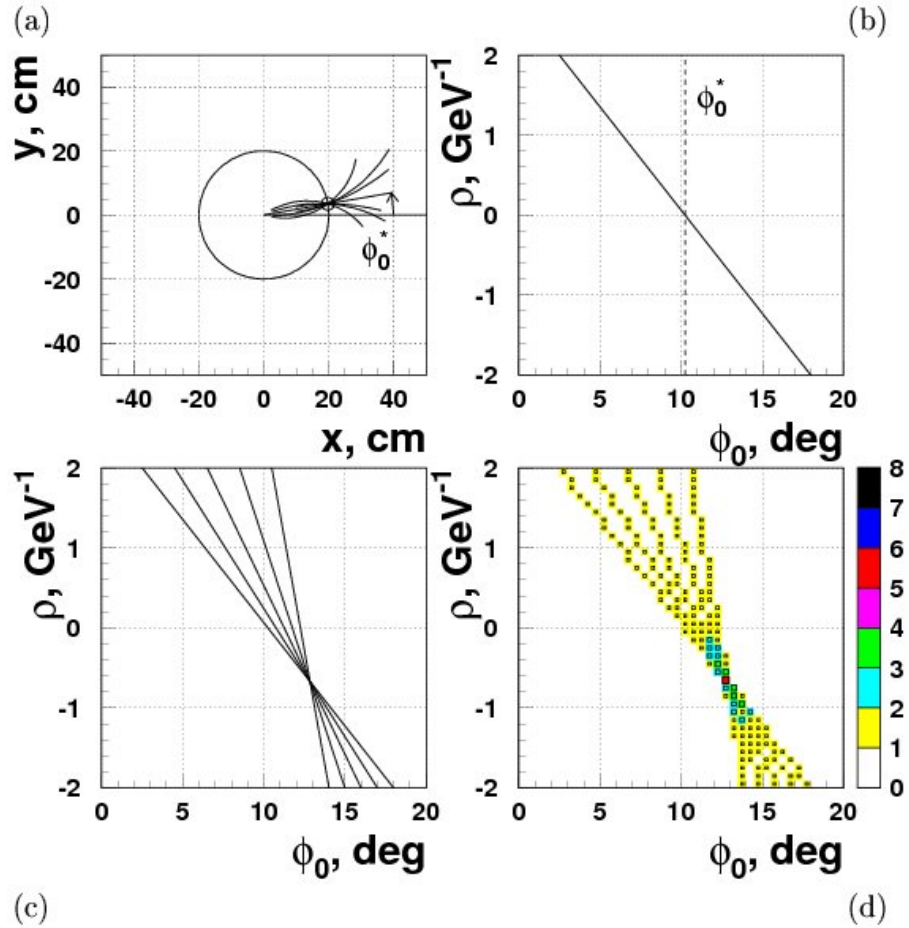


Figure 3.2: The histogramming technique shown for an example of a single 1.5 GeV muon track of 5 hits. (a) The family of trajectories containing a given hit. (b) The geometric place of all trajectories containing a given hit in parameter space. (c) Curves from different hits intersect at one point corresponding to the track parameters. (d) The point of intersection can be seen as a peak in the (ρ, ϕ) histogram. [6]

3.2 Vertex Reconstruction

The determination of the primary vertex, defined as the three-dimensional position of the hard scatter interaction, is a very important quantity since it is used for the calculation of the transverse energies in the calorimeter (Section 3.3), which have a direct impact on the reconstruction of the missing transverse energy (Section 3.6) in the event. The primary vertex reconstruction involves three basic steps: track selection, vertex fitting, and vertex

selection.

In the first step, tracks that were identified using the algorithms described in Section 3.1 are required to have a minimum p_T of 0.5 GeV and at least 2 SMT hits (if the track happens to belong to the SMT fiducial $\eta-z$ region). They are then clustered in the longitudinal plane to identify different interactions. Tracks that are 2 cm apart from each other are clustered together.

The second step is carried out in a two-pass approach for each of the track z -clusters. In the first pass, an estimation of the location and width of the beam is performed by fitting all the tracks in the z -cluster into a common vertex by means of a Kalman Filter vertex fitting algorithm. In the second pass, a pre-selection on the tracks corresponding to each z -cluster is performed based on their distance of closest approach to the beam spot. The resolution of the beam spot determination is properly taken into account. After the pre-selection, the Adaptive Vertex Fitting algorithm [46] is applied. This technique is an iterative Kalman Filter fitter that re-weights track errors based on their χ^2 contribution to the vertex by means of the Fermi-like function given in Eq. 3.1. There, χ_i^2 is the χ^2 contribution of the i th track to the primary vertex, χ_{cutoff}^2 is the distance where the function drops to 0.5, and T is a parameter controlling the sharpness of the function. The weight is re-computed always with respect to the new fitted vertex at each iteration, until convergence is achieved.

$$w_i = \frac{1}{1 + e^{(\chi_i^2 - \chi_{cutoff}^2)/2T}} \quad (3.1)$$

The third step consists of selecting and ordering, in a statistical fashion, the reconstructed primary vertices according to their increasing probability of coming from a Minimum Bias² (MB) interaction [47]. To accomplish this, reconstructed vertices that are within 2 cm from each other in the z -coordinate direction are clustered together, and only the highest multiplicity vertex is chosen from each cluster in order to remove split vertices. The MB probability for each of the reconstructed vertices is then calculated by using all the tracks within some defined distance around the vertex under analysis, and it is given by Eq. 3.2 where Π is the product of the individual probabilities of the N tracks associated to the vertex. The individual MB probabilities for the tracks are, in turn, given by Eq. 3.3, with

²MB interactions are those dominated by soft hadronic interactions, usually as part of the underlying event in a hard scatter collision.

$F(p_T)$ being the minimum bias track $\log_{10}(p_T)$ spectrum distribution determined from MC.

$$PMB = \prod \sum_{k=0}^{N-1} \frac{-\ln \Pi}{k!} \quad (3.2)$$

$$P(p_T) = \frac{\int_{\log_{10}(p_T)}^{\infty} F(p_T) dp_T}{\int_{\log_{10}(0.5)}^{\infty} F(p_T) dp_T} \quad (3.3)$$

The primary vertex with the lowest MB probability is picked as the hard scatter interaction vertex.

3.3 Electromagnetic Object Reconstruction

Most of the time, electromagnetic particles, i.e., electrons³ and photons, will predominantly deposit their energy in the EM part of the calorimeter through the initiation of EM cascades (*showers*), mainly due to the generation of bremsstrahlung processes, in case of electrons, or by e^+e^- production, in the case of photons.

The reconstruction of such particles starts with the clustering of EM towers [48]. The initial clustering is performed using the Simple Cone algorithm, which basically looks for EM towers with minimum transverse energy of 0.5 GeV and, if found, declare them as seeds. Calorimeter towers around these seeds are summed over within $\Delta R < 0.4$, in order to form calorimeter clusters. Each time a new tower is found within this cone the $\eta - \phi$ position of the cluster is recalculated. A simple cone cluster formed in this way is accepted if it has total $E_T > 1.5$ GeV and at least 90% of its energy belonging to the EM section of the calorimeter; otherwise, it is rejected.

A second cluster selection is performed by means of an isolation ratio computation. A list of towers within a large window (circle in $\eta - \phi$) of radius four calorimeter towers, about the highest E_T tower, is first created (Figure 3.3). From that list of towers, the total energy E_{tot} (EM + HAD), within a cone of $\Delta R < 0.4$ centered at the initial cluster position, is computed. Then, using the same list of towers, the EM energy around $\Delta R < 0.2$ from the initial cluster position, E_{core} , is calculated. If the isolation ratio $(E_{tot} - E_{core})/E_{core} < 0.2$, the cluster is isolated (Figure 3.4), meaning basically that there is a greater chance that

³Or, instinctively for this section's purpose, positrons.

the cluster is purely electromagnetic (electrons or photons) and not one formed by hadronic showers.⁴

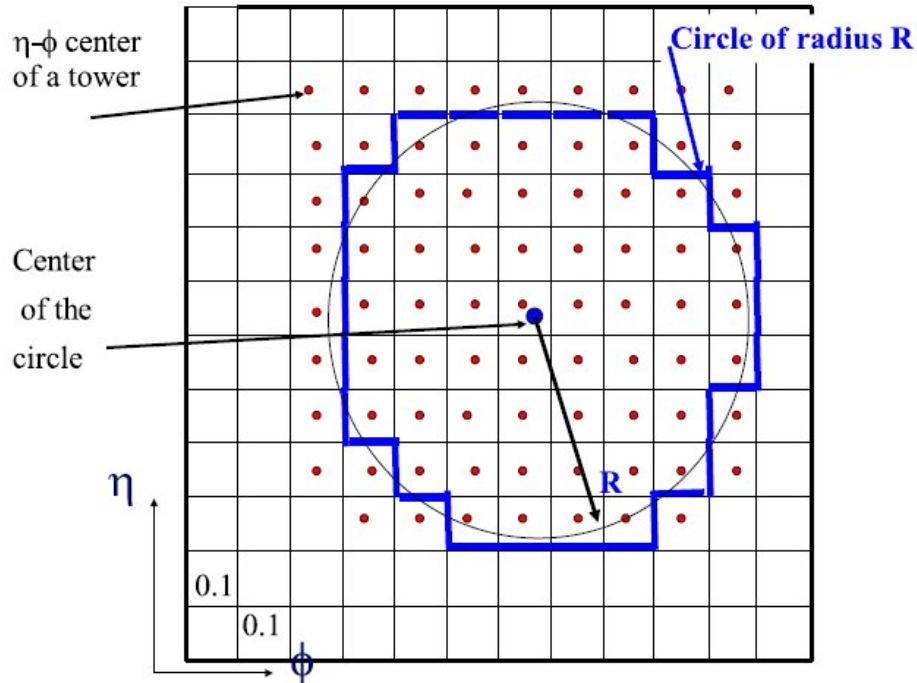


Figure 3.3: A circle of calorimeter towers in $\eta - \phi$ space. [7]

Electrons, as opposed to photons, are identified by associating (matching) a track, in the tracking detectors, to a reconstructed EM cluster. Low energy electrons, however, are generally not found by the clustering procedure. For this reason, there is an alternative algorithm [49] that is applied to reconstruct soft electrons. This method basically reverses the order of the standard reconstruction algorithm by looking first at tracks, finding preshower clusters for each track, and finally matching this information with calorimeter towers for each track. Additionally, the algorithm provides information gathered with the Road Method (RM) [50]. The method is used to reconstruct electrons in jets. The algorithm takes advantage of the fine granularity of the calorimeter and the tracking capabilities by

⁴In RunII b (See Chap. 4), the isolation energy (the numerator in the isolation expression), for a tighter selection level, is revised and slightly modified in order to properly take into account the effect of higher instantaneous luminosities.

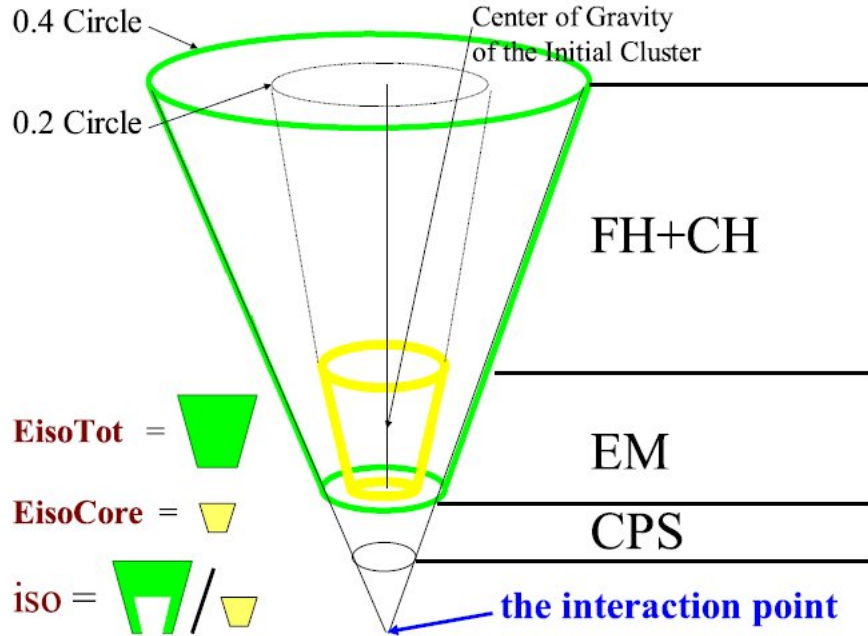


Figure 3.4: Schematic for the isolation in the simple cone algorithm. [7]

extrapolating reconstructed charged particle trajectories into the calorimeter.

The clustering algorithm matches candidates found by the algorithm in charge of finding soft electrons to the initial cluster candidates. If the initial cluster has an associated low-energy candidate, or if the cluster is isolated, the final selection is made and EM object candidates are stored, otherwise the cluster is rejected. Furthermore, the clustering algorithm uses, as final seeds, all low-energy candidates that were not matched to any initial cluster. In this case, an isolation procedure, similar to the one described above, is performed on a tower window of size 3×3 around the highest E_T tower of the candidate.

The next step performed is a very crucial one for this dissertation: CPS matching (see Chap. 4). After creating EM cluster candidates, the algorithm matches them to preshower clusters. The highest energy CPS cluster within a window of $\eta \times \phi = 0.1 \times 0.1$ about the EM object in the central region of the calorimeter is considered a match. A similar requirement holds for an FPS cluster matching an EM object in the end cap region. If the match is found, a flag is created, and the EM object's energy and position are adjusted in order to reflect the contribution from the preshower cluster.

The EM object is then matched to a track. If it has an associated low-energy object, then the charged particle associated with that low-energy candidate is adopted. If not, however, a central track is searched within $\eta \times \phi = 0.5 \times 0.5$ of the cluster. If found, the closest spatially matching track to the EM object is used, and the track information about η , ϕ , and vertex z position is used instead.

Additional information is computed for EM objects in order to help reduce multijet background (QCD background) and to discriminate between different EM object types (electrons or photons). The H-matrix quantity [51], for instance, is a shower shape χ^2 test based on correlated variables such as the fractional energy in each of the layers of the electromagnetic calorimeter, the total electromagnetic energy, the energy weighted transverse shower width in z and ϕ , and the z vertex distribution. Even though the H-matrix was originally designed to identify electrons, a looser requirement on it can be used to reject photon backgrounds. Electromagnetic showers, in general, have a lower χ^2 compared to other objects depositing energy in the calorimeter. In the analysis presented in this dissertation, the H-matrix and its input variables themselves are used to discriminate photons from different types of backgrounds (See Chap. 4).

An electron can be matched to a track by using two different χ^2 match probabilities. The first one is based on the position of the track with respect to the cluster in the calorimeter only (called spatial track match χ^2 probability), and the second one combines the spatial association with the ratio E_T/p_T , where E_T is determined by the calorimeter and p_T by the central track.

Furthermore, the probability of an EM object to have an associated track based on the density of hits in the CFT and SMT detectors that are consistent with one is also available [52]. This information proved to be of extreme importance for the study in this dissertation. In addition, the electron likelihood quantity is calculated to discriminate in favor of electrons or positrons based on the EM object's track, EM cluster, and the additional central tracks found very close to the candidate [53].

3.4 Muon Reconstruction

Muon reconstruction begins with the execution of the Linked List Algorithm [8], which builds muon segments out of hits in the muon wire chambers and in the scintillators. In order for this algorithm to work in all sections of the muon system (which have different geometrical

arrangements), it is necessary to perform a transformation of the hits' coordinates from the global system to their local system where drift circles⁵ are in the $x-y$ plane and wires extend along the z direction (wire planes are formed along the y axis).

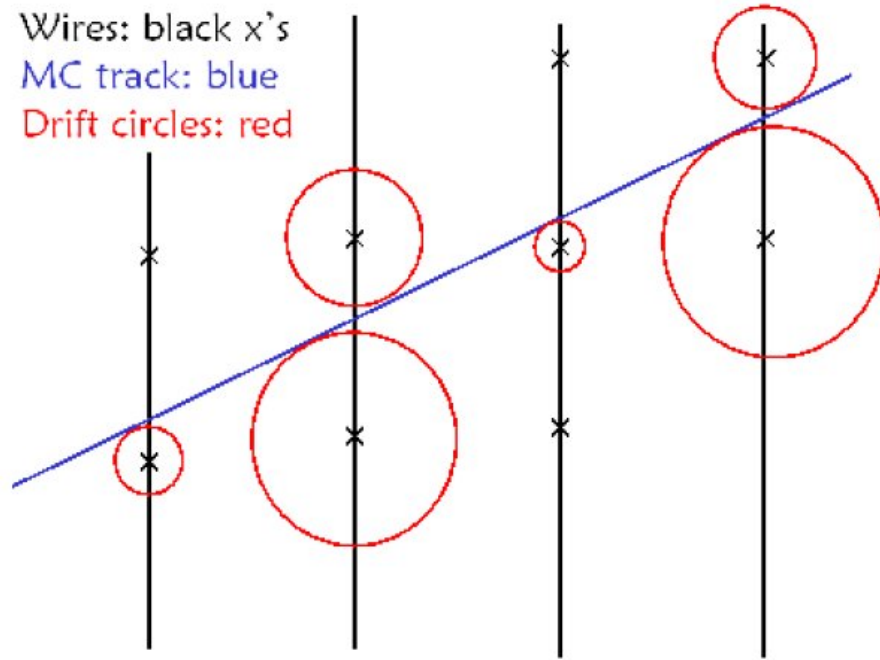


Figure 3.5: A local track segment in the muon system. Black vertical lines are the wire planes with the wires represented as “x”, running perpendicular to the plane of the picture. Drift circles are in red while the muon track is represented by a blue inclined line. [8].

After the coordinate transformation, the first step is to find local segments, which initially consist of two hits. Both hits are required not to belong to the same wire (drift circle) and to have a separation smaller than 20 cm in the y direction. Additionally, hits in the same plane are not considered to form a segment unless they are from the top and bottom of drift circles on neighboring wires. Inefficiencies in the wire chambers are taken into account by allowing the formation of local segments between hits which are not on neighboring planes. Local segments are then expanded to link additional local segments if they are compatible, resulting in new local segments with three or more hits. Figure 3.5 illustrates a sample track

⁵Effectively, a hit in a wire is a circle (or oval) with an equidrifttime circumference (Fig 3.5.)

segment.

After matching all possible local segments, they are fitted to a two-dimensional ($x - y$) line. The number of hits on the segment and the goodness of the fit, given by its χ^2 value, are used to choose the best four segments. The remaining segments are then associated with scintillator hits and re-fit. This is done in order to improve the timing information available and, in case of the forward system, refine the position determination.

These muon segments are then looped over and matched between those in the A-layer and those in the B- or C- layers. Local tracks (*local muons*) are finally created by fitting the best matches [54]. In addition, the presence of the toroidal magnet allows for local p_T measurements for muons with segments in both the A- and B- or C- layers.

Local muon tracks with a p_T measurement can be matched to a central track provided by the central tracking detectors (SMT and CFT) [55]. When a local muon is successfully matched with a central track it is called *central track-matched muon*. Central tracks can also be extrapolated to the muon system layers to find matches to track segments; this is useful for analyses requiring low momentum muons.

Muon reconstructed in this way are classified according to *type* and *quality*. A *type*, represented by a flag *nseg* in the algorithm implementation, is given to a muon depending on the number of muon segments (in the A-, B- or C- layers) used for its reconstruction and whether or not it was matched to a central track, as shown in Table 3.1.

Table 3.1: Muon types [2]

<i>nseg</i>	Type of segments	Central track matching
+3	A- and B- C- layers	central track to muon
+2	B- C- layers	central track to muon
+1	A-layers	central track to muon
0	muon hits used	central track to muon hit
-1	A-layer	no match
-2	B- C- layers	no match
-3	A- and B- C- layers	no match

The *quality* of a muon can be either *tight*, *medium*, or *loose*, depending on the *type* and the number of hits required in each of the layers involved. In this analysis, only muons with *loose* quality are of interest. *Loose* muons generally require $|nseg| = 3$ or, if $|nseg| < 3$,

$n_{seg} > 0$, plus some additional requirements on the number of wire hits and scintillator hits. Reference [56] gives a more detailed explanation of the different *quality* types.

To identify muons not coming from the interaction region, i.e., cosmic ray muons or halo muons, two selection flags are implemented in the reconstruction. First, a cosmic flag is activated if any of the scintillator hits are out of time, i.e., if the time given by the scintillators is not in agreement with that of the $p\bar{p}$ collision with more than 10 ns. An additional cosmic flag is activated if the muon has a matched track in the central tracking system, that track has a distance of closest approach larger than 0.2 cm, and it is out of time with the scintillator hits.

3.5 Jet Reconstruction

Quarks and gluons (parton level) produced in hadron-hadron high energy collisions fragment (or hadronize) into mesons and baryons (particle level). These energetic sprays of particles are known as jets and their reconstruction, out of detector measured quantities (detector level), is a challenging task. The aim of algorithms used for reconstruction is to associate the kinematic properties of these jets to the properties of the energetic partons produced in the hard scattering process.

A good jet reconstruction algorithm needs to follow certain recommendations in order to be robust [57]. These considerations include infrared and collinear safety, i.e., the results should be insensitive to the emission of soft partons or the splitting of energy between collinear particles. The algorithm should be also as independent to as possible of detector characteristics, should be invariant under longitudinal boosts along the beam axis, and must be computationally viable.

The DØ experiment uses the Improved Legacy Cone Algorithm (ILCA), also known as the Midpoint Cone Algorithm [58]. In order to build a composite object, this algorithm can associate and combine different types of items such as simulated partons or particles, or calorimeter cells or towers in data. The present discussion puts more emphasis on the reconstruction at the detector level, though the applicability extends to any of the aforementioned items. These items are always combined using the *E-scheme*, i.e., by adding

their 4-momentum:

$$p^J = (E^J, \mathbf{p}^J) = \sum_i (E^i, p_x^i, p_y^i, p_z^i). \quad (3.4)$$

From Eq. 3.4, all kinematic quantities can be derived: the transverse momentum $p_T^J = \sqrt{(p_x^J)^2 + (p_y^J)^2}$, the azimuthal angle $\phi^J = \tan^{-1}(p_y^J/p_x^J)$, and the rapidity $Y^J = \frac{1}{2} \ln(\frac{E^J + p_z^J}{E^J - p_z^J})$.

The process starts with the reconstruction of towers from calorimeter cells. Only those cells with energy greater than 2.5 times the width of their pedestal distributions σ_{cell} are taken into account. Noisy cells are removed by a dedicated algorithm [59]. Negative energy cells and cells with an energy less than $4\sigma_{cell}$ that have no neighbors with measured energies above $4\sigma_{cell}$ are also removed [60]. The 4-momentum of a tower is calculated using the E -scheme.

The Simple Cone Algorithm [57] is used to build jet preclusters out of a list of towers. The algorithm loops over this list looking for seeds with $p_T > 0.5$ GeV, and sorts them in decreasing order of p_T . The first item in the list is chosen as precluster seed P and removed from the list. Then, a new loop is carried out over the remaining items J in the list. If the solid angle⁶ $\Delta R(P, J)$ is smaller than 0.3 and $p_T^J > 1$ MeV, J is added to the precluster P . After all preclusters are formed, those with $p_T^P > 1$ GeV are used as seed for proto-jet generation. Single-tower preclusters are also discarded.

Proto-jets are the product of a clustering routine based on the list of preclusters provided by the Simple Cone Algorithm and the list of items (e.g. calorimeter towers). The procedure is an iterative one and consists of selecting a position and adding all items within a cone in ΔR of a certain size around that position. DØ reconstruction software uses two specific sizes, 0.7 for JCCA jets and 0.5 for JCCB jets. The list of preclusters, ordered in decreasing order of p_T , supplies the seeds for proto-jet candidate (PC) construction. A precluster in this list seeds a proto-jet candidate (PC) if it is separated from the closest existing proto-jet by a ΔR at least half of the jet cone size; otherwise it is discarded from the seeds list. During the iteration, all items inside the cone around PC are combined following the E -scheme to form a new proto-jet candidate PC' . PC is replaced by PC' at each iteration until $p_T^{PC'} < 3$ GeV (in which case the proto-jet is discarded) or the precluster candidate is stable, i.e., $\Delta R(PC', PC) < 0.001$. If the iterations reach number 50, the process is also

⁶The definition of the solid angle is similar to the one in Eq. 2.3 in Chap. 2 in the $(Y - \phi)$ space.

stopped. The algorithm then uses the next precluster in the list to try to construct a new proto-jet candidate until the available preclusters are exhausted.

In order to avoid sensitivity to soft radiation, ILCA uses midpoints between proto-jets as an additional set of seeds. A clustering procedure similar to the one described above is performed once again with no restriction on the proximity to existing proto-jets and no checks for duplicates. The final list of proto-jets from preclusters and midpoints is used in the last step: merging and splitting. This procedure is simply a way of dealing with overlapping proto-jets. It is based on the percentage of transverse energy shared by the lower p_T proto-jet. Proto-jets sharing a fraction greater than 50% are merged, the rest are split. When splitting takes place, the shared towers are individually assigned to the proto-jet that is closest in $(Y - \phi)$ space. Jets candidates formed in this way are stored together with some information, like their position or p_T , which is needed for higher level physics analysis.

3.6 Missing Energy Reconstruction

The missing transverse energy (\cancel{E}_T) is a very important quantity for the analysis presented in this dissertation. Since \cancel{E}_T is the signature of non-interacting particles in the detector (such as neutrinos or gravitons, for instance), its accurate measurement is vital to identify potential unknown new particles that would lead to the discovery of new physics. This is so because the total transverse momentum at the interaction point is approximately zero, which implies no net transverse momentum for the particles produced in an interaction. Thus, the magnitude of the vector sum of the x - and y -components of the measured energy in an event with no neutrinos must be zero within the resolution effects of the various detector components.

Missing E_T is nothing but the visible transverse energy in the calorimeter multiplied by a factor of (-1) [61]. In principle, all detector components and all reconstructed objects can contribute to \cancel{E}_T , therefore, its determination is the last task performed at the reconstruction level.

One can define the x - and y -components of the visible energy in the calorimeter following Eq. 3.5, where advantage is taken of the calorimeter granularity by using the cells for \cancel{E}_T reconstruction. The calorimeter missing energy projections are then given by Eq. 3.6 and Eq. 3.7. Thus, the missing transverse energy in the calorimeter can be defined as in

Eq. 3.8. A similar approach can followed by using towers instead of cells.

$$E_{x,y}^{vis} = \sum_{cells} E_i^{x,y}, \quad (3.5)$$

$$\cancel{E}_x = -E_x^{vis}, \quad (3.6)$$

$$\cancel{E}_y = -E_y^{vis}, \quad (3.7)$$

$$\cancel{E}_T = \sqrt{\cancel{E}_x^2 + \cancel{E}_y^2}. \quad (3.8)$$

There are different definitions of \cancel{E}_T in the reconstruction algorithm, depending on whether thresholds on cell or tower energy and η limits are applied [62]. The \cancel{E}_T and calorimeter E_T are corrected for the presence of reconstructed muons in the event, noisy cells from the CH section of the calorimeter, jets and corrections to their energy scale, and that of electromagnetic particles.

Additionally, *rings* in η_{det} are calculated with respect to the primary vertex. The ring information is given by x - and y -components for the electromagnetic and hadronic summed E_T , in each of the η_{det} bins. Rings are useful when analyses require a recalculation of \cancel{E}_T when the primary vertex has been reassigned [63].

CHAPTER 4

ANALYSIS

The analysis in this dissertation aims at testing for the presence of sub-millimeter LED in our universe. We do this by studying the process $q\bar{q} \rightarrow \gamma + G_{KK}$ (Fig 4.1) where a single photon and a Kaluza-Klein graviton are present in the final state. This chapter gives information about the datasets (Section 4.1.1) used for the study. It also explains the selection procedure for a sample that is later used to look for these exotic events.

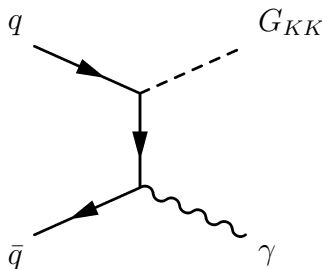


Figure 4.1: Feynman diagram for the process $q\bar{q} \rightarrow \gamma + G_{KK}$. Direct graviton production in the $\gamma + \cancel{E}_T$ channel.

As already mentioned in Section 1.4, the collider signature for a KK graviton that escapes to a hypothetical large extra volume is the loss of transverse energy. Thus, we expect the LED signal to be $q\bar{q} \rightarrow \gamma + \cancel{E}_T$. The apparent simplicity of the detection of these final states is diminished by the presence of different processes that have the same collider signature and that are difficult to reject. In Section 4.1.2, we state the kind of signal signature we are looking for and identify different sources of background. In that section, we also describe the procedure that was followed for MC simulations of the signal and some of the backgrounds

processes. In Section 4.1.3, we describe a fundamental tool that is used in this analysis: the EM pointing algorithm. This tool is crucial for the selection of single photons (Section 4.1.4) and background estimation (Section 4.2).

In the analysis presented in Ref. [64] we searched and found no evidence for the presence of large extra dimensions. We set limits on M_D at the 95% C.L. from 884 GeV to 778 GeV for two to eight extra dimensions. These published results, with approximately 1 fb^{-1} of data, constitute a great improvement over an existing similar study performed by the CDF collaboration during the early years of the Tevatron scientific program. This dissertation explains such an analysis in more detail. The CDF collaboration has recently carried out a similar search with 2 fb^{-1} of data, setting 95% C.L. lower limits on M_D from 1080 GeV to 900 GeV for two to six extra dimensions [10]. We have upgraded our published analysis to incorporate an additional 1.7 fb^{-1} of data. These preliminary results are also presented in this dissertation.

Searches for LED in other final states have been performed by collaborations at the Tevatron [65, 66, 67, 68] and the CERN LEP collider [11].

At the end, in Chap. 5, we use the results presented in this chapter in order to formulate an assertion about the hypothesis of the presence of LED in our universe.

4.1 Event Selection

There is a simple idea behind event selection for this analysis. Out of millions of events recorded by $D\bar{O}$ experiment, we need to select those that consist of a single energetic photon and nothing else. Analogously to the case of β -decay where physicists predicted the presence of the neutrino to explain the apparent non-conservation of energy, an excess of events in this final state could imply either the existence of an invisible particle or momentum non-conservation. We use this pool of candidate events to test the LED hypothesis.

The background to the $\gamma + \cancel{E}_T$ signal is dominated by electroweak boson production and *non-collision* background where muons from the beam halo or cosmic rays undergo bremsstrahlung and produce an energetic photon. The electroweak background is dominated by the processes $Z + \gamma \rightarrow \nu\bar{\nu} + \gamma$, $W \rightarrow e\nu$ where the electron is misidentified as a photon, $W + \gamma$ where the lepton from the W boson decay is not detected, and $W/Z + \text{jet}$ production where the jet is misidentified as a photon.

4.1.1 Datasets and Triggers

This analysis uses data recorded by the DØ detector between October 2002 and May 2008. In general, this period of time is known as *Run II*, since it corresponds to the second phase of the experimental program at the Tevatron Collider. An upgrade to the DØ detector was performed during a long shut-down of the Tevatron in 2006. As a result, two different datasets were created, *Run IIa* and *Run IIb*, corresponding to data accumulated before and after the shutdown, respectively. The upgrade to the DØ detector was primarily done to support the impact of higher instantaneous luminosities after the shut-down. This imposes physical and technical differences between the two datasets that forces the application of different selection requirements, although most of them remain the same. We explicitly note the differences in the selection criteria when considered necessary, otherwise it will be assumed that there is no difference between the two epochs. The strategy in this search is to study these datasets separately and combine them later with a method that observes possible correlations between them.

In both datasets we only use triggers that guarantee events with at least one energy cluster in the EM section of the calorimeter with $E_T > 20$ GeV. These triggers are 100% efficient for selecting EM objects with $E_T > 50$ GeV [69]. Tables 4.1 and 4.2 list the trigger definitions¹ that were used. Tables 4.3 and 4.4 summarize the data accumulated with these triggers and give their size in terms of integrated luminosity.

Additionally, we perform a standard quality check of the data used. This quality filter is provided by the DØ Data Quality Group and removes events that may have been recorded by sub-detector parts with hardware problems. It also removes duplicated events that may have been introduced during the data collection chain.

¹For a brief explanation of trigger definitions see Section 2.3.6. A more detail explanation of the nomenclature is given in Ref. [70].

Table 4.1: Run IIa trigger list.

Trigger list version	Trigger definitions
v8-v11	EM_HI_SH EM_HI_2EM5_SH EM_MX_SH EM_HI
v12	E1_SHT20 E2_SHT20 E3_SHT20 E1_SH30
v13	E1_SHT22 E2_SHT22 E3_SHT22 E1_SH30
v14	E1_ISH30 E1_ISHT22 E1_SH35 E1_SHT25 E3_ISH30 E3_ISHT22 E3_SH35 E3_SHT25

Table 4.2: Run IIb trigger list.

Trigger list version	Trigger definitions
v15-v15.5	E1_SHT25 E1_SH35 E1_L70 E2_SHT25 E2_SH35 E2_L70 E1_ISHT22 E1_ISH30 E2_ISHT22 E2_ISH30
v15.5-v16	E1_LH2SH27 E1_LH2L70 E1_SHT50 E1_SH60 E1_L80 E2_LH2SH27 E2_LH2L70 E2_SHT50 E2_SH60 E2_L80 E1_LH2ISH24 E2_LH2ISH24
v16	E1_SHT27 E1_LH3SH27 E1_SHT27_NOLUM E1_LH3ISH25 E2_LH3ISH25

Table 4.3: Data summary for Run IIa.

Trigger version	Time epoch	Run range	Integrated Luminosity pb ⁻¹
v8 - v11	11/21/02 – 07/07/03	166503 – 178721	100 ± 6
v12	05/26/03 – 06/28/04	177311 – 194566	231 ± 14
v13	06/28/04 – 07/13/05	194567 – 208122	379 ± 23
v14	07/05/05 – 02/22/06	207217 – 215670	334 ± 20
Total	11/21/02 – 02/22/06	166503 – 215670	1044 ± 63

Table 4.4: Data summary for Run IIb.

Trigger version	Time epoch	Run range	Integrated Luminosity pb ⁻¹
v15 - v15.3	09/05/06 – 01/31/07	222865 – 230124	533 ± 33
v15.5 - v15.96	01/31/07 – 03/13/08	230126 – 240743	1079 ± 66
v16	02/28/08 – 05/06/08	240390 – 241889	88 ± 5
Total	09/05/06 – 05/06/08	222865 – 241889	1700 ± 104

4.1.2 Signal, Background Sources, and MC Simulations

It is necessary to have a clear idea of the kind of events we are searching for and the backgrounds we expect. For our signal, we simulate the production of one photon and a KK graviton using a version of the PYTHIA [71] program that was modified to incorporate this process. Graviton plus jet production is included in PYTHIA version 6.413 where the cross-sections are calculated following Eq. 1.13. The relevant differential cross-sections used for the parton processes are analogous to Eq. 1.11 and can be found in Ref. [27]. In fact, a simple modification by one of the PYTHIA authors [72] was enough to accommodate our desired process ($q\bar{q} \rightarrow \gamma + G_{KK}$) into the program.

As can be noted from Eq. 1.11 and Eq. 1.13, the kinematical spectra remains unaffected if the number of extra dimensions is fixed. Therefore, we generate signal events for this number of extra dimensions from two to eight using a fixed value of $M_D = 1500$ GeV, with minimum parton transverse momentum (\hat{p}_T) of 50 GeV, in the full geometrical acceptance. In order to get the cross-sections for different values of M_D , we simply scale the cross-sections by $1/M_D^{n+2}$. We then multiply these cross-sections by 0.30, which is the fraction of hard-

collision events that have a photon with simulated (generated level) transverse momentum (p_T^{gen}) greater than 90 GeV in the central region ($|\eta| < 1.1$). Figure 4.2 shows the cross-sections as function of M_D for this particular acceptance configuration.

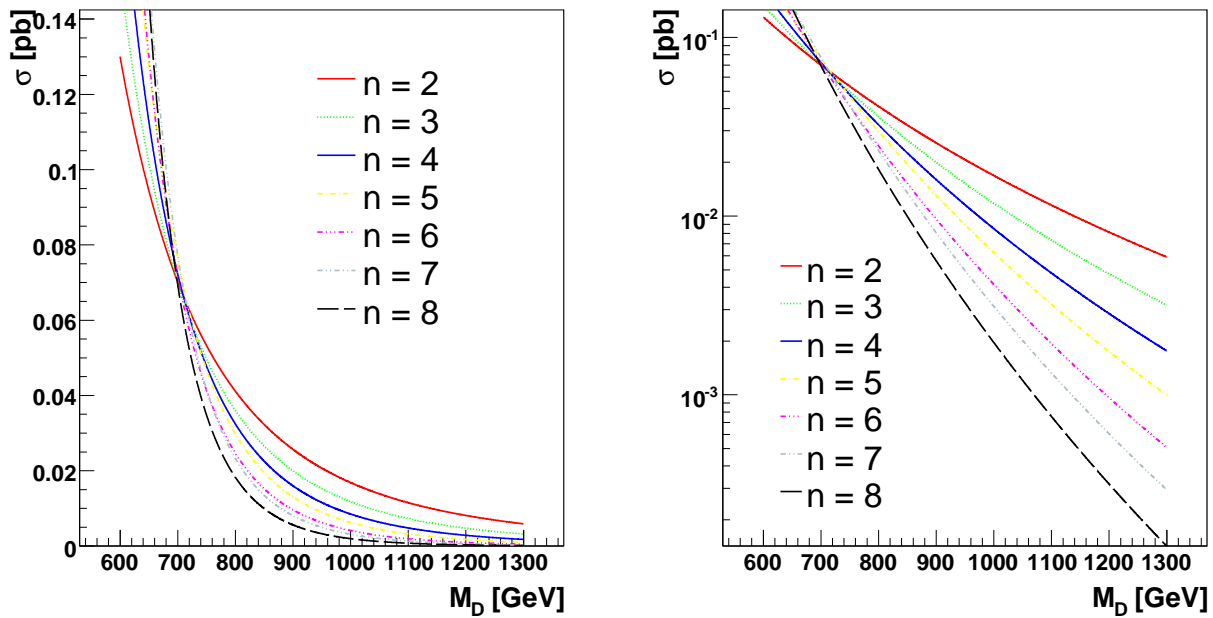


Figure 4.2: LED cross-sections for central single photons with $p_T^{gen} > 90$ GeV as function of M_D . Plots with linear (left) and semi-logarithmic (right) scales are shown.

It is useful, at this point, to identify the main sources of background to the $\gamma + \cancel{E}_T$ signal. They are:

- **Non-collision events**, background from beam halo muons or cosmic rays that undergo bremsstrahlung and produce an energetic photon in the calorimeter.
- **$Z + \gamma \rightarrow \nu\bar{\nu} + \gamma$ production**, which gives the same signature as the LED signal because the neutrinos will manifest as missing energy in the detector. Figure 4.3 shows the Feynman diagrams for this process.
- **$W \rightarrow e\nu$ production**, where the electron is misidentified as a photon due to inefficiency in the tracker. Figure 4.4 shows the Feynman diagram for this process.

- **$W + \gamma$ production**, where the charged lepton in a leptonic W decay is not reconstructed. Figure 4.5 shows the Feynman diagrams for this background.
- **$W/Z + \text{jet}$ production**, where the jet is misidentified as a photon. Figure 4.6 shows an example of a Feynman diagram for this background.

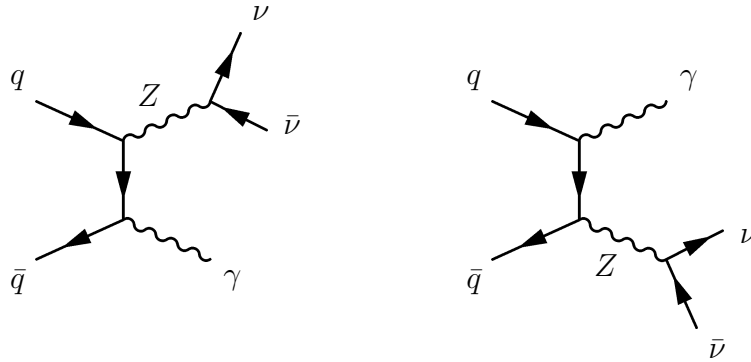


Figure 4.3: Feynman diagrams for the process $q\bar{q} \rightarrow Z + \gamma$.

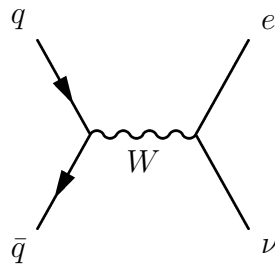


Figure 4.4: Feynman diagram for the background process $W \rightarrow e\nu$. The electron (positron) is misidentified as a photon due to inefficiency in the tracker.

Non-collision background is the most copious in this analysis. Later in this chapter it will be seen how we efficiently identify and reduce it, leaving $Z + \gamma \rightarrow \nu\bar{\nu} + \gamma$ production as the main background contributor. We use data events to estimate non-collision, $W \rightarrow e\nu$,

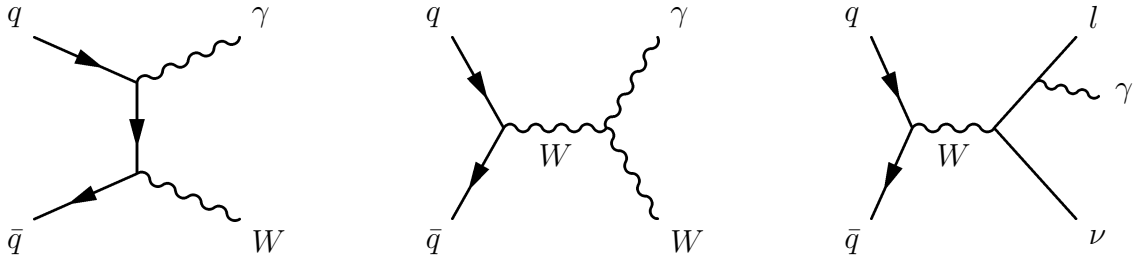


Figure 4.5: From left to right: Feynman diagrams representing the initial state radiation (IRS), trilinear gauge coupling (TGC), and final state radiation (FSR) contributions to the background process $W + \gamma$. The lepton from the leptonic decay of the W is not reconstructed.

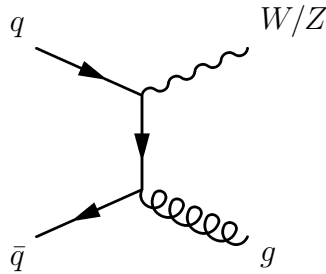


Figure 4.6: Example of a Feynman diagram for the background process $W/Z + \text{jets}$. The jet is misidentified as a photon.

and $W/Z + \text{jet}$ backgrounds, whereas $W + \gamma$ production and $Z + \gamma \rightarrow \nu\bar{\nu} + \gamma$ production are estimated from MC simulated samples. There is the possibility of an additional contribution to the background coming from multijet events (also known as QCD events). However, this background is shown to be negligible for this study. Background estimation will be studied later in Section 4.2.0.9.

The $W + \gamma$ MC sample corresponding to Run IIa is obtained from the official DØ Monte Carlo $W(+\text{jets}) \rightarrow \text{lepton} + \bar{\nu}(+\text{jets})$ samples, which is generated using PYTHIA version 6.3. The request identification numbers for the samples used are:

- $W(+\text{jets}) \rightarrow e + \nu(+\text{jets})$: 37639, 37640, 38851, 38853-38855, 38857-38861, 42214-

42218.

- $W(+\text{jets}) \rightarrow \mu + \nu(+\text{jets})$: 35033, 35034, 38929-38938, 42219-42223.
- $W(+\text{jets}) \rightarrow \tau + \nu(+\text{jets})$: 37646, 37648, 39231-39245, 41476-41485, 43254-43263.

We extract about 100 thousand $W + \gamma$ events at generator level, separating the final state radiation (FSR) from the initial state radiation component (ISR) in the resulting sub-sample. We do this in order to use the cross-sections calculated with the MC generator based on Ref. [73], which includes the trilinear gauge boson vertex (see Figure 4.5) contribution. The CTEQ6L1 parton distribution functions (PDF) are used in the cross-section calculation [74]. Additionally, we are careful not to include misidentified jets in the estimation by requiring the generated photon to spatially match the reconstructed one within a fixed cone of radius $\Delta R < 0.03$ (see Figure ?? in App. ??). Misidentified jets are estimated from data as described in Section 4.2.

For Run IIb epoch, however, the $W\gamma$ background is estimated using the official DØ Monte Carlo $W(+\text{gamma}) \rightarrow \text{lepton} + \bar{\nu}(+\text{gamma})$ samples (also generated with PYTHIA program version 6.3). The request identification numbers for the samples used are:

- $W(+\text{gamma}) \rightarrow e + \nu(+\text{gamma})$: 88458, 88459
- $W(+\text{gamma}) \rightarrow \mu + \nu(+\text{gamma})$: 88460, 88461
- $W(+\text{gamma}) \rightarrow \tau + \nu(+\text{gamma})$: 88462, 88463

These events are generated with minimum parton $p_T = 8$ GeV within the full geometrical coverage. The cross section is taken directly from the generator program.

For Run IIa, nearly 15000 $Z\gamma \rightarrow \nu\bar{\nu}\gamma$ events are simulated using PYTHIA version 6.3 using CTEQ6L1 PDFs. Likewise, for Run IIb, we generate 26000 of these events.

The uncertainty in the theoretical cross sections of the simulated SM background processes is dominated by the uncertainty in the next-to-leading-order K factors (7%). For the range of p_T in question and for the selection requirements used in this analysis (particularly the rejection of jets with $p_T > 15$ GeV; see Section 4.1.4) the K factors vary around unity within this uncertainty margin [73, 9], as can be seen in Figure 4.7 for the $Z + \gamma$ contribution.

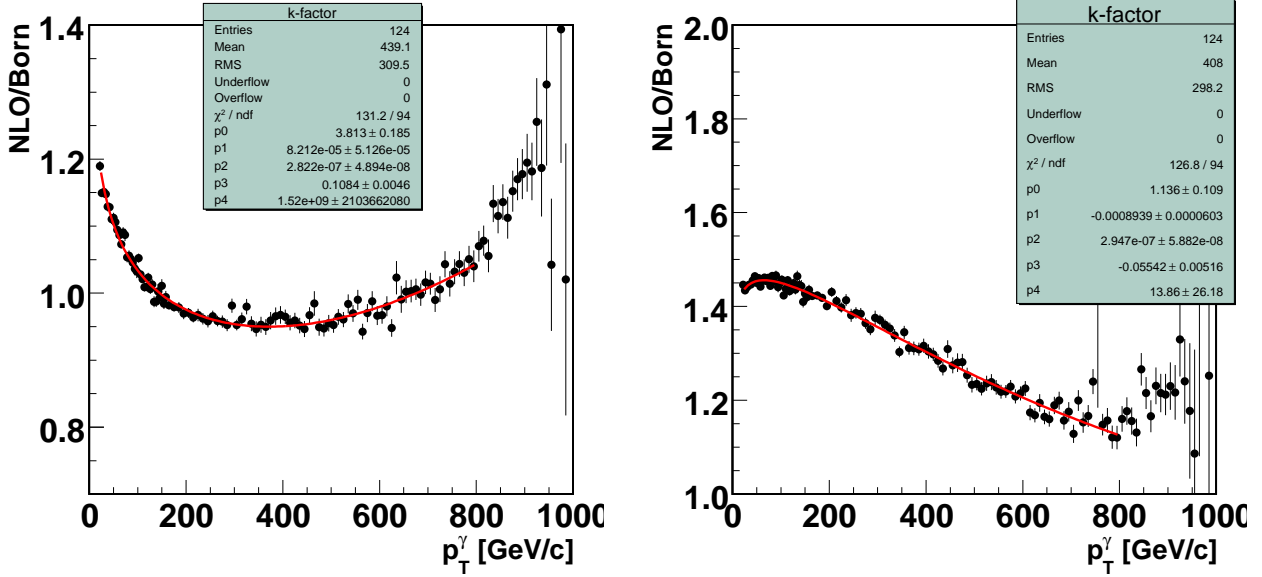


Figure 4.7: K-factor as a function of photon p_T with $p_T^{jet} > 15$ GeV veto (left) and with no veto on jets (right) [9].

All MC events are generated with the appropriate minimum-bias overlay, since the profiles are different for Run IIa and Run IIb datasets. Therefore, MC simulations are also classified in Run IIa and Run IIb epochs. They are passed through a detector simulation based on the GEANT [75] package, and processed using the same reconstruction software as for the data.

4.1.3 The EM Pointing Algorithm

Non-collision events, i.e., events that do not originate from the interaction region in the detector, may deposit energy in the electromagnetic part of the calorimeter, leaving a signature that can mimic the presence of new physics. For instance, muons from cosmic rays or from beam halo can undergo bremsstrahlung and produce an energetic photon. Most of these events are rejected by means of timing constraints in the detector, although a considerable number of them still remain. The inherent energy-unbalanced configuration of these events produces large \cancel{E}_T that is comparable to the p_T of the alien photon, making a perfect fake for the LED signal.

Figure 4.8 shows several views of the detector display of a *clean* signal event with a single photon. It is illustrative to compare the different projection views of this display with the

ones corresponding to a cosmic event (Figure 4.9), or a beam halo event (Figure 4.10). Note in the cosmic event, for example, how a cosmic ray muon enters the detector via its upper left part (see the $z - y$ view), deposits energy in the calorimeter, and traverses the entire detector to finally leave a muon segment at the bottom right part of the detector. At first sight, these three types of events leave identical signatures in the calorimeter, as can be seen in the $x - y$ views of the display figures.

Since, in practice, there is only one physical object in a LED event candidate (the photon), the options are very limited when it comes to trying to reject non-collision backgrounds. This is where the EM pointing algorithm comes in handy, as it will prove to be a fundamental tool to identify and discard non-collision background. The EM pointing algorithm calculates the point of origin and direction of an EM shower based purely on the information in the electromagnetic section of the calorimeter and the central preshower system. This is possible only because of the fine longitudinal and transverse segmentation in all four layers of the EM calorimeter.

The algorithm first calculates the energy weighted *center-of-gravity* of the spatial position of the electromagnetic shower in the four layers of the EM section of the calorimeter. Then, it performs a straight line fit using these four position coordinates and the position of the CPS energy cluster. The coordinates of the energy-weighted position at each layer F ($= 1, 2, 3, 4$) in the EM section of the calorimeter are calculated as [76]:

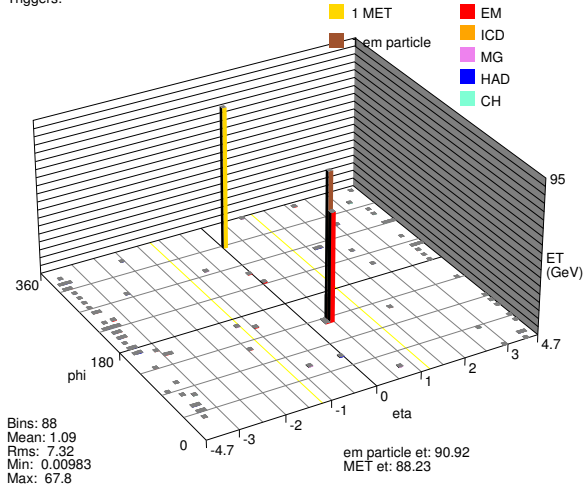
$$\begin{aligned}
 x^{layerF} &= \sum_{layerF}^{cells} w_{cell}^{layerF} x_{cell} / \sum_{cells}^{layerF} w_{cell}^{layerF}, \\
 y^{layerF} &= \sum_{cells}^{layerF} w_{cell}^{layerF} y_{cell} / \sum_{cells}^{layerF} w_{cell}^{layerF}, \\
 z^{layerF} &= \sum_{cells}^{layerF} w_{cell}^{layerF} z_{cell} / \sum_{cells}^{layerF} w_{cell}^{layerF}.
 \end{aligned} \tag{4.1}$$

In Eq. 4.1, x_{cell} , y_{cell} , and z_{cell} are the position coordinates of the individual cells in the EM calorimeter, and w_{cell}^{layerF} is the weight that a layer cell receives based on its relative (logarithmic) contribution to the total energy deposition of the EM shower in that particular calorimeter layer [76]:

$$w_{cell}^{layerF} = \max\{0, [w_0 + \ln(E_{cell}^{layerF} / E_{total}^{layerF})]\}, \tag{4.2}$$

Run 214635 Evt 23177986

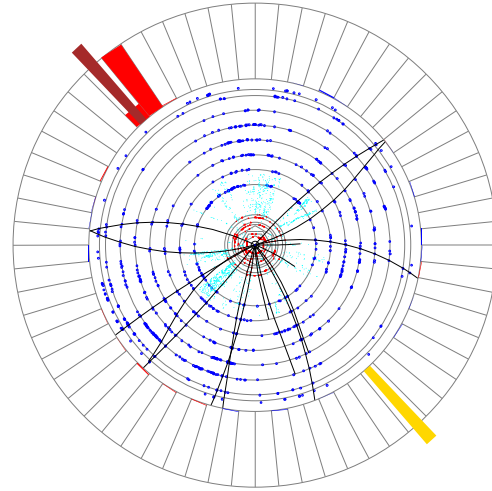
Triggers:



(a) $\eta - \phi$ lego plot

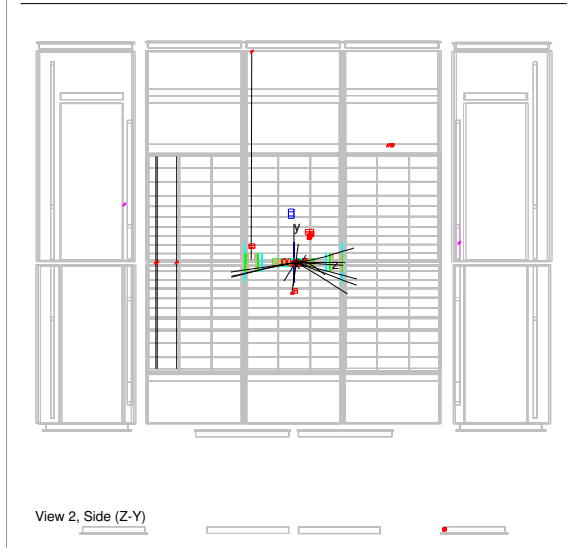
Run 214635 Evt 23177986

ET scale: 69 GeV



(b) $x - y$ view

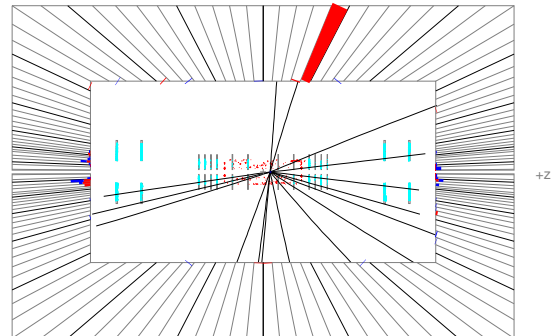
Run 214635 Evt 23177986



(c) $z - y$ view

Run 214635 Evt 23177986

E scale: 83 GeV



(d) $r - z$ view tracker and calorimeter

Figure 4.8: Detector display of a single photon event. In (a), the presence of an EM object is depicted in red, while missing transverse energy (MET) is shown in yellow. In (b) and (d), tracks can be seen, together with the energy deposition in the calorimeter. (c) shows very little activity (red and blue segments) in the muon spectrometer.

where $E_{cell}^{layer F}$ is the energy of a cell at layer F , $E_{total}^{layer F}$ is the energy of all cells in the EM shower at layer F , and w_0 is a cutoff weight. If the result of Eq. 4.2 is negative, due to the

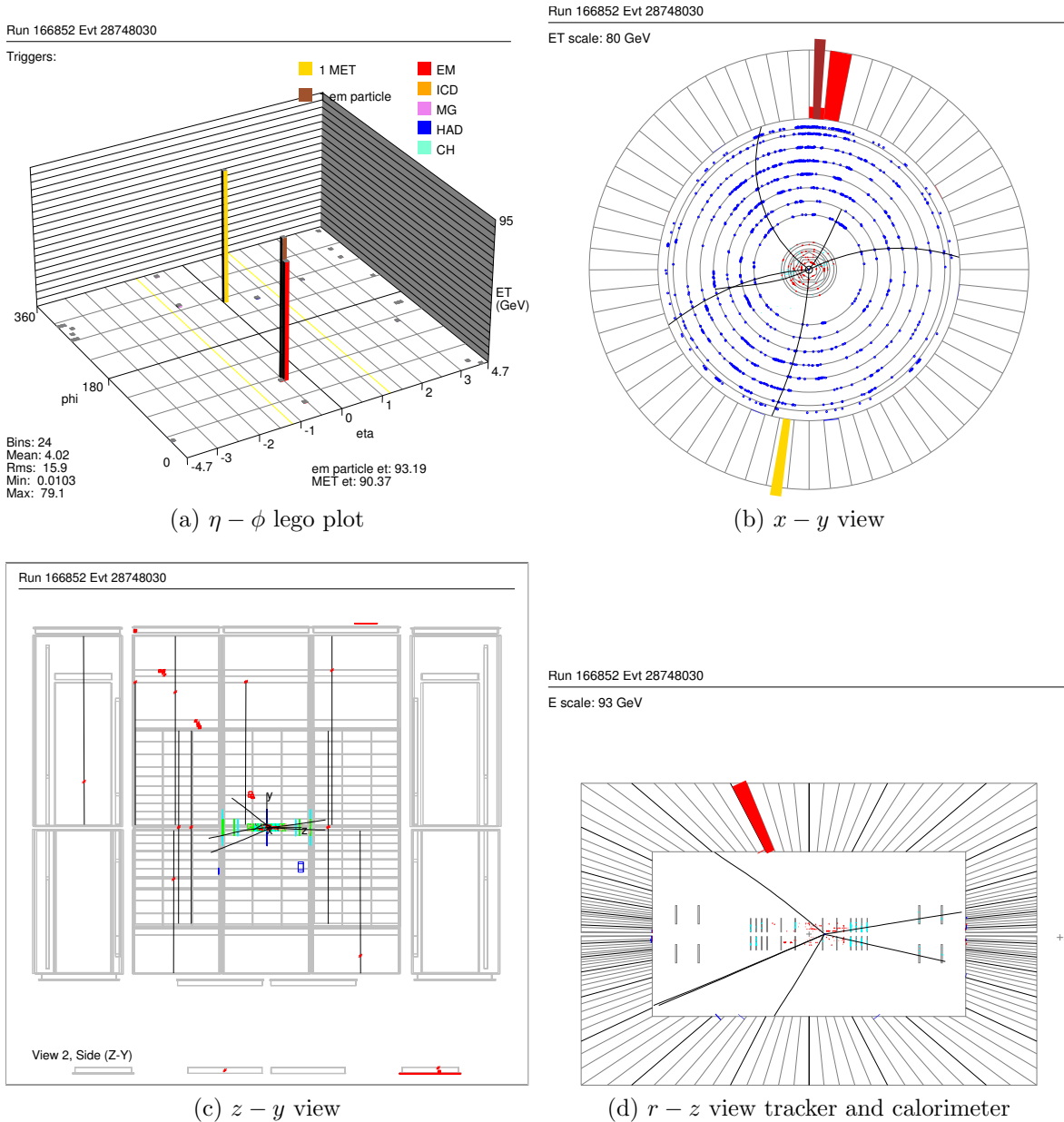


Figure 4.9: Detector display of a cosmic ray event with identical signature as for a signal single photon event. A cosmic ray muon enters the detector from the upper part, deposits energy in the calorimeter, and leaves at the bottom.

presence of unphysical negative energies engendered by the calorimeter readout, the weight is set to zero.

The positions given by Eq. 4.1 are then corrected by using Monte Carlo simulated samples

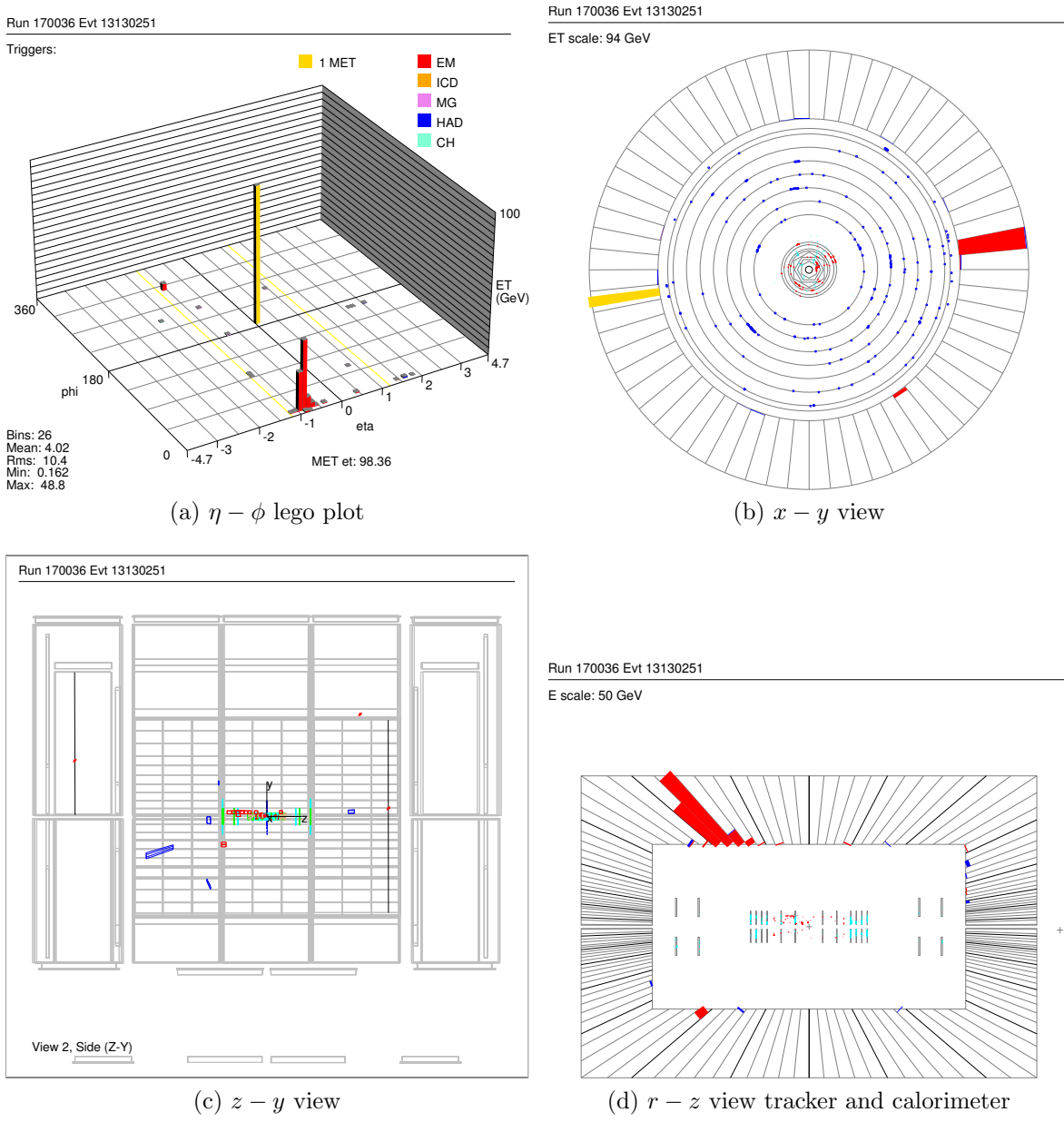


Figure 4.10: Detector display of a beam halo event with identical signature as for a signal single photon event. Notice the presence of no tracks and, therefore, no reconstructed interaction vertex in the event.

of photons or $Z \rightarrow e^-e^+$ events in data, as described in Ref. [76]. Using the corrected positions and its estimated errors, a straight line fit is performed in the $r - z$ and in the $r - \phi$ planes independently. The inward extrapolation of the fit in the $r - z$ plane results in the

determination of the z -coordinate of the interaction vertex, whereas the same procedure in the $r - \phi$ plane gives the distance of closest approach (DCA) to the z -axis of the detector. An illustration of this technique is shown in Figure 4.11.

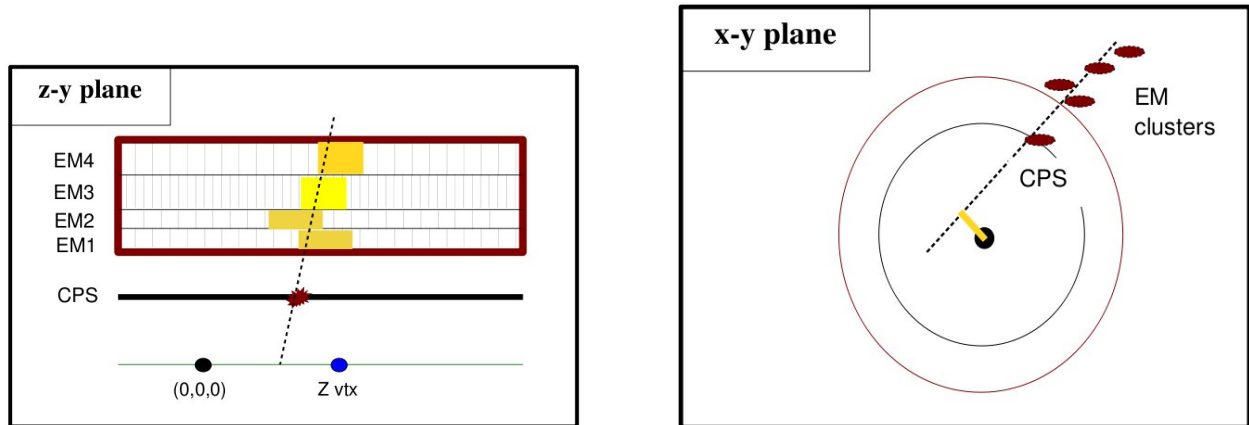


Figure 4.11: Illustration of the inward extrapolation of the the EM pointing algorithm fit in the $r - z$ plane (left), which predicts the z -coordinate of the interaction vertex, and in the $r - \phi$ plane (right), which predicts the DCA to the z -axis of the detector.

We will see, in the following sub-sections, how the tracker-independent variables that are measured by the EM pointing algorithm allow us to select single photon events and estimate the most difficult backgrounds in this analysis.

4.1.4 Single Photon Sample Selection

Photons are reconstructed in the detector as calorimeter clusters fulfilling the following requirements:

- At least 97% of the total energy is deposited in the EM section of the calorimeter for Run IIa data, and 95% for Run IIb data.
- It is, geometrically, within the η fiducial coverage of the calorimeter and tracking system in $|\eta_{det}| < 1.1$, i.e., in the central region of the detector.
- The calorimeter isolation variable, $\mathcal{I} = [(E_{0.4}^{tot} - E_{0.2}^{em}) - \alpha \cdot l] / E_{0.2}^{em}$, is required to be less than 0.07. In this equation, $E_{0.4}^{tot}$ denotes the total energy deposited in the calorimeter

in a cone of radius $\mathcal{R} = \sqrt{(\Delta\eta)^2 + (\Delta\phi)^2} = 0.4$, $E_{0.2}^{\text{em}}$ is the EM energy in a cone of radius $\mathcal{R} = 0.2$, l is the instantaneous luminosity, and α is a constant that takes different values for the central and end-cap regions of the calorimeter. For this analysis, which is restricted to the central region, α takes the values of zero and 0.0033 for Run IIa and Run IIb, respectively.

- Has track isolation, i.e, the scalar sum of the transverse momenta of all tracks which originate from the primary vertex in an annulus of $0.05 < \mathcal{R} < 0.4$ around the cluster is less than 2 GeV.
- The EM cluster width (squared) in $r \times \phi$ space in the third layer of the EM calorimeter is less than 14 cm² or 16 cm² for Run IIa or Run IIb data, respectively.

This set of conditions are known as *core* requirements and are given by the DØ Photon Identification Group [77, 78]. However, these requirements do not guarantee that only photons are selected. Electrons or jets can, for example, pass there selection criteria without much problem. For these reason we obtain the *photon* sample by selecting events with only one photon that pass the core criteria and the additional requirements described below.

4.1.4.1 Photon p_T , jet p_T , and \cancel{E}_T requirements.

We require events with photon $p_T > 90$ GeV and $\cancel{E}_T > 70$ GeV. Additionally, in order to reduce multijet background and to avoid large \cancel{E}_T due to mismeasurement of jet energy, we require no jets with $p_T > 15$ GeV.

The photon p_T requirement is optimized by computing the metric ϵ_S/\sqrt{B} , where ϵ_S is the efficiency of the signal and B is the number of background events. We use the Run IIa signal MC sample with $n = 2$ and the Run IIa $W + \gamma$ MC sample for the background. Figure 4.12 shows this *significance-like* quantity for the signal versus photon p_T minimum threshold.

The magnitude for the photon p_T threshold is also constrained by the high \cancel{E}_T requirement that was adopted in order to reduce the multijet background to negligible levels (see Section 4.2). One can clearly see, in Figure 4.38 and Eq. 4.3, a *turn-on* (after the multijet background fade-out region) occurring at about $\cancel{E}_T = 70$ GeV; thus, it is reasonable to set the photon p_T threshold to this value. Figure 4.13 shows the \cancel{E}_T distribution for Run IIa MC signal events with a minimum photon p_T of 90 GeV.

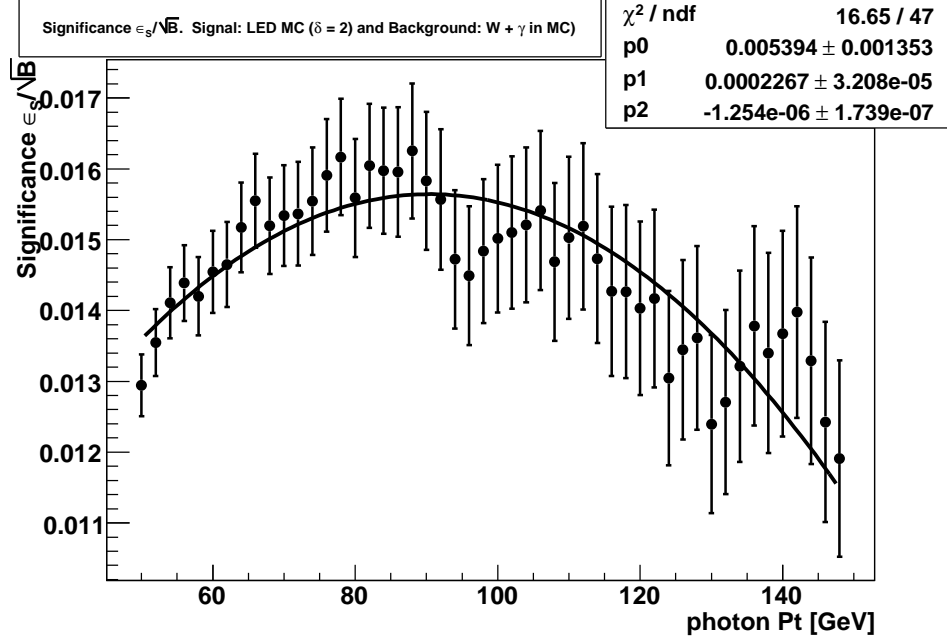


Figure 4.12: *Significance-like* metric ϵ_S/\sqrt{B} for the signal versus photon p_T threshold in Run IIa.

The inefficiency that the \cancel{E}_T requirement introduces in the signal selection is of the order of 10% for the different number of extra dimensions.

4.1.4.2 Anti-track match requirement

The main purpose of this requirement is to reduce the possibility of selecting an electron instead of a photon. We require that the photon have no associated track in the central tracking system nor a significant density of hits in the SMT of CFT systems consistent with a track. The latter requirement is described in more detail in Ref. [52]. This combination of requirements, known as the anti-track match requirement, was used successfully in Ref. [79] for an analysis performed on Run IIa data. The measured efficiency is 0.930 ± 0.010 . For Run IIb data, however, there is a significant loss in efficiency (0.796 ± 0.022) [80] due to higher occupancy in the tracker [81] due to higher instantaneous luminosities.

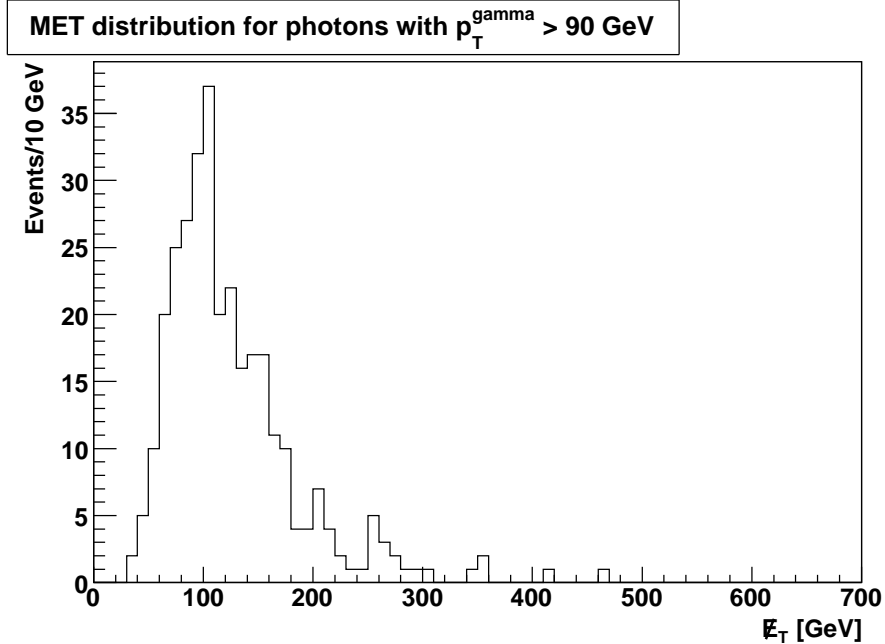


Figure 4.13: \cancel{E}_T distribution for Run IIa signal events with photon $p_T > 90$ GeV

4.1.4.3 CPS match requirement and EM pointing resolution

We require the photon candidate be matched to a CPS cluster. This selection condition was studied in Ref. [82] for Run IIa data and the efficiency was measured to be 0.880 ± 0.030 . We proceed, along the same lines, to estimate the efficiency of this requirement in Run IIb. We select $Z + \gamma$ events using a dielectron sample from Z decays to check the performance of the central preshower. We use a set of data with at least two high- p_T clusters where we select events with two electrons and one photon. The two electrons are selected by requiring two clusters with $p_T > 20$ GeV that have a track match, calorimeter isolation $\mathcal{I} < 0.07$, at least 95% of the energy in the EM section of the calorimeter, and shower shape consistent with that of an electron. At least one of them is required to be in the CC. The required photon has to be in the CC with $p_T > 15$ GeV, $\mathcal{I} < 0.07$, at least 95% of its energy in the EM section of the calorimeter, and with EM cluster width less than 16 cm^2 .

Figure 4.14 shows the three body mass distribution for all the events (points) and for events in which the photon has a cluster match in the CPS (open histogram). We select those events with three body mass between 82 GeV and 102 GeV.

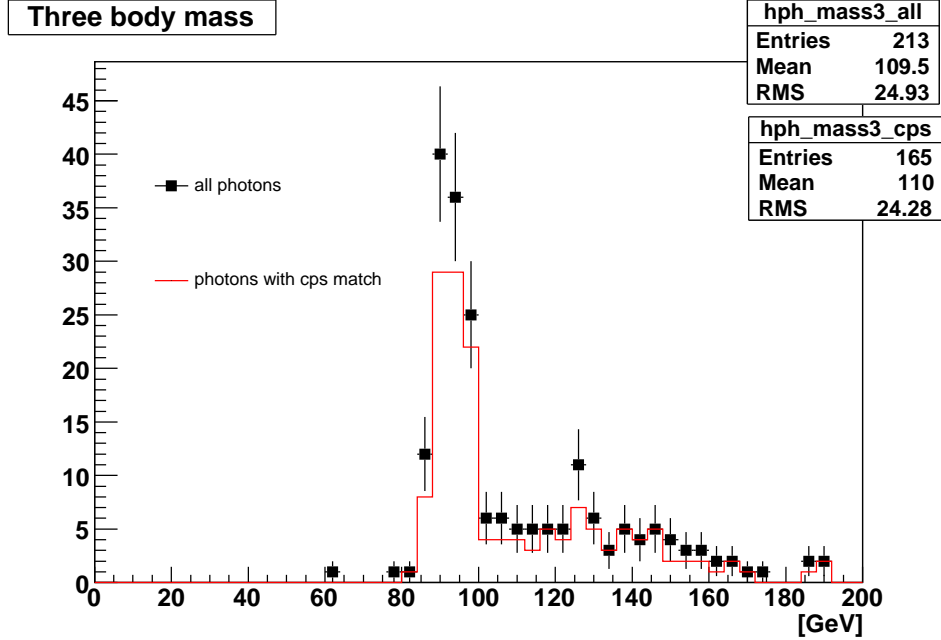


Figure 4.14: Three body mass distribution for $Z \rightarrow e^+e^-\gamma$ events in Run IIb data.

Inside this range, 90 events out of 117 passed the CPS match requirement, yielding an efficiency of 0.77 ± 0.04 . Figure 4.15 shows the efficiency of the CPS match versus the photon rapidity measured in data and in the official DØ MC $\gamma + jet$ events sample. The CPS matching efficiency in MC is comparable with that in data.

We take advantage of this data sample to test the resolution of the EM shower pointing by plotting (Figure 4.16) the difference between the z -position of the reconstructed vertex and the z -position from the photon pointing. The resolution in Run IIb epoch (about 3.5 cm) is degraded compared to Run IIa (2.3 cm) [82].

4.1.4.4 Muon and high- p_T track rejection

We reject events that have reconstructed muons of loose quality, as described earlier in Section 3.4. In order to further reject events with leptons that leave a distinguishable signature in the tracker but that are not reconstructed in the other subsystems of the detector, we impose a requirement on the p_T of any isolated track not to be greater than $p_{T_{max}}^{track}$, where $p_{T_{max}}^{track}$ takes the value of 6.5 GeV for Run IIa data and 8 GeV for Run IIb data. A track is considered to be isolated if the ratio between the scalar sum of the transverse momenta of

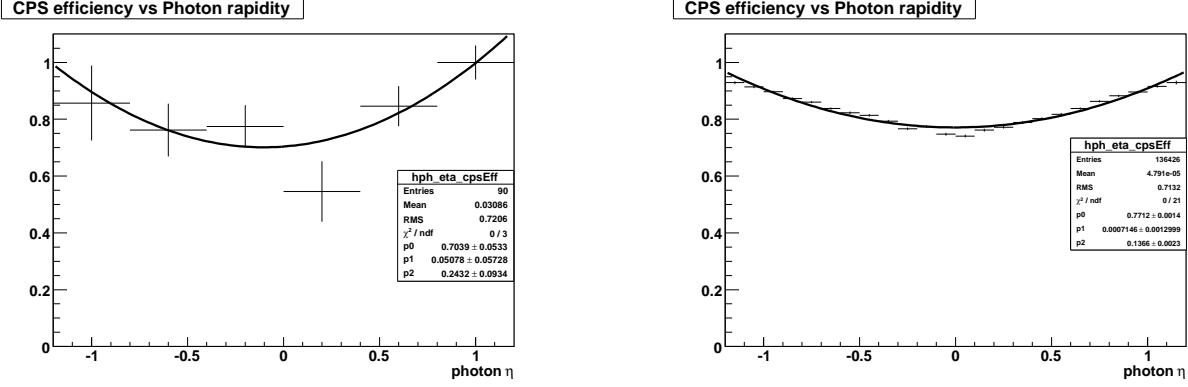


Figure 4.15: CPS match efficiency vs photon rapidity using $Z \rightarrow e^+e^-\gamma$ events in Run IIb data (left) and Run IIb MC (right).

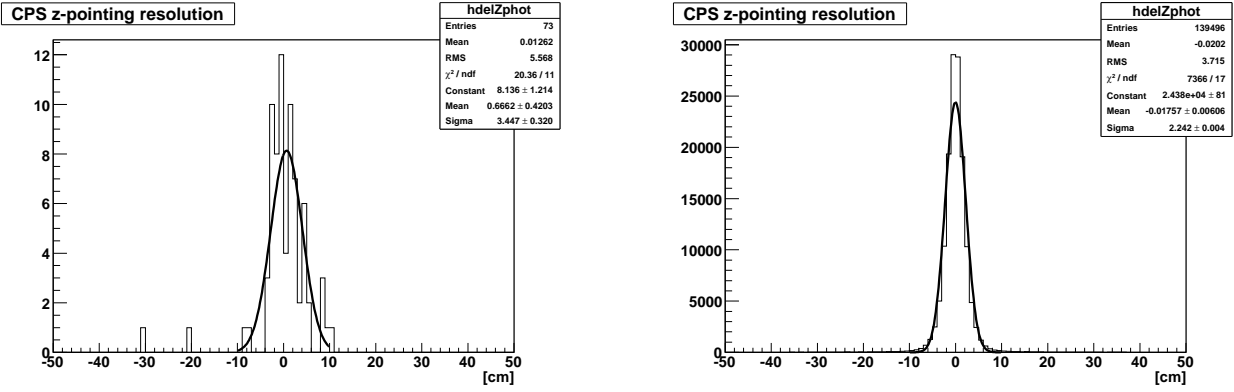


Figure 4.16: Pointing resolution measured using $Z \rightarrow e^+e^-\gamma$ events in Run IIb data (left) and MC (right).

all tracks that originate from the interaction vertex in an annulus of $0.1 < \mathcal{R} < 0.4$ around the track and the p_T of the track is less than $trkiso$, where $trkiso$ take the values of 0.3 for Run IIa and 0.9 for Run IIb. We choose to use an annulus with inner radius of 0.1 in order to account for possible tau narrow jets decays. The track in question is required to be within 2 cm of the primary vertex. In addition, we do not veto on any track that is within $\Delta R < 0.3$ around the photon EM cluster in order to account for possible early photon conversions.

We optimize this requirement using samples of $W \rightarrow e\nu$ events from data as the signal (see Section 4.2), and the $W + \gamma \rightarrow e\nu + \gamma$ MC samples as the background. Figure 4.17 shows the metric ϵ_S / \sqrt{B} (see Section 4.1.4.1) versus the minimum p_T of the track rejection

for different isolation values. The efficiency of this requirement is measured in $W \rightarrow e\nu$ data events and is estimated to be 0.865 ± 0.004 and 0.798 ± 0.002 for Run IIa and Run IIb data, respectively.

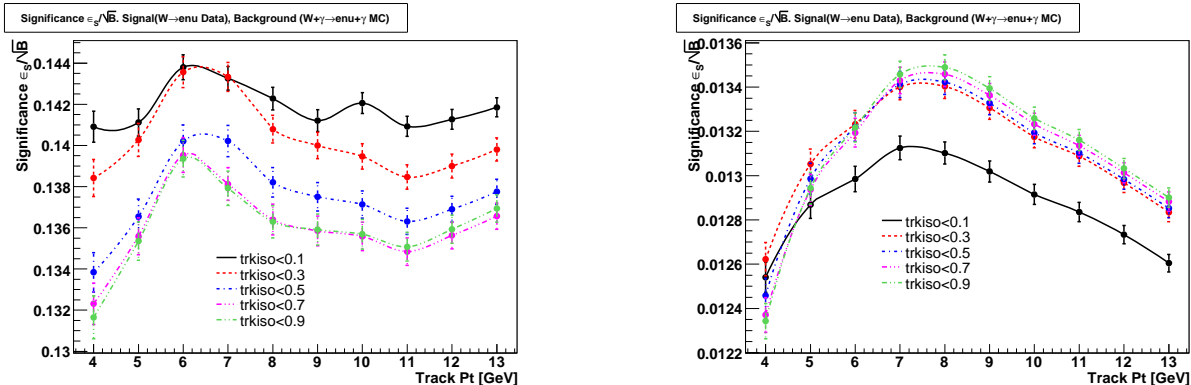


Figure 4.17: *Significance-like* metric ϵ_S/\sqrt{B} for the signal versus track p_T maximum threshold, for different isolation values. Run IIa data (left) and Run IIb (right) results are shown.

4.1.4.5 Cosmic muon rejection

We reject events with cosmic ray muons identified using the timing of the signal in the muon scintillation counters, as described in Section 3.4. We also reject events that have presence of a characteristic pattern formed by hits in the muon drift chambers and the photon EM cluster that is consistent with a cosmic muon undergoing bremsstrahlung in the calorimeter, i.e., if two of the muon A-segments align with the selected photon EM cluster.

The procedure is best described in Ref. [83], with some minor improvements to the implementation. The vectors from all muon A-segments in the event to the location of the photon EM cluster are first calculated and the angle (θ) between these vectors is then computed. Since we expect the radiated photons to be practically collinear with the muon (Figure 4.9), the size of the angle θ serves as a handle to reject cosmic events. We reject all events containing a best aligning trio with $|\cos(\theta)| > 0.9$ for Run IIa and $|\cos(\theta)| > 0.95$ for Run IIb. Figure 4.18 shows the cosine of the angle θ for the best aligning trio in each event in Run IIa and Run IIb photon samples.

The efficiencies for cosmic muon rejection measured in $W \rightarrow e\nu$ data events are estimated

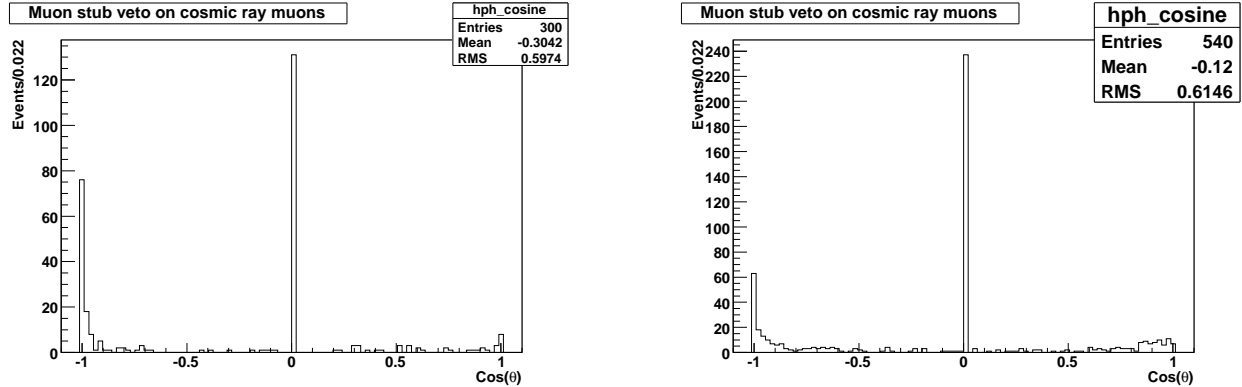


Figure 4.18: Cosine of θ distribution for Run IIa (left) and Run IIb (right) photon samples. Zero is a default value for those events that do not have muon A-segments or for events with muon A-layer positions exceeding the maximum allowed size, as stated in Ref. [2].

to be 0.909 ± 0.004 and 0.859 ± 0.003 for Run IIa and Run IIb, respectively.

4.1.4.6 Pointed vertex requirement

We require the presence of at least one reconstructed interaction vertex consistent with the measured direction of the photon. In particular, we require that the z -coordinate of at least one interaction vertex in the event be within 10 cm of the position predicted by the pointing algorithm. We loop over all the reconstructed vertices in the event and compare their z -position with the best fitted z -position of the primary vertex given by the pointing algorithm. ΔZ_{min} is the distance along the z -axis between the reconstructed vertex that best agrees with that from the pointing tool and the pointed vertex. Figure 4.19 shows the distribution of this variable for photon sample² events, signal-like (e/γ sample) events, non-collision events, and misidentified jet events in Run IIa³. Similar plots are found in Figure 4.20 for Run IIb.

Clearly, the photon sample comprises different contributions; in particular, we can detect one with a narrow shape, just like a clean LED signal would give, and a wider one, most likely coming from non-collision events. Figure 4.21 shows the DCA distribution (from pointing) for the Run IIa photon sample before and after applying the requirement on ΔZ_{min} . As it will

²The photon sample used in this section requires events with photon $p_T > 50$ GeV and $\cancel{E}_T > 45$ GeV.

³The e/γ sample, non-collision sample, and misidentified jet sample are selected in the same way as described in Section 4.2.

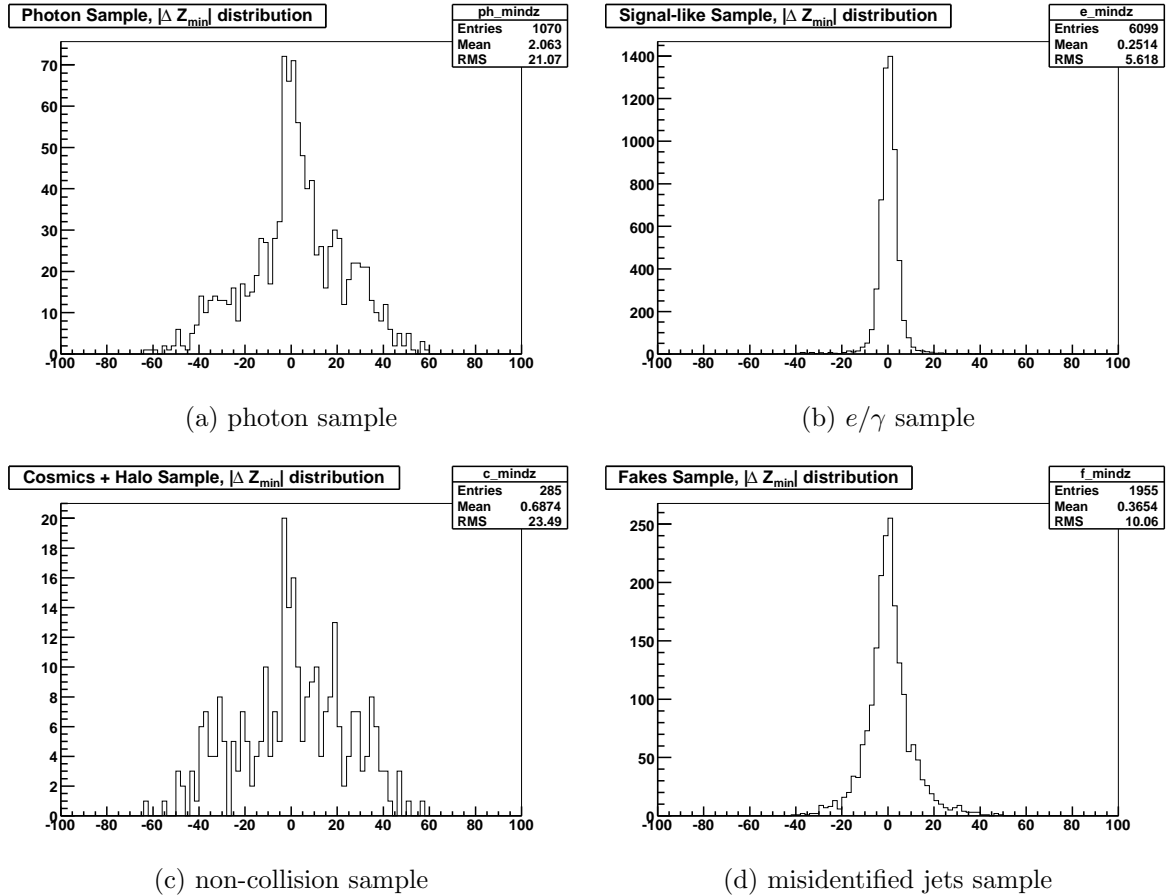


Figure 4.19: Distribution of the distance along the z -axis between the reconstructed vertex that best agrees with that from the pointing tool and the pointed vertex for different Run IIa data samples.

become clear in Section 4.2, the tail of the distribution at higher DCA values ($DCA > 4$ cm) is almost entirely populated by non-collision events. Events with higher DCA values are removed in greater number than those in the lower DCA region. Equivalent plots can be found in Figure 4.22 for Run IIb data. We measure the efficiency of this requirement in $W \rightarrow e\nu$ data events. For Run IIa the efficiency is 0.942 ± 0.003 while for Run IIb it is 0.907 ± 0.003 .

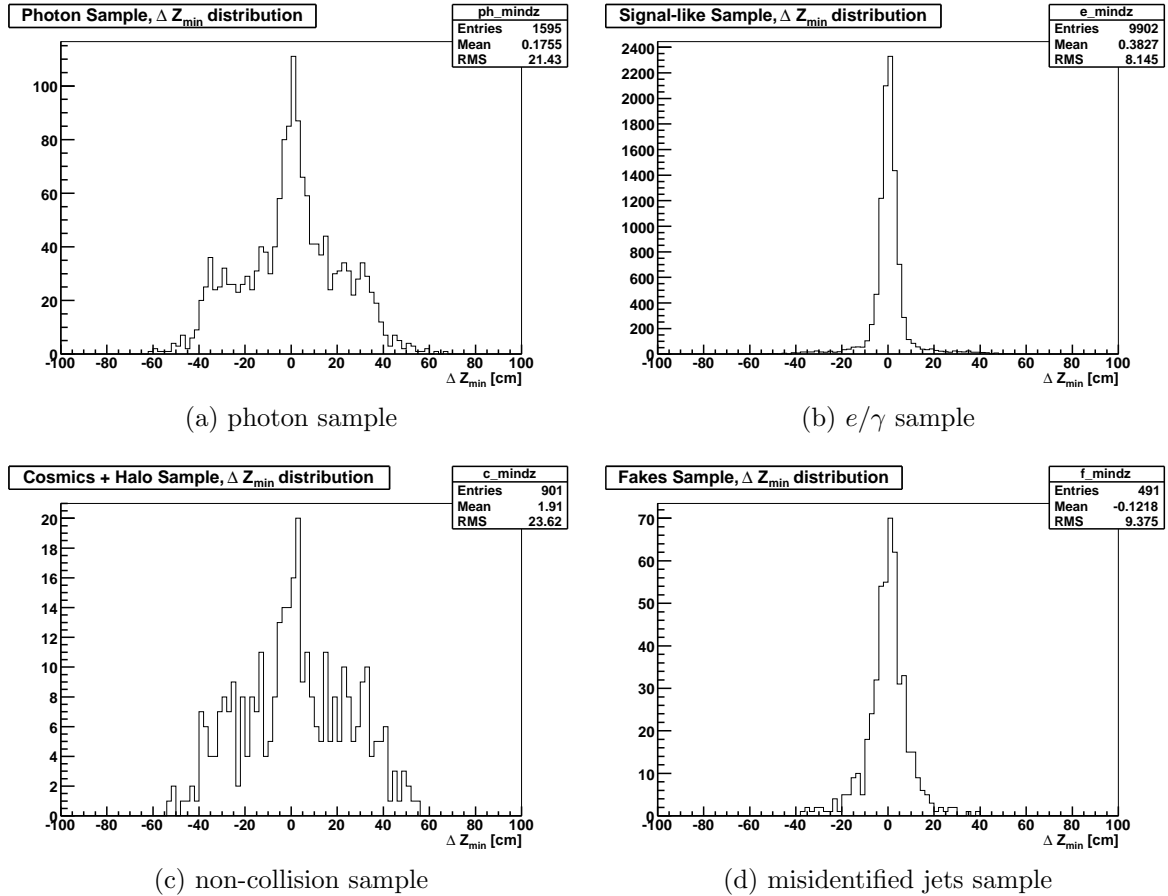


Figure 4.20: Distribution of the distance along the z -axis between the reconstructed vertex that best agrees with that from the pointing tool and the pointed vertex for different Run IIb data samples.

4.1.4.7 Photon shower shape requirements

We require photon EM showers to deposit at least 10% of their total energy in the third layer of the EM section of the calorimeter. EM objects coming from the interaction region of the detector are expected to deposit the bulk of their energy in the third layer of the EM part of the calorimeter. Particles which are not coming from that region will most likely miss all the material in front of the first calorimeter layer. Thus, due to the fact that the first EM layer of the calorimeter receives the largest of the compensating weights among all EM layers (which accounts for the vast amount of material in front of it), particles which are product of cosmic ray muons or beam halo contamination will have large energy fraction

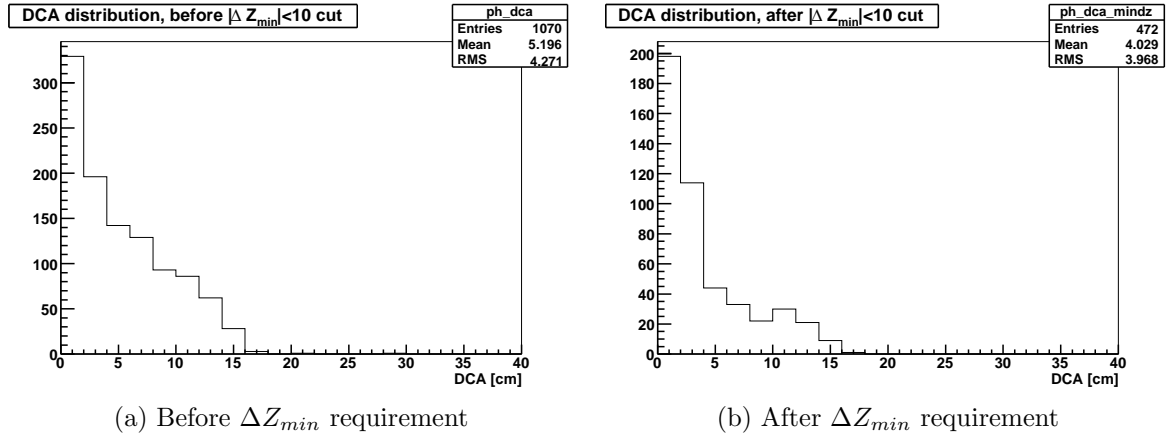


Figure 4.21: DCA distribution of the Run I Ia photon sample before and after applying a requirement on ΔZ_{min} .

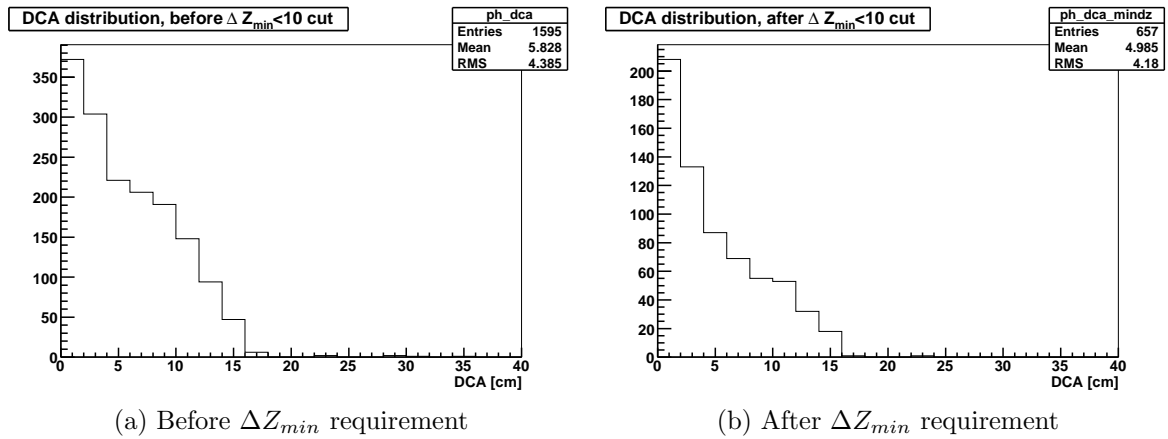


Figure 4.22: DCA distribution of the Run I Ib photon sample before and after applying a requirement on ΔZ_{min} .

in the first EM layer and small energy fraction in the third layer.

Figure 4.23 shows the distribution of the energy fraction at the third EM layer of the calorimeter for photon sample⁴ events, signal-like (e/γ sample) events, non-collision events, and misidentified jet events in Run I Ia.⁵ Similar plots are found in Figure 4.24 for Run I Ib.

⁴The photon sample used in this section requires events with photon $p_T > 50$ GeV and $\cancel{E}_T > 45$ GeV.

⁵The e/γ sample, non-collision sample, and misidentified jet sample are selected in the same way as described in Section 4.2.

Additionally, Figure 4.25 shows the energy fraction at the first layer of the EM calorimeter for non-collision events.

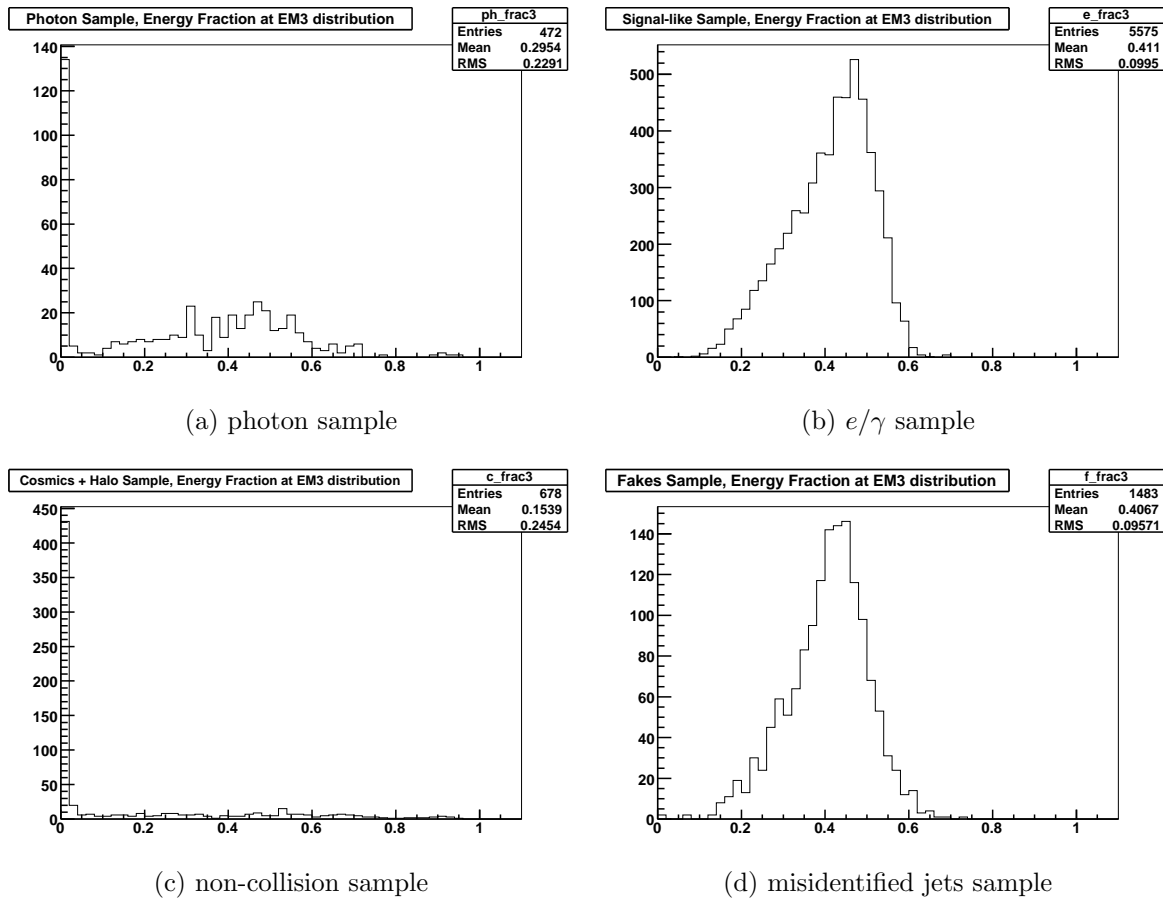


Figure 4.23: Distribution of the energy fraction at the third EM layer of the calorimeter for different Run IIa data samples.

Figure 4.26 shows the DCA distribution (from pointing) for the Run IIa photon sample before and after applying the requirement on ΔZ_{min} . We use $W \rightarrow e\nu$ events in data to measure the efficiency of this requirement and find it to be 1.000 ± 0.001 .

Additionally, we impose a requirement on the H-matrix [51] variable $Hmx7 < 30$ in Run IIa data and $Hmx7 < 35$ in Run IIb data in order to eliminate abnormal energetic photons in untagged events with hardware problems in the calorimeter [84].

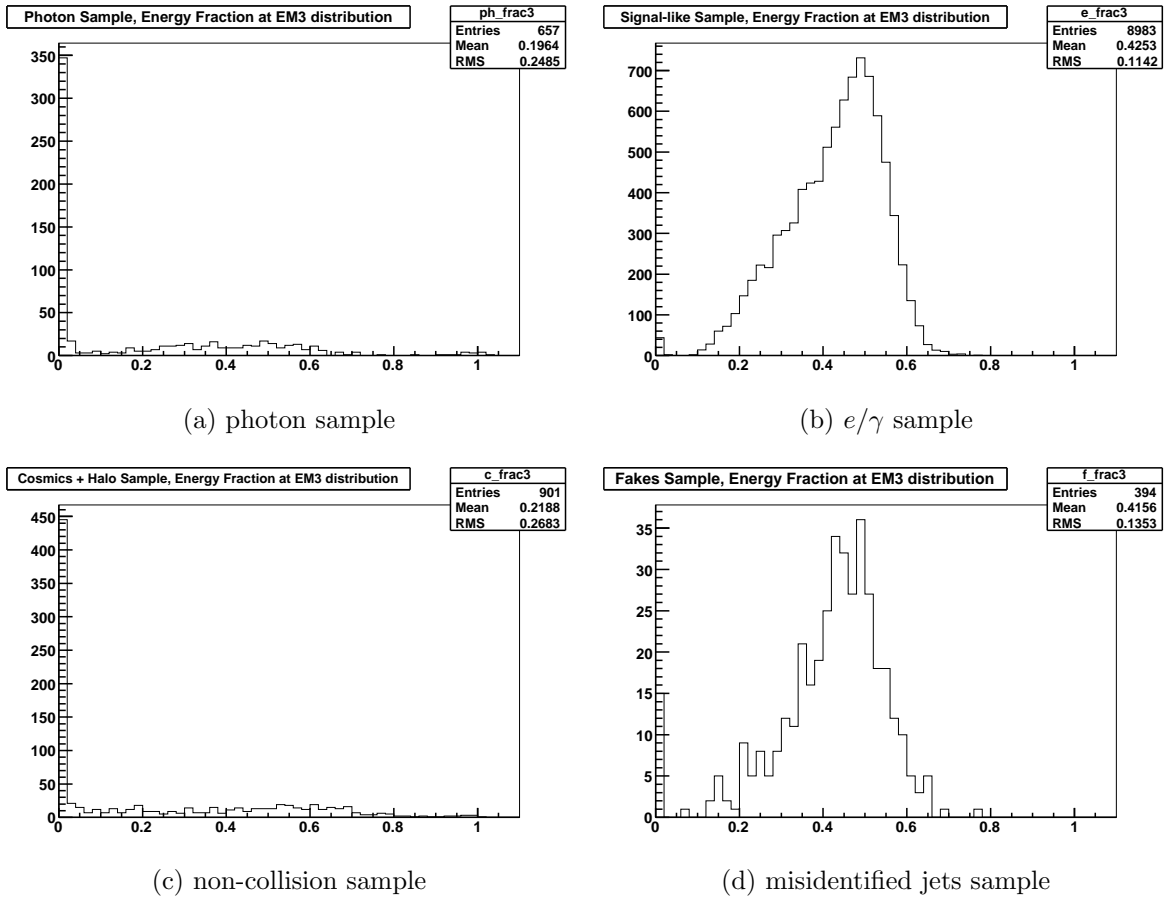


Figure 4.24: Distribution of the energy fraction at the third EM layer of the calorimeter for different Run IIb data samples.

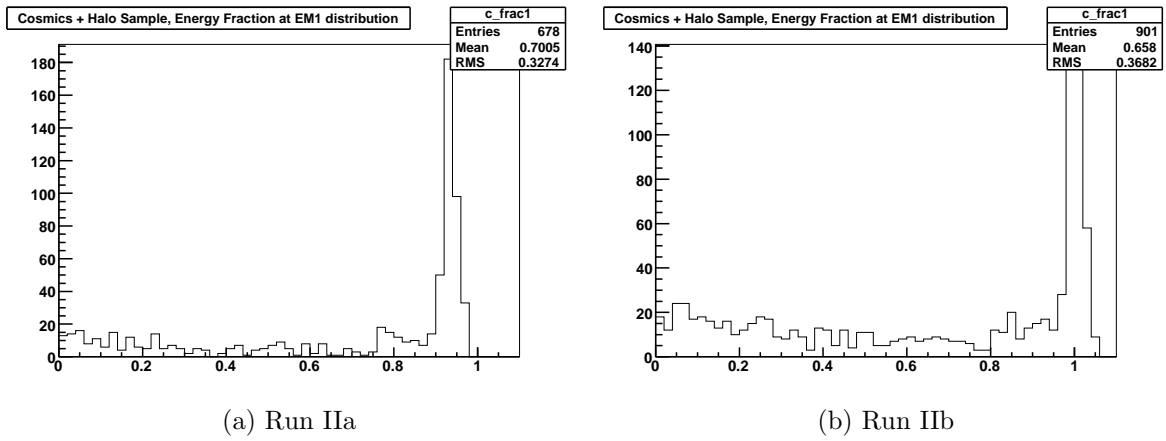


Figure 4.25: Distribution of the energy fraction at the first EM layer of the calorimeter for non-collision events.

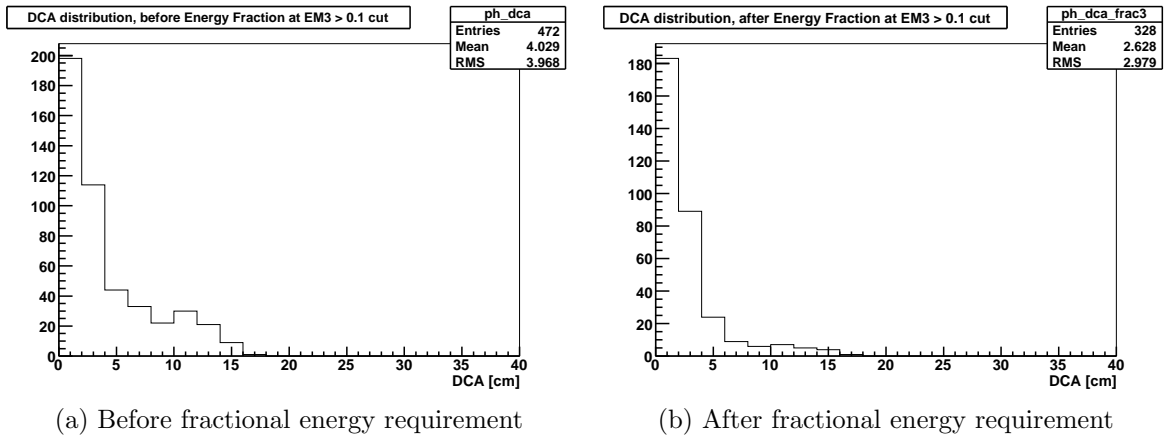


Figure 4.26: *DCA* distribution of the Run IIa photon sample before and after applying a requirement on the fractional energy at the third EM layer of the calorimeter.

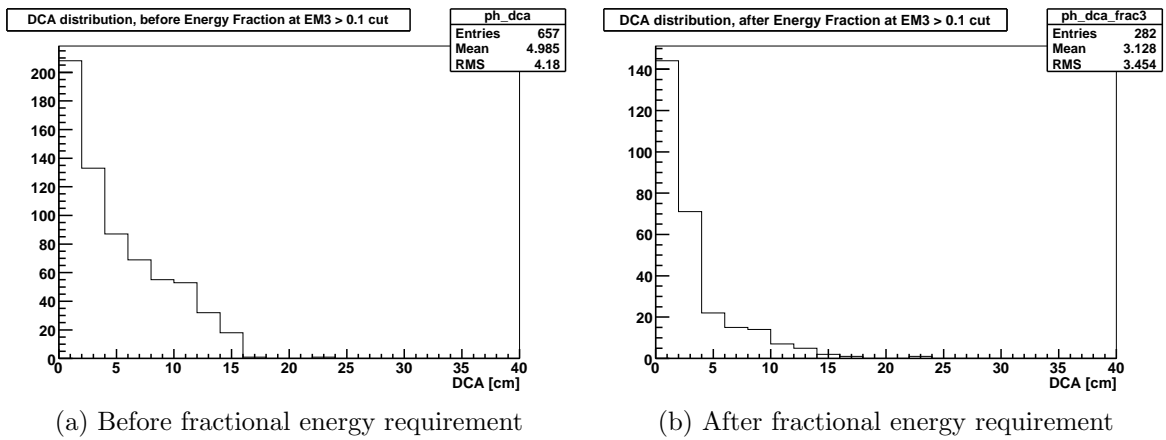


Figure 4.27: *DCA* distribution of the Run IIb photon sample before and after applying a requirement on the fractional energy at the third EM layer of the calorimeter.

4.2 Background Estimation

Figure 4.28 shows the photon p_T distributions in the photon samples after the requirements described in the last section. Despite all the efforts made in order to reject unwanted events with non-collision particles, the final photon samples still show evidence of having a large number of them, as can be inferred from the presence of events at higher values of DCA in Figure 4.29. We envisage a way to determine this background and estimate the contributions from the remaining background sources for this analysis.

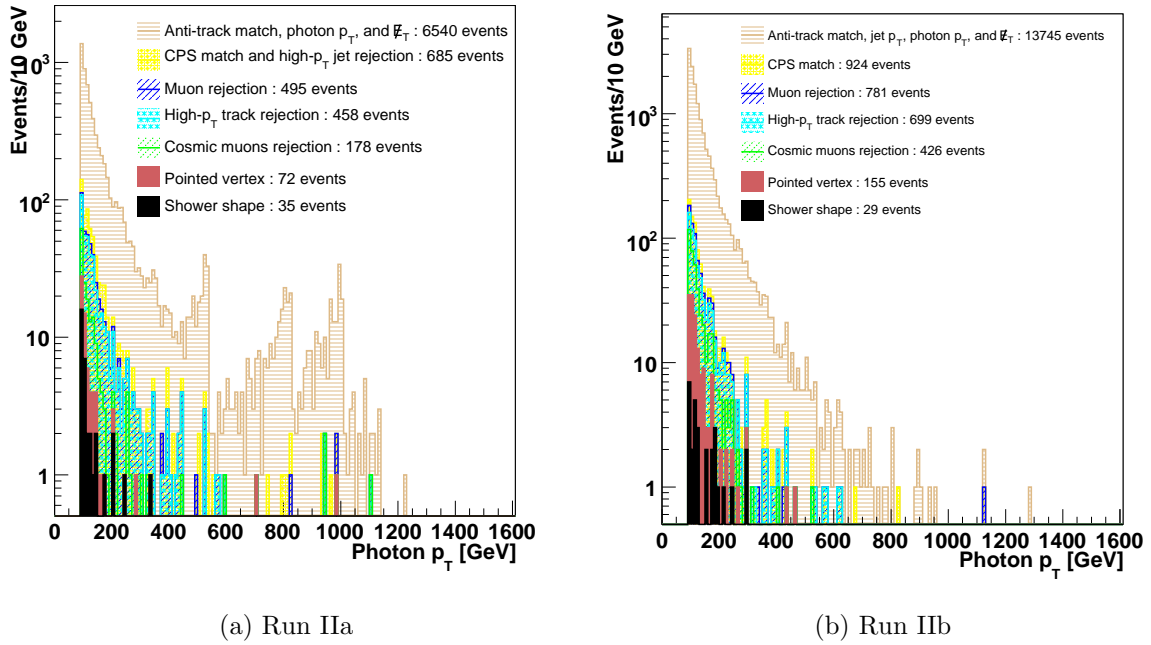


Figure 4.28: Photon p_T distribution in semi-log scale for the photon sample. The peaks in one of the Run IIa distributions is due to calorimeter noise. The requirements imposed successfully reject those problematic events.

4.2.0.8 Non-collision and Misidentified jets background estimation

We use the EM pointing DCA to estimate the remaining background from jet-photon misidentification and non-collision events. Misidentified jets have poor pointing resolution, and therefore a wider DCA distribution compared to electrons or photons. Likewise, the DCA distribution for photon candidates in non-collision events have an even wider shape.

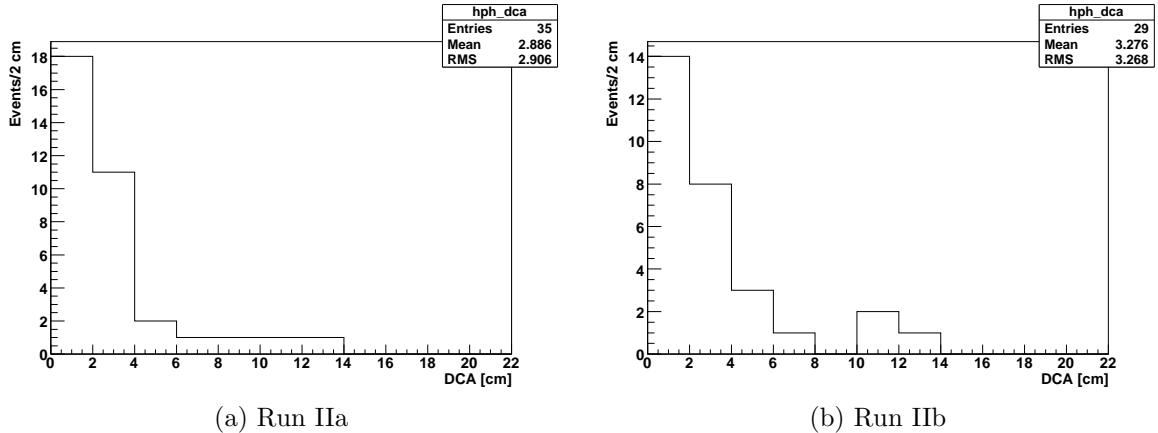


Figure 4.29: Photon DCA distributions in the photon sample.

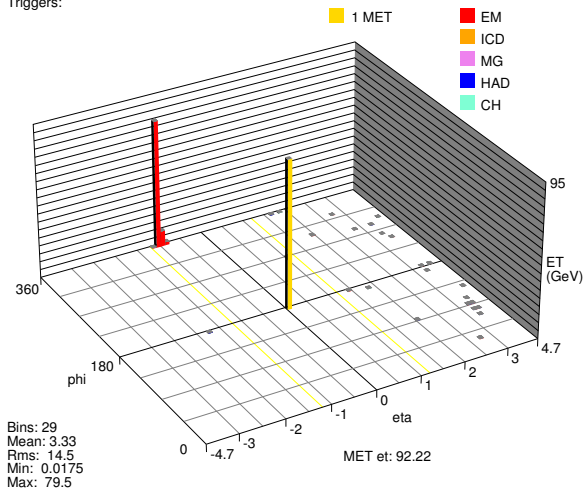
We prepare three DCA distribution templates: the *non-collision* template, the *misidentified jets* template, and the e/γ template. The first template is obtained from a sample in which a photon candidate, passing the same quality requirements as for the photon sample, is selected from events with no hard scatter (no reconstructed interaction vertex or fewer than three reconstructed tracks, see Figure 4.10, 4.30, and 4.31), or from events with identified cosmic muons (Figure 4.9).

The misidentified jets template is extracted from the *fake photon* sample, which fulfills exactly the requirements as the photon sample except that the photon track isolation requirement is inverted. This sample is dominated by misidentified jets. We cross-check the shape of this template with the one obtained from an *EM plus jet* sample, where the EM object passes all photon identification requirements except the track isolation, and where the jet approximately balances the EM object in the transverse plane. We find good agreement between them, as can be appreciated in the left plot of Figure 4.32. Finally, the e/γ template is obtained from a data sample of isolated electrons. The shape of the templates for Run IIa can be seen in the right plot of Figure 4.32. Additionally, Figure 4.33 shows the template shapes for Run IIb and their comparison with the ones from Run IIa.

We fit the DCA distribution in the *photon* sample to a linear sum of the three templates, fixing the contribution of *misidentified jets* as described below, and determine the e/γ and *non-collision* contributions. The results of the fit are illustrated in Figure 4.34. Most of the signal photons have DCA less than 4 cm, therefore we limit our analysis to this particular

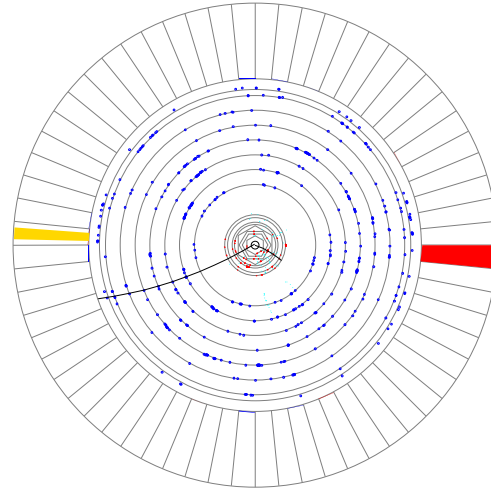
Run 167191 Evt 4284804

Triggers:

(a) $\eta - \phi$ lego plot

Run 167191 Evt 4284804

ET scale: 93 GeV

(b) $x - y$ view

Run 167191 Evt 4284804

(c) $z - y$ view

Run 167191 Evt 4284804

E scale: 80 GeV

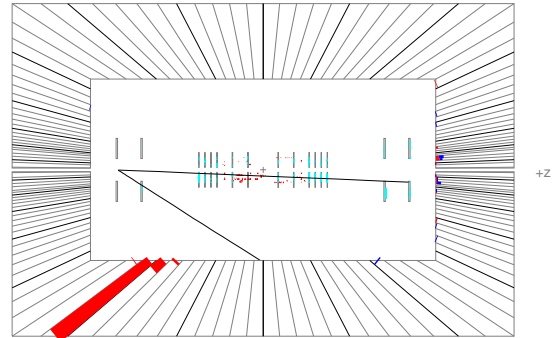
(d) $r - z$ view tracker and calorimeter

Figure 4.30: Detector display for a beam halo event with a single photon. The number of reconstructed tracks is less than three.

window, which contains 29 and 22 data events in Run IIa and Run IIb, respectively.

The total number of background events from misidentified jets (N_{misid}) are predicted from the *fake photon* sample based on the rates at which jets, passing all other photon identification criteria, fail or pass the track isolation requirement. To measure those rates

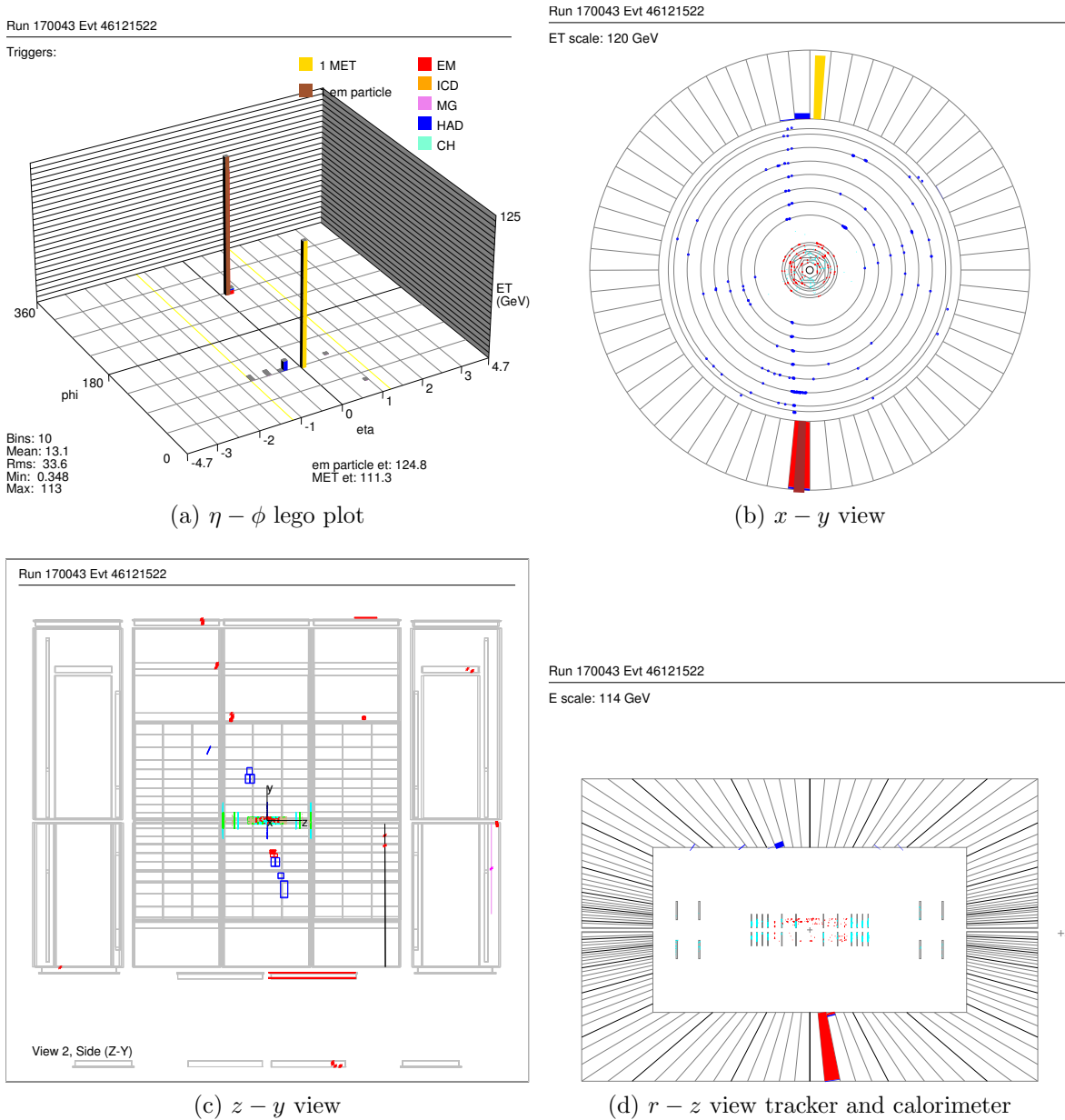


Figure 4.31: Detector display of a cosmic ray muon event with a single photon. No tracks and, therefore, no vertices are reconstructed.

we use the EM plus jet sample. This is done in order to improve the poor results for the misidentified jet component as a consequence of the e/γ and misidentified jets templates having too similar shapes. We first determine the number of events (N_1) in the sample that fail the track isolation requirement. We then fit (Figure 4.35) the DCA distribution of the

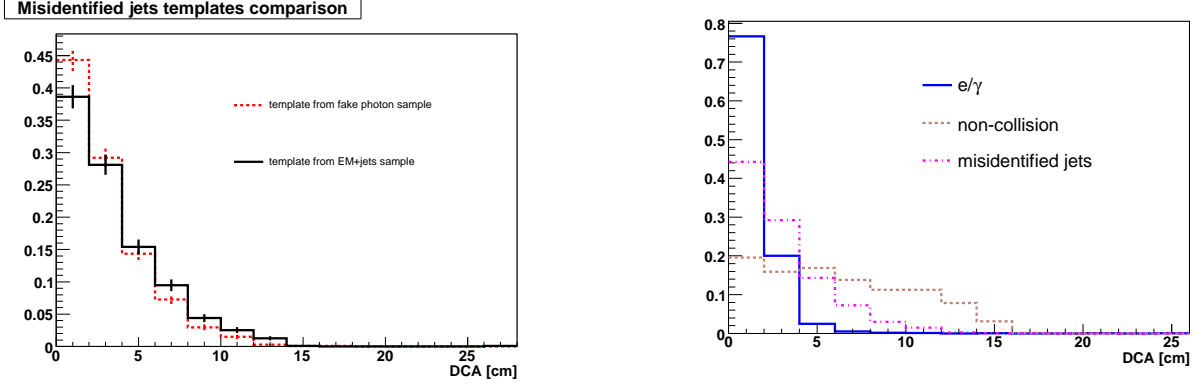


Figure 4.32: Comparison between misidentified jets DCA templates from two different samples in Run IIa (left). DCA template shapes in Run IIa (right).

events that pass the track isolation to a linear sum of the e/γ and misidentified jets templates in order to extract the number of misidentified jets (N_2) passing the track isolation. N_{misid} is then equal to the number of events in the fake photon sample multiplied by N_2/N_1 . The uncertainty on the number of misidentified jets is estimated by varying the central value of the result in the last fit by plus and minus one standard deviation, and by seeing how the total background contribution changes. We take half the total spread as the final uncertainty.

We take into account the small systematic error from the uncertainty in the shape of the e/γ template contribution. We estimate this uncertainty in Run IIa by using two extra photon DCA shapes from $Z\gamma \rightarrow e^+e^-\gamma$ and $Z\gamma \rightarrow \mu^+\mu^-\gamma$ decays. Figure 4.36 compares the shapes used. The averaged difference in the result for the non-collision number of events, when the different shapes are used, was calculated to be 0.4 events.

Figure 4.37 illustrates the validity of the method by showing the photon azimuthal distribution in a photon sample that suffers a much bigger contamination from non-collision events and that has lower kinematical requirements, namely, photon $p_T > 50$ GeV and $\cancel{E}_T > 45$ GeV. The fractional contributions of the different backgrounds are taken from the results of a DCA fit similar to the one described above. The two humps at about zero and 3.1 radians are consistent with the assumption that halo particles, for instance, deposit their energy mainly along the plane of the beam pipe.

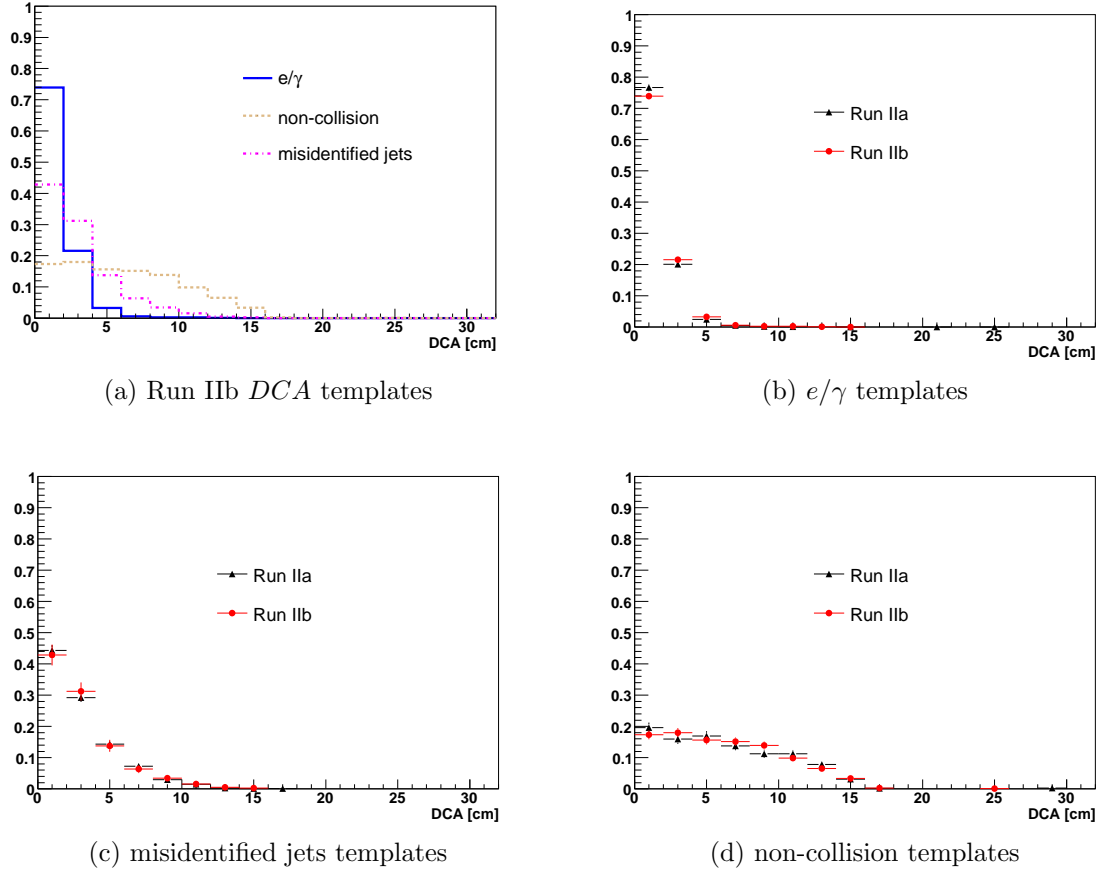


Figure 4.33: (a) DCA templates in Run IIb. (b,c,d) Comparison between shapes in Run IIa and Run IIb.

4.2.0.9 Additional SM background estimation

$W \rightarrow e\bar{\nu}$ background where the electron is misidentified as a photon is estimated directly from data using the electron sample. We apply the same requirements as for the photon sample and multiply the remaining number of events, before the isolated high- p_T track rejection requirement, by $(1 - \epsilon_{trk})/\epsilon_{trk}$, where ϵ_{trk} is the track match efficiency measured to be 0.980 ± 0.001 [77, 78]. We then multiply this number by the efficiency of each of the remaining requirements, namely, high- p_T track rejection, cosmic muons rejection, pointed vertex requirement, photon shower shape requirements, and DCA requirement.

The background contributions from $W + \gamma$ production and $Z + \gamma \rightarrow \nu\bar{\nu} + \gamma$ production are estimated using the MC samples described in Section 4.1.2. For Run IIb, where the

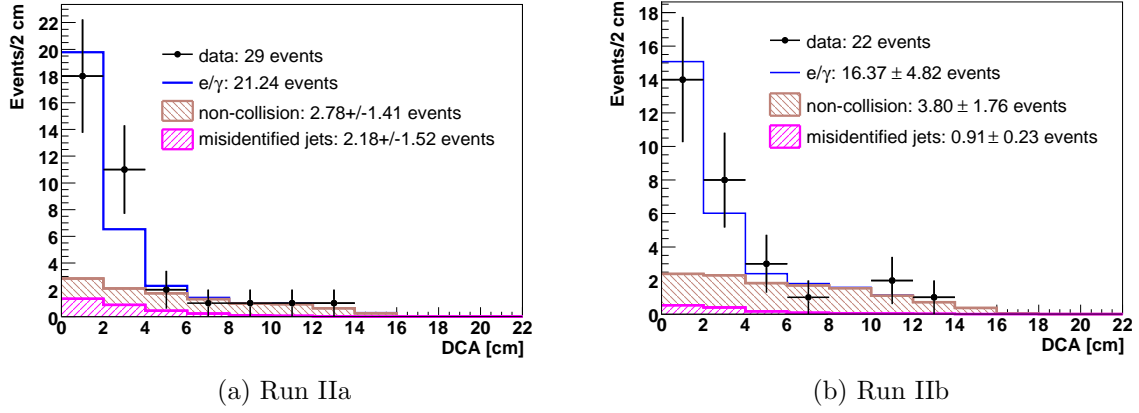


Figure 4.34: DCA distribution for the selected events in data (points with statistical uncertainties). The different histograms represent the estimated background composition from the template fit to this distribution. The number of events within a window of 4 cm in DCA are shown.

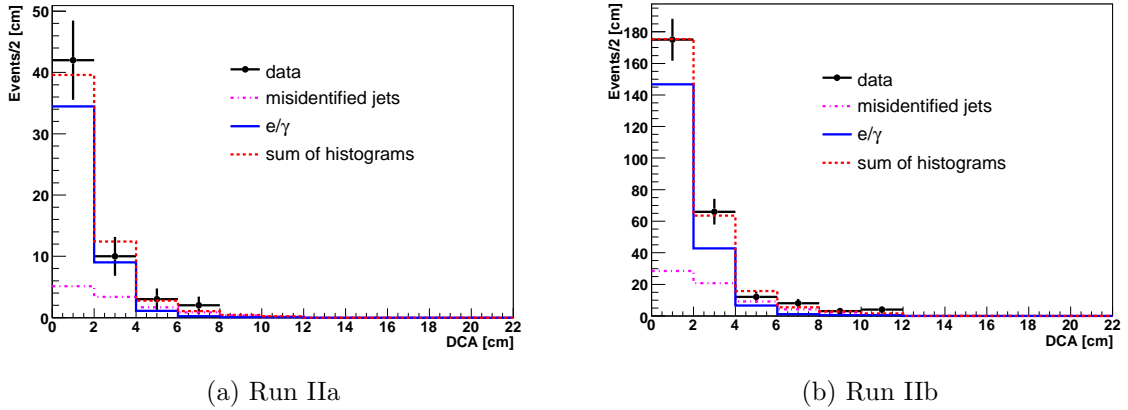


Figure 4.35: DCA template fit using the EM plus jet sample for Run IIa and Run IIb.

instantaneous luminosities are considerably higher than in Run IIa, we apply a luminosity weight to the MC samples in order to match the data. We apply the same requirements as for the photon sample and employ a data/MC scale factors to adjust for the differences between efficiencies in data and simulation. The scale factor values are 0.95 ± 0.05 for photon identification (K^γ) [77, 78], 0.99 ± 0.07 for loose muon identification (K^μ) [56], and 0.94 ± 0.07 for track reconstruction (K^{trk}) [56]. Table 4.5 shows the methodology used for calculating

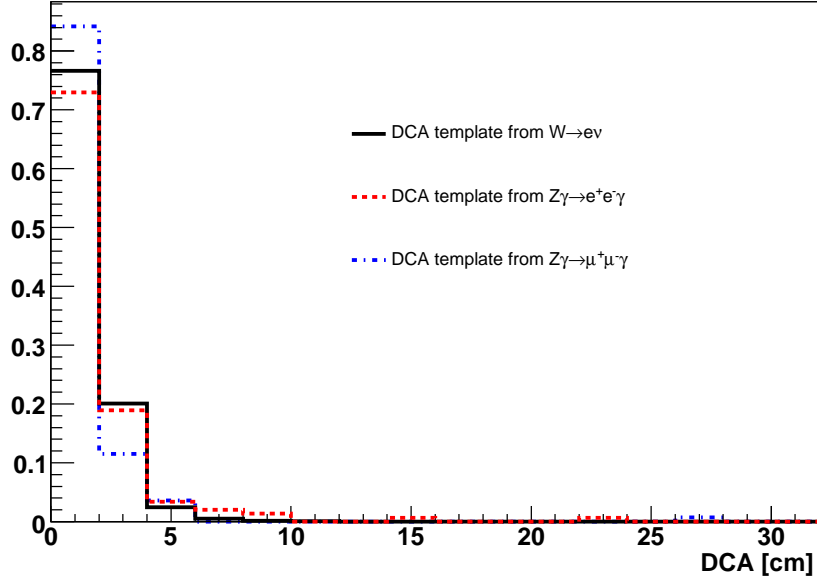


Figure 4.36: e/γ DCA templates comparison.

the number of remaining events in data after selecting these objects in MC samples. The results are then used to estimate the total acceptance in data, and to calculate the final number of expected events for these SM backgrounds. Table 4.6 shows a summary of the different types of background that were estimated using data and MC.

In order to check whether we suffer from multijet or any other extra source of background, we release the \cancel{E}_T kinematical requirement and plot the missing transverse energy distribution in the photon sample for Run IIa, with all the backgrounds overlaid (Figure 4.38). We are careful to take the \cancel{E}_T spectrum for the non-collision contribution (estimated above as a fraction of final candidate events) from a region where the signal is small, in order to avoid any possible bias related to signal region dependence. An exponential fit (Figure 4.39) to the difference between the photon sample data and the total accounted background at low values of \cancel{E}_T gives the following result for the number of events coming from multijet background or any other source:

$$N_{\text{multijet}} = \exp(7.88 - 0.12 \cdot \cancel{E}_T) \quad (4.3)$$

Thus, multijet events contributing to the background becomes negligible at values of

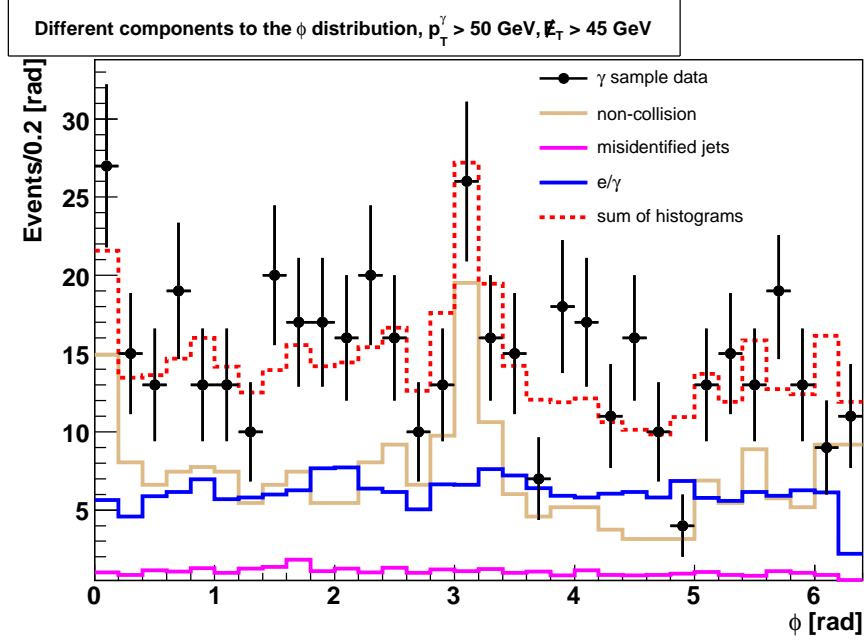


Figure 4.37: Photon azimuthal distribution in a photon sample with lower kinematical requirements. The different background components are shown.

Table 4.5: Methodology used for calculating the number of remaining events in data when MC samples are used.

Selection (rejection) criteria	Number of events in MC	Number of events in DATA
photon ID	N_0	$N_0 \cdot K^\gamma$
photon ID + muon selection	N_1	$N_1 \cdot K^\mu \cdot \frac{N_0 \cdot K^\gamma}{N_0} = N_1 \cdot K^\mu \cdot K^\gamma$
photon ID + muon rejection	$N_0 - N_1$	$K^\gamma \cdot (N_0 - N_1 \cdot K^\mu)$
photon ID + muon rejection + isolated high- p_T track selection	N_2	$N_2 \cdot K^{trk} \cdot \frac{K^\gamma \cdot (N_0 - N_1 \cdot K^\mu)}{N_0 - N_1}$
photon ID + muon rejection + isolated high- p_T track rejection	$N_0 - N_1 - N_2$	$K^\gamma \cdot (N_0 - N_1 \cdot K^\mu) \cdot \left[1 - \frac{N_2 \cdot K^{trk}}{N_0 - N_1}\right]$

Table 4.6: Data and estimated backgrounds for Run IIa and Run IIb.

Background	Number of expected events, Run IIa (1 fb^{-1})	Number of expected events, Run IIb (1.7 fb^{-1})	Number of expected events, combination (2.7 fb^{-1})
$Z + \gamma \rightarrow \nu\bar{\nu} + \gamma$	12.1 ± 1.3	17.4 ± 2.2	29.5 ± 2.5
$W \rightarrow e\nu$	3.8 ± 0.3	4.7 ± 1.7	8.5 ± 1.7
Non-collision	2.8 ± 1.4	3.8 ± 1.8	6.6 ± 2.3
Misidentified jets	2.2 ± 1.5	0.91 ± 0.23	3.1 ± 1.5
$W + \gamma$	1.5 ± 0.2	0.72 ± 0.15	2.22 ± 0.3
Total Background	22.4 ± 2.5	27.5 ± 3.3	49.9 ± 4.1
Data	29	22	51

missing transverse energy higher than 70 GeV. We assume this to be true in Run IIb as well.

The photon p_T distributions for the photon sample in Run IIa and Run IIb, and for the combined photon sample can be seen in Figure 4.40 and Figure 4.41, respectively. Additional distributions can be found in App. ??.

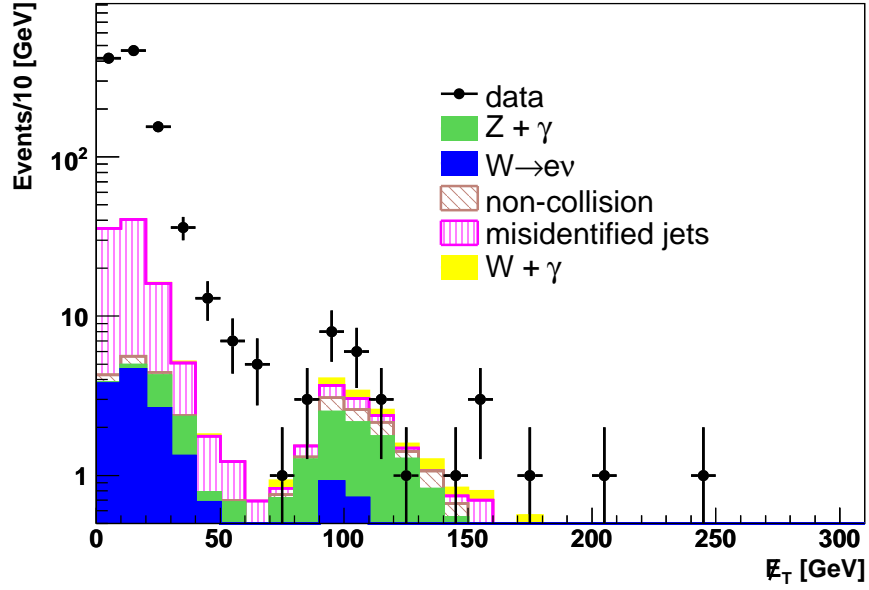


Figure 4.38: Missing transverse energy distribution in semi-log scale for Run IIa photon sample after releasing the $E_T^\#$ requirement.

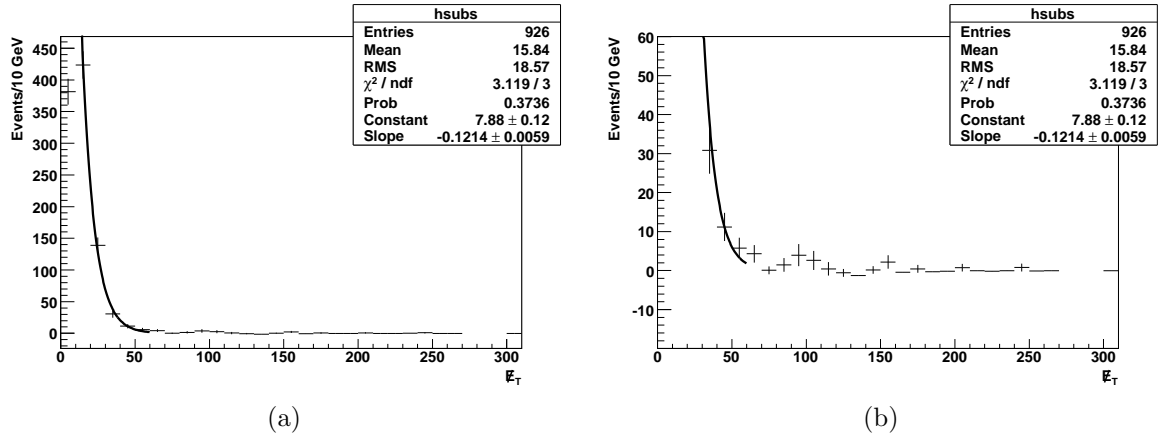


Figure 4.39: (a) Exponential fit to the difference between data and the total accounted background at low E_T in Run IIa data. (b) Zoomed-in figure.

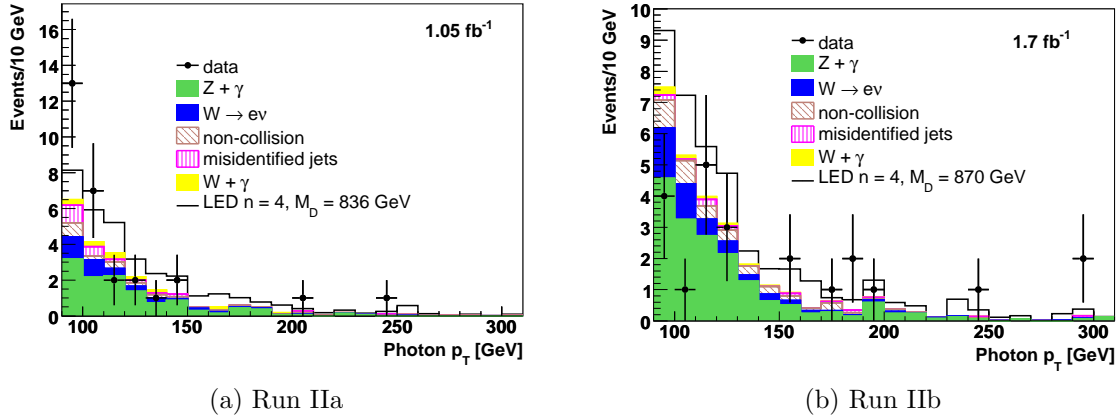


Figure 4.40: Photon p_T distribution for the final candidate events in Run IIa and Run IIb photon samples (data show statistical uncertainties). The LED signal is stacked on top of SM backgrounds.

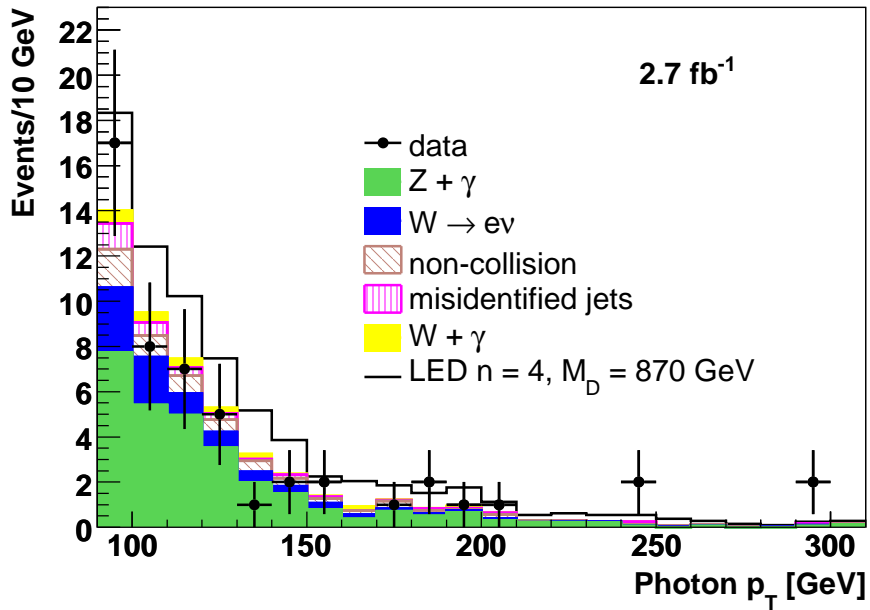


Figure 4.41: Photon p_T distribution for the final candidate events in the combined Run IIa and Run IIb photon sample (data show statistical uncertainties). The LED signal is stacked on top of SM backgrounds.

CHAPTER 5

RESULTS AND CONCLUSIONS

Before making any assertion about the presence of LED in our universe, it is necessary to take into account the systematic uncertainties on the SM backgrounds and on the predicted signal. Section 5.1 summarizes these uncertainties. Data and the SM expectation agree (Table 4.6), so we employ a frequentist technique (Section 5.2) to set lower limits for the fundamental Planck scale M_D . The results are presented in Section 5.3. We conclude this dissertation with Section 5.4 where we present a summary of the results and make our final remarks.

5.1 Systematic Uncertainties

The total uncertainties presented in Table. 4.6 include the contribution of systematic uncertainties. The main sources are the uncertainty in the photon identification efficiency (5%), which is propagated via correction factors for MC simulations, the uncertainty in the total integrated luminosity (6.1%), and the uncertainty in the signal acceptance from the PDFs (4%). For the SM backgrounds estimated from MC, the quoted uncertainties include the uncertainty in the theoretical cross section, which is dominated by the uncertainty in the next-to-leading-order K factors (7%), as mentioned in Section 4.1.2. The uncertainty in the width of the e/γ sample DCA template results in an additional systematic uncertainty of 0.4 events in the non-collision background estimate.

5.2 Limit Setting Technique

Following the guidelines given in Ref. [85], we choose the *Modified Frequentist Method* [86] as the procedure for combining the analyses and computing limits. This method uses a

likelihood ratio of Poisson probabilities (Eq. 5.1) as a *test statistic* to discriminate *signal plus background* and *background* hypotheses.

$$Q_i = \frac{e^{-(s_i+b_i)}(s_i + b_i)^{d_i}}{d_i!} \bigg/ \frac{e^{-b_i}b_i^{d_i}}{d_i!}. \quad (5.1)$$

In Eq. 5.1, s_i is the estimated signal, b_i is the background, and d_i is the number of candidates in each bin in the calculation of confidence levels. This test statistic allows for an easy combination of different experiments (treated as different channels), thus making it appropriate for our case with two separate analyses over different datasets. The joint statistic for the outcome of two channels is just the product of the test statistic of the two channels separately,

$$Q = \prod_{i=1}^n Q_i, \quad (5.2)$$

It is convenient to express the test statistic in a logarithmic form, known as the log-likelihood ratio (LLR),

$$-2 \ln Q = 2 \sum_{i=1}^n s_i - 2 \sum_{i=1}^n \ln(1 + s_i/b_i) \quad (5.3)$$

The confidence level for the possibility that the simultaneous presence of signal and background ($s + b$ hypothesis) is consistent with data is defined as

$$CL_{s+b} = P_{s+b}(Q \leq Q_{obs}), \quad (5.4)$$

i.e, the fraction of a large pool of pseudo-experiments that have test statistic less than or equal to the observed one.

Similarly, the confidence level for the background-only scenario (b hypothesis) is given by

$$CL_b = P_b(Q \leq Q_{obs}). \quad (5.5)$$

The modified frequentist confidence level CL_s is calculated as,

$$CL_s = CL_{s+b}/CL_b. \quad (5.6)$$

The main motivation for this non-standard frequentist approach is that it reduces the ambiguity that arises when fluctuations in the background produce deficits of observed events, which lead to an exclusion of the $s+b$ hypothesis even when there is little experimental sensitivity to it. A signal hypothesis is excluded at the 95% confidence level (C.L.) if $CL_s < 0.05$.

Each individual source of systematic uncertainty is approximated by a Gaussian distribution and incorporated in the calculation via the Cousins and Highland [87] method. When correlations between systematic uncertainties are present, they are properly taken into account, as described in Ref. [88]. The method is implemented in the program *Collie* [89], which is employed to set the limits in this analysis.

5.3 Limits on LED

We factorize the acceptance (photon with $p_T > 90$ GeV and in CC) and estimate the total efficiency for the MC signal sample to be 0.38 ± 0.04 for all n in Run IIb; we calculate this efficiency by applying the same requirements as for our photon sample, and by using the data/MC scale factors in the same way as for the SM backgrounds from MC. There is a drop in efficiency of about 10% compared to Run IIa where the total efficiency was 0.48 ± 0.04 . This is mainly due to the drop in efficiency of the anti-track match because of the higher occupancy of the tracker at higher luminosities. The higher luminosities also affect the efficiency of the CPS match and high- p_T jet rejection requirements, but in a lesser degree.

Systematic uncertainties between the two epochs (Run IIa and Run IIb) are very close, but the largest of the two are used in the limit setting procedure. In order to combine the total efficiencies, we perform a luminosity-weighted average of the two values and add an extra systematic uncertainty of 5%. The combined efficiency is then 0.43 ± 0.05 . We employ the modified frequentist approach described in Section 5.2 to set limits on the production cross section for the signal, using the binned photon p_T distribution as the input variable. We assume the leading-order theoretical cross section for the signal. Table 5.1 and Figure 5.1 summarize the limit setting results.

Table 5.1: Summary of limit calculations.

n	Run IIa 1 fb ⁻¹ [64] observed (expected) cross section limit (fb)	Run IIa 1 fb ⁻¹ [64] observed (expected) M_D lower limit (GeV)	Combination 2.7 fb ⁻¹ observed (expected) cross section limit (fb)	Combination 2.7 fb ⁻¹ observed (expected) M_D lower limit (GeV)	CDF 2 fb ⁻¹ [10] observed M_D lower limit (GeV)
2	27.6 (23.4)	884 (921)	19.0 (14.6)	970 (1037)	1080
3	24.5 (22.7)	864 (877)	20.1 (14.7)	899 (957)	1000
4	25.0 (22.8)	836 (848)	20.1 (14.9)	867 (916)	970
5	25.0 (24.8)	820 (821)	19.9 (15.0)	848 (883)	930
6	25.4 (22.3)	797 (810)	18.2 (15.2)	831 (850)	900
7	24.0 (23.1)	797 (801)	15.9 (14.9)	834 (841)	--
8	24.2 (21.9)	778 (786)	17.3 (15.0)	804 (816)	--

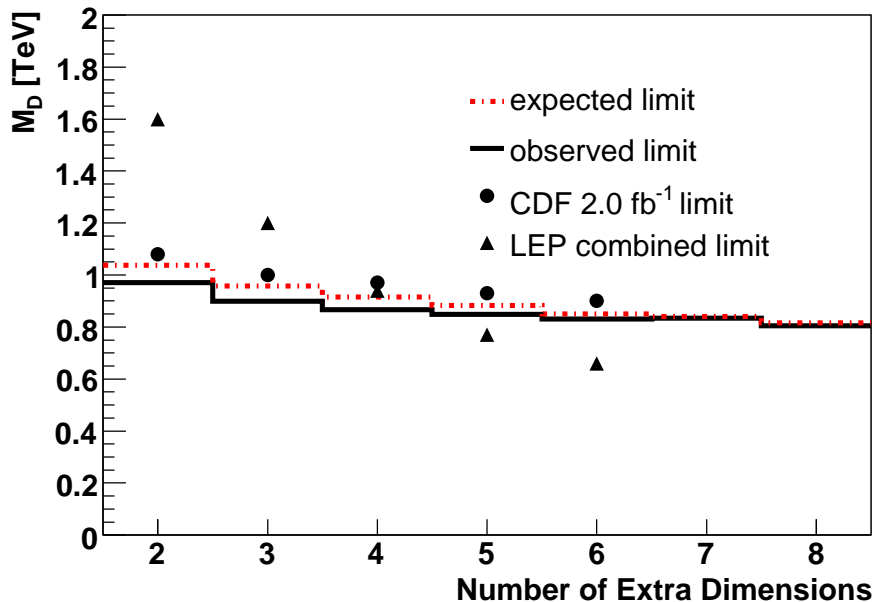


Figure 5.1: Expected and observed lower limits on M_D for LED in the $\gamma + \cancel{E}_T$ final state. CDF limits with 2 fb^{-1} of data (single photon channel) [10], and the LEP combined limits [11] are also shown.

5.4 Summary and Final Remarks

We have conducted a search for large extra dimensions in the $\gamma + \cancel{E}_T$ final states finding no evidence for their presence. We derive the following lower limits on M_D at the 95% C.L.: $M_D > 970, 899, 867, 848, 831, 834$ and 804 GeV for $n = 2, 3, 4, 5, 6, 7$ and 8 extra dimensions, respectively. These limits constitute a significant improvement to the limits set by LEP experiment [11] for $n > 4$, and are in good agreement with the most recent results from CDF [10] experiment.

It is relevant to mention that a search for discrepancies between the SM expectation and data in the $\gamma + \cancel{E}_T$ channel could also serve as a test for the presence of anomalous couplings among neutral gauge bosons, namely, $ZZ\gamma$ and $Z\gamma\gamma$ couplings. A study of this type would alert us about the possibility for physics beyond the SM.

At the time of this writing, we are on the verge of the LHC start-up. The higher energies and luminosities expected in this experiment, together with the ideas and results presented

in this dissertation, will broaden the avenues towards a possible future discovery of LED, or, in their absence, a better understanding of the physical laws of our universe.

REFERENCES

- [1] C. Amsler et al. Review of particle physics. *Phys. Lett.*, B667:1, 2008. ([document](#)), 1.1, 1.2, 2.2
- [2] G. Hesketh. Content of the p17 Muon Thumbnail. DØ Note 4735, 2005. ([document](#)), 3.1, 4.18
- [3] B. W. Worthel B. M. Evanger. Concepts rookie book. Training Documentation Beams-doc-1023-v1, Fermi National Accelerator Laboratory, 2004. ([document](#)), 2.1, 2.1
- [4] Thomas Gadfort. Evidence for electroweak top quark production in proton- antiproton collisions at $s^{1/2} = 1.96$ TeV. FERMILAB-THESIS-2007-55. ([document](#)), 2.2
- [5] G. Borissov. Ordering a Chaos or ... Technical Detail of AA Tracking. Available online at: http://www-d0.fnal.gov/global_tracking/talks/20030228/talk-adm-030228.ps. ([document](#)), 3.1, 3.1
- [6] A. Khanov. HTF: histogramming method for finding tracks. The algorithm description. DØ Note 3778, 2000. ([document](#)), 3.1, 3.2
- [7] Andrew Warren Askew. Measurement of the W gamma to mu nu gamma cross section, limits on anomalous trilinear vector boson couplings, and the radiation amplitude zero in p anti-p collisions at $s^{1/2} = 1.96$ -TeV. FERMILAB-THESIS-2004-31. ([document](#)), 3.3, 3.4
- [8] O. Peters. Muon Segment Reconstruction - Linked List Algorithm. Available online at: http://www-d0.fnal.gov/nikhef/muon_reco/segmentreco/MuonSegmentReconstruction.pdf. ([document](#)), 3.4, 3.5
- [9] U. Baur, Tao Han, and J. Ohnemus. QCD corrections and anomalous couplings in Z gamma production at hadron colliders. *Phys. Rev.*, D57:2823–2836, 1998. ([document](#)), 4.1.2, 4.7
- [10] T. Aaltonen et al. Search for large extra dimensions in final states containing one photon or jet and large missing transverse energy produced in p-pbar collisions at $\sqrt{s} = 1.96$ TeV. 2008. ([document](#)), 4, 5.1, 5.1, 5.4
- [11] LEP Exotica Working Group. Combination of LEP Results on Direct Searches for Large Extra Dimensions. Available online at: http://lepexotica.web.cern.ch/LEPEXOTICA/notes/2004-03/ed_note_final.ps.gz. ([document](#)), 4, 5.1, 5.4

- [12] David J. Griffiths. INTRODUCTION TO ELEMENTARY PARTICLES. NEW YORK, USA: WILEY (1987) 392p. [1](#)
- [13] D. h. Perkins. INTRODUCTION TO HIGH-ENERGY PHYSICS. Reading, Usa: Addison-wesley (1982) 437p. [1](#)
- [14] Michael Edward Peskin and Daniel V. Schroeder. An Introduction to quantum field theory. Reading, USA: Addison-Wesley (1995) 842 p. [4](#)
- [15] L. H. Ryder. QUANTUM FIELD THEORY. Cambridge, Uk: Univ. Pr. (1985) 443p. [4](#)
- [16] Peter W. Higgs. BROKEN SYMMETRIES AND THE MASSES OF GAUGE BOSONS. *Phys. Rev. Lett.*, 13:508–509, 1964. [1.1.3](#)
- [17] M. Veltman. Problems and difficulties in standard model and gravitation. *Int. J. Mod. Phys.*, A20:1163–1167, 2005. [1.2](#)
- [18] Friedemann Brandt. Lectures on supergravity. *Fortsch. Phys.*, 50:1126–1172, 2002. [1.2](#)
- [19] A. A. Tseytlin. Introductory Lectures on String Theory. 2008. [1.2](#)
- [20] Gian Francesco Giudice. Naturally Speaking: The Naturalness Criterion and Physics at the LHC. 2008. [1.2](#)
- [21] Jose Miguel Figueroa-O’Farrill. BUSSTEPP lectures on supersymmetry. 2001. [1.2](#)
- [22] Kenneth Lane. Two lectures on technicolor. 2002. [1.2](#)
- [23] Nima Arkani-Hamed, Savas Dimopoulos, and G. R. Dvali. The hierarchy problem and new dimensions at a millimeter. *Phys. Lett.*, B429:263–272, 1998. [1.3](#), [1.3](#)
- [24] Nima Arkani-Hamed, Savas Dimopoulos, and G. R. Dvali. Phenomenology, astrophysics and cosmology of theories with sub-millimeter dimensions and TeV scale quantum gravity. *Phys. Rev.*, D59:086004, 1999. [1.3](#)
- [25] D. J. Kapner et al. Tests of the gravitational inverse-square law below the dark-energy length scale. *Phys. Rev. Lett.*, 98:021101, 2007. [1.3](#)
- [26] Schuyler Cullen and Maxim Perelstein. SN1987A constraints on large compact dimensions. *Phys. Rev. Lett.*, 83:268–271, 1999. [1.3](#)
- [27] Gian F. Giudice, Riccardo Rattazzi, and James D. Wells. Quantum gravity and extra dimensions at high-energy colliders. *Nucl. Phys.*, B544:3–38, 1999. [1.3](#), [1.4](#), [1.4](#), [4.1.2](#)
- [28] (Ed.) Cole, Frank T., (Ed.) Goldwasser, Edwin L., and (Ed.) Wilson, Robert Rathbun. National Accelerator Laboratory design report January 1968. FERMILAB-DESIGN-1968-01. [2](#)
- [29] TeVI Group. Design Report Tevatron 1 project. FERMILAB-DESIGN-1984-01. [2](#)

- [30] Pushpalatha C. Bhat and William J. Spalding. Fermilab collider Run II: Accelerator status and upgrades. *AIP Conf. Proc.*, 753:30–41, 2005. 2
- [31] M. Begel, D. Edmunds, P. Laurens, and R. Partridge. DØ Luminosity in Run 2: Delivered. DØ Note 3970, 2003. 2
- [32] B. W. Worthel J. P. Morgan. Pbar rookie book. Training Documentation Beams-doc-1021-v1, Fermi National Accelerator Laboratory, 2004. 2.1
- [33] V. M. Abazov et al. The upgraded D0 detector. *Nucl. Instrum. Meth.*, A565:463–537, 2006. 2.3, 2.3.1, 7
- [34] DØ Upgrade Collaboration. DØ Silicon Tracker Technical Design Report. Available online at: http://d0server1.fnal.gov/projects/silicon/www/silicon_old.html. 2.3.1.1
- [35] Michael S. Weber. The D0 silicon micro-strip tracker. *Nucl. Instrum. Meth.*, A560:14–17, 2006. 2.3.1.1
- [36] K. Hanagaki. D0 layer 0 innermost layer of silicon microstrip tracker. *Nucl. Instrum. Meth.*, A569:8–11, 2006. 2.3.1.1
- [37] DØ Upgrade Collaboration. The DØ Upgradet Central Fiber Tracker Technical Design Report. Available online at: http://d0server1.fnal.gov/projects/scifi/cft_home.html. 2.3.1.2
- [38] M. Adams et al. Design Report of the Central Preshower Detector for the D0 Upgrade. DØ Note 3014, 1996. 2.3.2
- [39] M. Bhattacharjee et al. Technical Design Report of the Forward Preshower Detector for the D0 Upgrade. DØ Note 3445, 1998. 2.3.2
- [40] S. Abachi et al. The D0 Detector. *Nucl. Instrum. Meth.*, A338:185–253, 1994. 2.3.3
- [41] V. M. Abazov et al. Run IIB upgrade technical design report. FERMILAB-PUB-02-327-E. 2.3.6.1
- [42] M. Abolins et al. Design and Implementation of the New D0 Level-1 Calorimeter Trigger. *Nucl. Instrum. Meth.*, A584:75–97, 2008. 2.3.6.1
- [43] DØ Algorithms Group. How to Run RECO. Available online at: <http://www-d0.fnal.gov/computing/algorithms/howto/howtoreco.html>. 3
- [44] DØ Algorithms Group. DØRun II Event Data Model. Available online at: http://www-d0.fnal.gov/software/data_model/data_model.html. 3
- [45] R. Fruhwirth. Application of Kalman filtering to track and vertex fitting. *Nucl. Instrum. Meth.*, A262:444–450, 1987. 3.1.2

- [46] A. Schwartzman and C. Tully. Primary Vertex Reconstruction by Means of Adaptive Vertex Fitting. DØ Note 4918, 2005. [3.2](#)
- [47] M. Narain and A. Schwartzman. Probabilistic Primary Vertex Selection. DØ Note 4042, 2002. [3.2](#)
- [48] F. Fleuret. The DØ Electron/Photon Analysis Package EMAnalyze. DØ Note 3888, 2001. [3.3](#)
- [49] F. Fleuret, F. Beaudette, and S. Protopopescu. The DØ Soft Electron Reconstruction Package SEMReco. DØ Note 3872, 2001. [3.3](#)
- [50] F. Beaudette and Grivaz J.-F. The Road Method. DØ Note 3976, 2002. [3.3](#)
- [51] Georg Steinbrueck. Measurement of the angular distribution of electrons from W boson decays at D0. FERMILAB-THESIS-1999-24. [3.3](#), [4.1.4.7](#)
- [52] A. Atramentov and Y. Maravin. Utilizing CFT and SMT hits count for photon and electron reconstruction. DØ Note 4444, 2004. [3.3](#), [4.1.4.2](#)
- [53] L. Wang, J. Hays, J. Mitrevski, and C. Schwanenberger. Electron Likelihood Efficiency in p17. DØ Note 5114, 2006. [3.3](#)
- [54] F. Déliot. The Fit Algorithm in muo_trackreco. Available online at: <http://www-d0.fnal.gov/~deliot/fitalg.ps>. [3.4](#)
- [55] L. Chevalier, F. Déliot, C. Guyot, Ch. Royon, and B. Tuchming. Track Parameter Error Matrix Propagation in Matter and Magnetic Field, Error Matrices Combination. Available online at: <http://www-d0.fnal.gov/~tuchming/myprop.ps>. [3.4](#)
- [56] P. Calfayan, T. Gadfort, G. Hesketh, V. Lesne, M. Owen, R. Strohmmer, V. Sharyy, and B. Tuchming. Muon Identification Certification for p17 data. DØ Note 5157, 2007. [3.4](#), [4.2.0.9](#)
- [57] Gerald C. Blazey et al. Run II jet physics. 2000. [3.5](#), [3.5](#)
- [58] E. Busato and A. Bernard. Jet Algorithms in the DØ Run II Software: Description and User's Guide. DØ Note 4457, 2004. [3.5](#)
- [59] B. Oliver, U. Bassler, and G. Bernardi. NADA, A new Event by Event Hot Cell Killer. DØ Note 3687, 2000. [3.5](#)
- [60] U. Bassler and G. Bernardi. Towards a Coherent Treatment of Calorimetric Energies: Missing Transverse Energy, Jets, E.M. Objects and the T42 Algorithm. DØ Note 4124, 2002. [3.5](#)
- [61] L. Swayer and A. Stone. Missing ET Reconstruction: Variables and Methods. DØ Note 3957, 2003. [3.6](#)

- [62] S. Trincaz-Duvoid and P. Verdier. Missing ET Reconstruction in p17. DØ Note 4474, 2004. [3.6](#)
- [63] J. Steele and B. Hirosky. mETR_x: A MissingET Revertexing Tool. DØ Note 3895, 2001. [3.6](#)
- [64] V. M. Abazov et al. Search for Large Extra Dimensions via Single Photon plus Missing Energy Final States at $\sqrt{s} = 1.96$ TeV. *Phys. Rev. Lett.*, 101:011601, 2008. [4](#), [5.1](#)
- [65] V. M. Abazov et al. Search for Large extra spatial dimensions in the dielectron and diphoton channels in $p\bar{p}$ collisions at $\sqrt{s} = 1.96$ TeV. 2008. [4](#)
- [66] A. Abulencia et al. Search for large extra dimensions in the production of jets and missing transverse energy in p anti-p collisions at $\sqrt{s} = 1.96$ -TeV. *Phys. Rev. Lett.*, 97:171802, 2006. [4](#)
- [67] V. M. Abazov et al. Search for large extra spatial dimensions in dimuon production at D0. *Phys. Rev. Lett.*, 95:161602, 2005. [4](#)
- [68] V. M. Abazov et al. Search for large extra dimensions in the monojet + missing E_T channel at DØ. *Phys. Rev. Lett.*, 90:251802, 2003. [4](#)
- [69] M. Owen and M. Hohlfeld. Trigger Efficiencies for the OR of Single Electron Triggers in p17 Data. DØ Note 5409, 2007. [4.1.1](#)
- [70] TriggerMeisters. Available online at: http://www-d0online.fnal.gov/www/groups/tm/tm_main.html, 2008. [1](#)
- [71] Torbjorn Sjostrand, Leif Lonnblad, Stephen Mrenna, and Peter Skands. PYTHIA 6.3: Physics and manual. 2003. [4.1.2](#)
- [72] Stephen Mrenna. private communication, 2007. [4.1.2](#)
- [73] U. Baur and Edmond L. Berger. Probing the W W gamma Vertex at the Tevatron Collider. *Phys. Rev.*, D41:1476, 1990. [4.1.2](#)
- [74] Andrew Askew. private communication, 2007. [4.1.2](#)
- [75] R. Brun and F. Carminati. GEANT. CERN Program Library Long Writeup Report No. W5013, 1994. [4.1.2](#)
- [76] Stilianos Isaak Kesisoglou. Search for gauge mediated supersymmetry in the gamma gamma missing-E(T) channel. FERMILAB-THESIS-2004-44. [4.1.3](#), [4.1.3](#), [4.1.3](#)
- [77] A. Atramentov et al. Photon Identification in p17 Data. DØ Note 4976, 2005. [4.1.4](#), [4.2.0.9](#)
- [78] A. Atramentov et al. Electron and Photon Identification with p20 Data. DØ Note 5761, 2008. [4.1.4](#), [4.2.0.9](#)

- [79] V. M. Abazov et al. Search for Supersymmetry in Di-Photon Final States at $\sqrt{s} = 1.96$ TeV. *Phys. Lett. B*, 659:856, 2008. [4.1.4.2](#)
- [80] E. Carrera, A. Ferapontov, Y. Maravin, and Y. Gershtein. Study of $Z\gamma \rightarrow \nu\nu\gamma$ events in DØ Run IIa and Run IIb Data. DØ Note in preparation, 2008. [4.1.4.2](#)
- [81] Atramentov A., X. Bu, and J. Zhu. p20 Hits on the Road Study. Available online at: <http://www-d0.hef.kun.nl//askArchive.php?base=agenda&categ=a08888&id=a08888s1t65/transparencies>. [4.1.4.2](#)
- [82] Y. Maravin and Y. Gershtein. Search for GMSB SUSY in Diphoton Events with Large Missing E_T . DØ Note 5425, 2007. [4.1.4.3](#), [4.1.4.3](#)
- [83] J. Lazoflores. Tagging of Bremsstrahlung Muons that Deposit Energy in the Electromagnetic Calorimeter Faking a Photon Signal. DØ Note 5112, 2006. [4.1.4.5](#)
- [84] B. Calpas, S. Kermiche, and E. Nagy. Search for Heavy Resonances Decaying into gamma+jet Final States. DØ Note 5510, 2007. [4.1.4.7](#)
- [85] V. Buescher et al. Recommendation of the Ad-Hoc Committee on Limit-Setting Procedures to be Used by DØ in Run II. DØ Note 4629, 2004. [5.2](#)
- [86] Thomas Junk. Confidence level computation for combining searches with small statistics. *Nucl. Instrum. Meth.*, A434:435–443, 1999. [5.2](#)
- [87] Robert D. Cousins and Virgil L. Highland. Incorporating systematic uncertainties into an upper limit. *Nucl. Instrum. Meth.*, A320:331–335, 1992. [5.2](#)
- [88] Wade Fisher. Calculating Limits for Combined Analyses. DØ Note 4975, 2006. [5.2](#)
- [89] Wade Fisher. Collie: COncidence Level LLimit Evaluator. Available online at: <http://www-d0.hef.kun.nl//askArchive.php?base=agenda&categ=a081312&id=a081312s10t1/transparencies>. [5.2](#)

BIOGRAPHICAL SKETCH

Edgar F. Carrera

The author of this dissertation was born in the volcanic highlands (2850 m) of Quito, Ecuador. After graduating from his High School, Colegio Marista, in the year of 1997, he spent almost a year in Modesto, CA as an exchange student at Davis High School, where he made very good friends and also learned some English.

Back in Ecuador, in the Fall of 1998, he was admitted in the National Polytechnic School in Quito, the most prestigious university in Ecuador. There, he majored in Physics and graduated with honors, receiving a Bachelor of Science in the Spring of 2004. His thesis was under the supervision of his undergrad adviser Dr. Luis Lascano, with whom he worked on studying "The Electric Conductivity in AC current of Ferroelectric Ceramics of Composition $Pb_xBi_4Ti_{3+x}O_{(1,2,3)+x}$ ".

Even though this was an interesting topic, it was not related to what he really wanted to do: particle physics. Unfortunately, there was no such field of research in Ecuador, so he decided to pursue his higher-level education abroad. In July of 2003 he was awarded full scholarship to go to Trieste, Italy, for the Summer School in Particle Physics at the International Center for Theoretical Physics (ICTP). The enriching experience confirmed and enhanced his interest in the field.

He moved to Tallahassee, FL in the fall of 2004 to study at Florida State University and to join, later on (Summer of 2005), the High Energy Physics group. He spent the first years of his doctoral training working for the Compact Muon Solenoid experiment at the Large Hadron Collider accelerator at CERN in Geneva, Switzerland. He contributed primarily to the intercalibration of the electromagnetic calorimeter (ECAL) system, and the development and implementation of a technique for the calibration of its response. Early

in 2007 he joined the DØ Collaboration at the Tevatron at Fermilab. There, he served as calorimeter subsystem expert, contributed with the electromagnetic identification group, and published an article on the search for large extra dimensions (Phys. Rev. Lett. 101, 011601 (2008)).

Edgar successfully defended his dissertation in December 2008 and, at the time of this writing, he continues working at DØ as a calorimeter expert and preparing a publication on $ZZ\gamma/Z\gamma\gamma$ anomalous coupling.